Scalable Generation of Cluster State with Superconducting Circuit

(超伝導回路を用いたスケーラブルなクラスタ状態生成手法)

by

Takahiko Satoh

佐藤　貴彦

A Doctor Thesis

博士論文

Submitted to

the Graduate School of the University of Tokyo

on Dec 12, 2014

in Partial Fulfillment of the Requirements

for the Degree of Doctor of Information Science and Technology

in Computer Science

Thesis Supervisor: Hiroshi Imai　今井　浩

Professor of Computer Science

ABSTRACT

Recently, fault tolerant quantum computation such as surface coding and topological quantum computation has been paid attention to due to high threshold against computational errors compared with that of conventional gate-model quantum computation. These schemes use a two or three-dimensional cluster state as universal resources for quantum computation. We can generate a cluster state by performing controlled-phase gates on an initial state prepared in $|+\rangle$ state, where the control-phase gates are realized by nearest neighbor Ising type interactions. There are many proposal to realize Ising type interaction such as ultracold atoms in an optical lattice, superconducting charge qubits, superconducting spin qubits, resonator wave guides, nitrogen-vacancy centers, and quantum dots. Among many candidates, we especially discuss superconducting flux qubits. Superconducting flux qubits have a strong anharmonicity, so that we can perform high-speed single-qubit rotation with excellent fidelity.

Usually, implementation of high-fidelity two-qubit gates is the hardest part for the realization of quantum computation. Two qubit gates require in-situ turn on/off the interaction between qubits by the external control apparatus. Since imperfection of the interaction control tends to induce spatially correlated errors between qubits, sophisticated technology is required to suppress such error rate below the threshold of fault tolerant quantum computation. Up to now, the generation of a large cluster state using solid-state qubit has not been demonstrated in a scalable manner yet. One of the main obstacles is the requirement for independent control of two-qubit gates that are necessary for the scalable quantum information processing. For a superconducting flux qubit, existing method uses applied magnetic field to control the interaction. It is known that the application of magnetic field to local area is difficult. Thus, it is hard to implement local control of the interaction without cross-talk problem where unwanted errors occurs between qubits.

Firstly, we propose a novel way to control a number of two-qubit gates independently without using the on/off switching of locally applied magnetic field. Specifically, we assume the superconducting flux qubits that are inductively coupled with each other via always-on Ising interaction. Unlike the previous method to change the interaction strength with unitary operations, we fully make use of non-unitary properties of projective measurements so that we can effectively turn on/off the interaction via quantum feedforward. Also, we show how to generate a two or three-dimensional cluster state that are universal resource for fault tolerant quantum computation with constant step-size operations. The on/off switching of locally applied magnetic field is not necessary to

perform projective measurements and quantum feedforward. Thus, it is expected that our scheme may contribute to achieve a scalability of flux qubits system.

Secondly, we propose the interaction generating method using capacitively-coupled flux qubits to overcome the cross-talk problem. In this scheme, we generate Ising type interaction by applying bias voltage to qubits which are connected via capacitor. Our scheme has a property that we can control the interaction strength by applying bias voltage, which does not require on/off switching of applied magnetic field. Furthermore, for an arbitrary size of the system, we propose the constant step-size procedure for generating a scalable two-dimensional cluster state. In this scheme, we can sufficiently suppress non-nearest neighbor interactions. Also, we estimate the parameter range to implement fault torelant quantum computation in this architecture.

Our proposals pave the way for scalable quantum information processing with superconducting flux qubits.

論文要旨

近年，従来の誤り訂正符号を用いたゲートモデルや MBQC モデルの量子計算よりも高いエラー耐性を持つ Surface coding やトポロジカル量子計算と呼ばれるフォールトトレラント量子計算が注目を集めている．同量子計算では，２次元や３次元のクラスタ状態を万能量子資源として用いる．クラスタ状態を生成する手法の一つとして，$|+\rangle$ 状態の量子ビットを複数個用意し，量子ビット間にイジング型相互作用を働かせた系の時間発展によって構成した制御位相ゲートを用いる方法が知られている．イジング型相互作用の生成は，冷却原子や NV 中心，量子ドット，超伝導系などさまざまな系で実現している．本研究ではこれらの系の中で，特に超伝導磁束量子ビットに関する議論を行う．超伝導磁束量子ビットはエネルギー準位に強い非調和性を示すため，高速かつ高精度な１量子ビット操作が可能な特性を持つ系である．

一般的に，高フィデリティな２量子ビットゲートの実装は量子計算の実現に向けた最も困難な技術であると考えられている．２量子ビットゲートは，適切なタイミングで on/off 制御される量子ビット間の相互作用により構成される．不完全な相互作用制御は量子ビット間に相関したエラーを引き起こすため，フォールトトレラント量子計算の持つエラー閾値を下回る高度な制御技術が必要となる．現在までのところ，固体素子量子ビットによる実用的な大規模クラスタ状態の生成には至っていない．その要因の一つとして，スケーラブルな量子情報処理に必須となる，複数の２量子ビットゲートの独立制御の難しさが挙げられる．超伝導磁束量子ビットの場合，従来手法では外部磁場を用いた相互作用の生成・制御が行われてきたが，外部磁場の局所印加は難しいことが知られている．そのため，印加外部磁場が引き起こすクロストークを抑制し，他の量子ビットの状態へ影響を与えないような相互作用の局所的な on/off 制御は困難という問題がある．

そこで本研究では，局所的な印加磁場の on/off 制御を必要とせず，複数の２量子ビットゲート独立制御が可能になる新たな手法を提案する．　具体的には，隣接超伝導磁束量子ビット間に常時磁気結合によるイジング型相互作用が存在する系を想定する．ユニタリ操作による相互作用強度の変更を行う従来手法とは異なり，本手法では非ユニタリ操作である射影測定と量子フィードバックを用いることで，１量子ビット操作の高いタイミング精度に基づく実効的な相互作用の on/off 制御を行う．さらに，同手法を用いた２次元および３次元のクラスタ状態を系のサイズに依らず，定数ステップで生成する手順を提案する．射影測定と量子フィードバックは局所的な印加磁場の on/off を必ずしも必要としないため，これらの手法はスケーラビリティ獲得に貢献すると考えられる．

また，外部磁場制御の問題を根本的に解決するため，電荷結合を用いた新たな超伝導磁束量子ビット間相互作用の生成手法を提案する．本手法では，キャパシタを介して結合された複数の超伝導磁束量子ビットに対して，電圧を印加することでイジング型相互作用を生成する．同手法の特徴として，印加電圧の変更によって相互作用の強度調整・局所生成が可能であることや，クロストークの要因である相互作用生成のための外部磁場の印加の on/off 制御を必要としないこと，さらに，多数の超伝導磁束量子ビットから構成される系を想定し，非隣接間相互作用を十分に抑制した上で，２次元クラスタ状態を定数ステップで生成する手順の整備と必要となる各種パラメータの推計を行なった．

これらの手法は超伝導磁束量子ビットの持つ外部磁場制御の困難さに起因する複数の２量子ビットゲートの独立操作に対する問題を解決し，より大規模な量子情報処理の実現に向けたアプローチとなる．

Acknowledgements

First of all, I would like to thank my adviser Professor Hiroshi Imai for his valuable comments and continuous support during the last five years.

Special thanks also go to Yuichiro Matsuzaki, Hiraku Toida, Kosuke Kakuyanagi, William J. Munro, Koichi Semba, Hiroshi Yamaguchi, Shiro Saito, and the other members of NTT Basic Research Laboratories. And I would also like to thank François Le Gall, Masato Edahiro, Akitoshi Kawamura, Toshihiro Tanuma, Jeans-François Baffier, Takyuya Akiba, Hidefumi Hiraishi, Yoichi Iwata, Alonso Gragera, Bingkai Lin, Keigo Oka, and the other members of Imai Laboratory for giving a lot of fun and talking about many things.

Finally, I would like to thank my parents for their unconditional support.

Contents

List of Figures

List of Tables

Chapter 1

Introduction

1.1 Backgrounds

Quantum computation is a new paradigm of information processing. Known algorithms give superior performance for tasks such as factoring [93, 88], searching an unsorted database [43, 44], quantum simulation [1, 116], other algorithms [29, 47, 96, 22, 24, 13] and more. All these algorithms require a large-scale quantum computer. A quantum computer is composed of a sequence of single-qubit gates and two-qubit gates [32, 27, 65, 16]. The single-qubit gate denotes a rotation of the qubit around an arbitrary axis and degree. A control-phase gate is one of the typical examples of two-qubit gates. This gate flips the phase of the target qubit if and only if the state of the control qubit is $|1\rangle$. The role of control and target qubits are reversible for a control-phase gate. This gate can be realized by Ising type interaction between control and target qubit. Individual qubits should be efficiently addressed, and the interaction between two qubits should be controlled by some external apparatus.

The challenge is how to design and build a quantum computer with realistic technology. This requires quantum architecture. There have been a number of quantum architectures for relevant physical systems, such as the nitrogen-vacancy centre [113, 73], ion traps [71], superconducting systems [40]. To realize fault-tolerant quantum computation, it is crucial to investigate a scheme to generate a cluster state in a scalable way. The cluster state is a universal resource for quantum computation, and this state can be used for a fault-tolerant scheme such

as surface code [87, 84] and topological code [83]. The cluster state is generated by performing controlled-phase gates on nearest-neighbor qubits which are prepared in $|+\rangle$ state and set on a square lattice. One can generate a cluster state if we can turn on/off an Ising type interaction between qubits with high accuracy. Moreover, controlled-phase gate should be performed within a time scale much shorter than the decoherence time for fault-tolerant quantum computation.

Superconducting circuit is one of the promising systems to realize such a cluster-state quantum computation using solid-state system. Josephson junctions in the superconducting circuit can induce a non-linearity, and so one can construct a two-level system. There are several types of Josephson junction qubit: charge qubit [19], superconducting spin qubit [79], superconducting flux qubit [15, 25, 77, 17], superconducting phase qubit [4, 51, 99], superconducting transmon qubit [31, 60, 6, 8], fluxonium qubit [69, 120], and several hybrid systems [115, 100].

The transmon qubit [31, 60, 6], which is a cooper-pair box and relatively insensitive to low-frequency charge noise, is considered one of the powerful method of the qubit implementation by using superconducting circuit. Scheme of the tunable qubit-qubit capacitive coupling is proposed and demonstrated [40, 21, 39]. The high fidelity qubit readout using a microwave amplifier is demonstrated [92, 52, 55]. Furthermore, high fidelity (99.4%) two-qubit gate using five qubits system is achieved. This result is the first step toward surface code scheme [8]. These results show a good scalability towards the realization of generating a large scale cluster state.

The flux qubit consist of a superconducting loop containing several Josephson junctions. This system has a large anharmonicity and can be well approximated to a two-level system. Single qubit gate operations can be realized with high speed and reasonable fidelity [114]. Meanwhile, the best observed coherence time is an order of 10 μs [18, 101]. Quantum non-demolition measurement of flux qubits during the coherence time is realized by using Josephson bifurcation amplifier [94, 95, 57, 58]. Furthermore, the tunable coupling schemes for two qubit gate operations are proposed and demonstrated [80, 41, 50, 108, 76, 46, 5, 112, 42].

There are two typical tunable qubit-qubit coupling schemes, inductive cou-

pling and capacitive coupling. In flux-qubit systems, existing schemes rely on inductive coupling with the external magnetic field. Several schemes of the tunable qubit-qubit inductive coupling are proposed and demonstrated [80, 41, 50, 108, 76, 46, 5, 112, 42]. However, it is hard to apply magnetic field to a localized region. Due to this property, the control of individual qubits with magnetic field tends to produce decoherence and cross talk. Therefore, suppressing the cross talk for qubit-qubit coupling is important to achieve further scalability for flux qubit system.

1.2 Contributions

As mentioned above, a flux qubit has a large anharmonicity which makes it possible to construct a two-level system, and therefore flux qubits provide us with almost ideal two-level systems unlike transmon qubit. This property might be important for large scale quantum computation. If the system is not a two-level system, there might exist an error that induce a transition from the target two-level system to another unknown state, so that quantum state cannot be confined in the target two-level system. The standard quantum error correction (QEC) schemes [87, 84, 83] assume ideal two-level systems. The QEC scheme for non ideal two-level system is still developing. Even if a new QEC for such imperfect two-level systems was invented, the threshold for the gate operations might be worse than those for the standard QEC. Therefore, flux qubits could be suitable for large-scale quantum computation.

In this dissertation, we show improving methods for cross talk problem that focus on enhancing the scalablity of controlled-phase gate on superconducting flux qubits.

Our first contribution is to suggest a new way to control the Ising type interaction between flux qubits where each qubit is inductively coupled with another qubit. As mentioned above, many schemes of inductively coupling for flux qubits are suggested and demonstrated. Meanwhile, these methods require high-speed and high-accuracy on/off switching of applied local magnetic field. For this reason, it is hard to control the interaction with suppressed cross talk in these

schemes. We propose the way to control the interaction between inductively coupled flux qubits based on a novel technique using always-on Ising interaction, quantum measurement, and feedforward [110, 89, 70, 58]. It is worth mentioning that we do not need to change the amount of magnetic fields at all during computation. Once we calibrate the proper value of the magnetic fields on each flux qubit before starting computation, we can control the interaction just using quantum measurement and feedforward. In quantum mechanics, there are two type of operations, unitary operations such as applying microwave pulses and non-unitary operations such as readout of the qubit. While most of the authors in previous papers use unitary operation to control the interaction [12, 11, 118], we exploit the non-unitary properties that the projective measurement have. We will assume an always-on Ising interaction between nearest neighbor qubits, and will insert an ancillary qubit between the qubits that process quantum information. We show that it is possible to effectively turn on/off the interaction via quantum measurement and feedforward on the ancillary qubits. Furthermore, we explain how scalability is achieved in this scheme, and suggest a way to construct a large two or three-dimensional cluster state which enables us to perform fault tolerant quantum computation with high error threshold [83]. Since quantum feedforward is matured technology in superconducting circuit, our proposal provides a feasible and reliable way to control the interaction between the flux qubits. Moreover, it is possible to implement quantum measurements and feedforward without switching on/off applied magnetic fields on the flux qubits, which may make it easy to achieve individual addressability. Therefore, our scheme would be a crucial step for the realization of flux-qubit based quantum computation.

Our second contribution is the generating and controlling method of Ising type interaction between four-junction flux qubits using capacitive coupling. By using an applied voltage, we control the interaction between flux qubits that are connected by capacitance. Unlike the standard schemes, our scheme does not require to change the applied magnetic field on the flux qubit for the control of the interaction. This may have advantage to suppress a cross talk between the flux qubits because applying local voltages is typically much easier than applying local

magnetic flux. We take into account of realistic noise, the fluctuation width of the applied voltage and the timing jitter, on this type of flux qubits, and estimate a qubit-parameter range where one can perform fault-tolerant quantum computation [87, 84]. Furthermore, we show constant step-size methods for generating a one or two dimensional cluster states in a scalable way. In these methods, we show the optimum parameter set, coupling capacitance, applied voltage, and step-size, with fixed noise parameters. Furthermore, we show echo pulses are effective to reduce the number of operation steps.

1.3 Organization of this Dissertation

In Chapter 2, we present the fundamentals of quantum computation and a review of existing research. In Chapter 3, we explain about our scalable architecture for generating a two or three dimensional cluster state using superconducting circuit with always-on Ising interaction. In Chapter 4, we show our result of generation Ising type interaction between flux qubits using capacitive coupling. Chapter 5 is the concluding remarks of this Dissertation.

Chapter 2

Preliminaries

2.1 Quantum computation

In this section, we first review key ingredients of quantum computation, and some definitions and theorems that are used in this thesis.

2.1.1 Qubit

The fundamental unit of classical information is described as a binary digit (bit), which has a state either "0" or "1". In the case of quantum information, the fundamental unit is a quantum bit (qubit) which has two possible orthonormal quantum states $|0\rangle$ and $|1\rangle$. A qubit is expressed as a superposition of two states $|0\rangle$ and $|1\rangle$ with amplitudes α and β as follows:

$$|\psi\rangle = \alpha|0\rangle + \beta|1\rangle,$$

where α and β denotes complex number satisfying $|\alpha|^2 + |\beta|^2 = 1$.

More formally, the state of a qubit is also described by a unit vector in a two-dimensional complex vector space $\mathbb{C}^2$. Furthermore, the state $|0\rangle$ and $|1\rangle$ are known as computational basis states as the following column vectors:

$$|0\rangle = \begin{pmatrix} 1 \\ 0 \end{pmatrix}, |1\rangle = \begin{pmatrix} 0 \\ 1 \end{pmatrix}.$$

Definition 1. A qubit is described by a unit vector in a two-dimensional Hilbert

space $\mathbb{C}^2$ and can be represented as linear combination of two orthonormal quantum states $|0\rangle$ and $|1\rangle$ with amplitudes α and β as follows:

$$|\psi\rangle = \alpha|0\rangle + \beta|1\rangle = \begin{pmatrix} \alpha \\ \beta \end{pmatrix},$$

where α and $\beta \in \mathbb{C}^2$ and $|\alpha|^2 + |\beta|^2 = 1$.

A general quantum state of n qubits can be written as: $|\psi\rangle = \sum_{x\in\{0,1\}^n} \alpha_x|x\rangle$, where α_x are complex numbers such that $\sum_{x\in\{0,1\}^n} |\alpha_x|^2 = 1$.

2.1.2 Transform operation

The transformation of quantum systems are given by unitary quantum operators. Then, single qubit gate operations can be described by 2×2 matrices. We show several substantial gates for single qubit transformations, and Pauli, phase shift and Hadamard operators are described as

$$\sigma_X : = \hat{X} = |1\rangle\langle 0| + |0\rangle\langle 1| = \begin{pmatrix} 0 & 1 \\ 1 & 0 \end{pmatrix}, \tag{2.1}$$

$$\sigma_Y : = \hat{Y} = -i|1\rangle\langle 0| + i|0\rangle\langle 1| = \begin{pmatrix} 0 & -i \\ i & 0 \end{pmatrix}, \tag{2.2}$$

$$\sigma_Z : = \hat{Z} = |0\rangle\langle 0| - |1\rangle\langle 1| = \begin{pmatrix} 1 & 0 \\ 0 & -1 \end{pmatrix}, \tag{2.3}$$

$$S : = |0\rangle\langle 0| + i|1\rangle\langle 1| = \begin{pmatrix} 1 & 0 \\ 0 & i \end{pmatrix}, \tag{2.4}$$

$$H : = \frac{1}{\sqrt{2}}(|0\rangle\langle 0| + |1\rangle\langle 0| + |0\rangle\langle 1| - |1\rangle\langle 1|) = \frac{1}{\sqrt{2}} \begin{pmatrix} 1 & 1 \\ 1 & -1 \end{pmatrix}. \tag{2.5}$$

We denote the Hadamard basis by$\{|+\rangle, |-\rangle\}$ as follows:

$$|+\rangle = H|0\rangle = \frac{1}{\sqrt{2}}(|0\rangle + |1\rangle) = \frac{1}{\sqrt{2}}\begin{pmatrix}1\\1\end{pmatrix},$$
$$|-\rangle = H|1\rangle = \frac{1}{\sqrt{2}}(|0\rangle - |1\rangle) = \frac{1}{\sqrt{2}}\begin{pmatrix}1\\-1\end{pmatrix}.$$

For arbitrary multi-qubit quantum operations, it is necessary to implement at least one two-qubit gate operation. We use the Controlled-phase (Controlled-Z) gate, which is described by the following two qubits transformation:

$$\begin{aligned}\hat{U}_{CZ}^{(a,b)} &= |0\rangle_a|0\rangle_b\langle 0|_a\langle 0|_b + |0\rangle_a|1\rangle_b\langle 0|_a\langle 1|_b \\ &\quad +|1\rangle_a|0\rangle_b\langle 1|_a\langle 0|_b - |1\rangle_a|1\rangle_b\langle 1|_a\langle 1|_b \\ &= \begin{pmatrix}1&0&0&0\\0&1&0&0\\0&0&1&0\\0&0&0&-1\end{pmatrix}. \end{aligned} \tag{2.6}$$

where a and b denote the name of qubits.

2.1.3 Measurement

If we measure a qubit in $|0\rangle, |1\rangle$ basis, then we obtain only one bit information either $|0\rangle$ (with probability $|\alpha|^2$) or $|1\rangle$ (with probability $|\beta|^2$). After measurement, that qubit is not entangled with other quantum system.

2.2 Graph states as a resource for quantum computation

Let us review the concept of a graph state introduced in [107, 49, 48, 35]. A graph $G(V, E)$ is composed of vertices V and edges E where an edge connects two vertices. By regarding the vertex as a qubit and edge as an entanglement between the qubits, we can associate the graph with a graph state $|\Phi\rangle_{G(V,E)}$

defined as the following equation

$$|\Phi\rangle_{G(V,E)} = \prod_{(a,b)\in E} \hat{U}_{CZ}^{(a,b)} |+\rangle^{\otimes N}$$

where $(a,b) \in E$ denotes an edge between the vertices a and b. Also, $\hat{U}_{CZ}^{(a,b)}$ denotes a controlled-phase (π) operation between them.

The controlled-phase gate can be realized by Ising type interaction [86, 85]. When a graph $G(V,E)$ is given, the necessary Hamiltonian to create a cluster state corresponding G is as follows

$$\hat{H}_{G(V,E)} = \sum_{(l,l')\in E} g_{(l,l')} \frac{1+\hat{Z}_l}{2} \frac{1+\hat{Z}_{l'}}{2}$$

where $g_{(l,l')}$ denotes the interaction strength between qubit l and l'. By letting a separable state $\otimes_{l\in V}|+\rangle_l$ evolve for $g_{(l,l')}t = \pi$ according to this Hamiltonian, the following unitary operator will be applied to the initial state

$$\begin{aligned} S_{G(V,E)} &= \exp\left(-i\pi \sum_{(l,l')\in E} \frac{1+\hat{Z}_l}{2} \frac{1+\hat{Z}_{l'}}{2}\right) \\ &= \prod_{(l,l')\in E} \hat{U}_{CZ}^{(l,l')}. \end{aligned}$$

and hence we can create the target graph state.

Although there are many proposal to realize Ising type interaction such as ultracold atoms in an optical lattice [68, 67, 34, 104, 56, 97, 20, 54], ion traps [81, 28, 38, 117, 36, 23], superconducting charge qubit [19], superconducting spin qubit [79], superconducting flux qubit [15], resonator waveguide [63], nitrogen-vacancy center [102, 74, 14, 113, 91, 33, 3], quantum dot [103, 111, 45, 64] and electronic spins coupled to the motion of magnetized mechanical resonators [82], the major challenge for experimental realization is to switch on/ off the interaction with a high fidelity. Only a few experiments have demonstrated a high fidelity controllable two-qubit gate with a fidelity above the threshold of fault tolerant quantum computation [90, 10, 7]. One of the possible ways to overcome the

experimental difficulties for demonstrating the high-fidelity two-qubit gates is to use an always-on interaction scheme [119, 53, 61, 12, 11, 118]. Since there are no need for the additional controlling operations to switch the interaction, these scheme may scale well for a large number of qubits. Here, we propose a new approach to implement fault tolerant quantum computation with always-on interaction by using the non-unitary properties of projective operations and quantum feedforward.

2.2.1 Fault tolerant quantum computation using cluster states

A specific type of a graph state such as a two or three-dimensional cluster state, which are generated in d-dimensional lattices, can be a universal resource for measurement-based quantum computation (MBQC) [86, 85, 75, 106] and topological quantum computation [87, 84, 83]. Topological quantum computation, which is based on Kitaev's surface codes for quantum error correction using qubits which are attached to each edge of the square lattice on the torus or other surface [59], is known for the high error tolerance.

When we use a two-dimensional cluster state for surface codes, there are three types of main qubits. One of them is called a logical qubit that contains quantum information. The other qubits are called syndrome qubits. Half of syndrome qubits are to detect the dephasing errors on the logical qubits while the other ancillary qubits are to detect bit-flip noises. Main qubits are set on a grid point of square lattice as shown in Fig. 2.1.

Topological quantum computation using a three-dimensional cluster state is known to have a high threshold for quantum error correction especially when there is a finite probability to lose a qubit [9, 98]. The overview of this scheme is shown in Fig. 2.2 where three-dimensional cluster state is used as a resource for the computation. In the 3D cluster state, qubits connected in a z-axis direction are used for the logical qubit that contains the information for the computation (Fig.2). The other qubits located between the logical qubits are used for detecting error syndrome. In order to process the computation with error corrections, we measure qubits by layer. Syndrome qubits are measured in $\hat{X}$-basis, and the

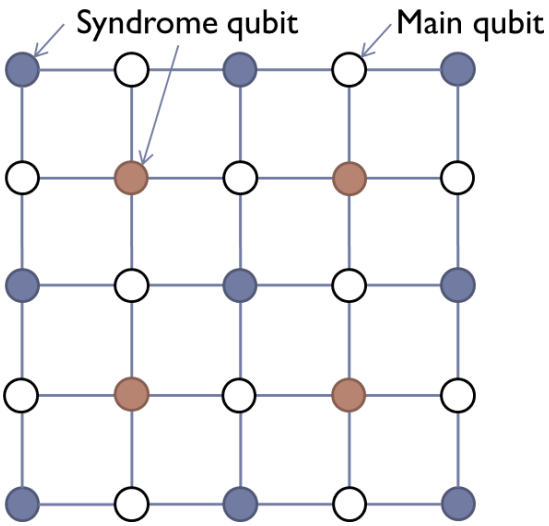

Figure 2.1: Schematic of a two-dimensional cluster state. Hollow circles denote logical qubits and colored circles denote two types of syndrome qubits for surface coding scheme. Logical qubits hold arithmetical quantum information. Blue qubits deny $\hat{X}$ errors, and red qubits deny $\hat{Z}$ errors. We refer to these qubits as main qubits.

outcomes are used for detecting the location and type of the error, so that we can correct the error after analyzing the syndromes by classical computation.

2.3 Superconducting flux qubit

The superconducting flux qubit consist of a superconducting loop containing several Josephson junctions. The two quantum states correspond to persistent current flowing in clockwise and anti-clockwise directions, as first proposed by Mooij *et al.* [72, 78] in 1999. In 2000, Van der Wal *et al.* [109] and Jonathan *et al.* [37] demonstrated the superposition of persistent currents using flux qubit. For example, we show the circuit of three-Josephson junctions flux qubit proposed by Mooij *et al.* [72] in Fig. 2.3. In particular, the superconducting loop include three or four Josephson junctions to suppress effectively the height of energy barrier between double well. We explain the detail of components of flux qubits as follows.

Even if the superconducting loop does not include Josephson junctions, the

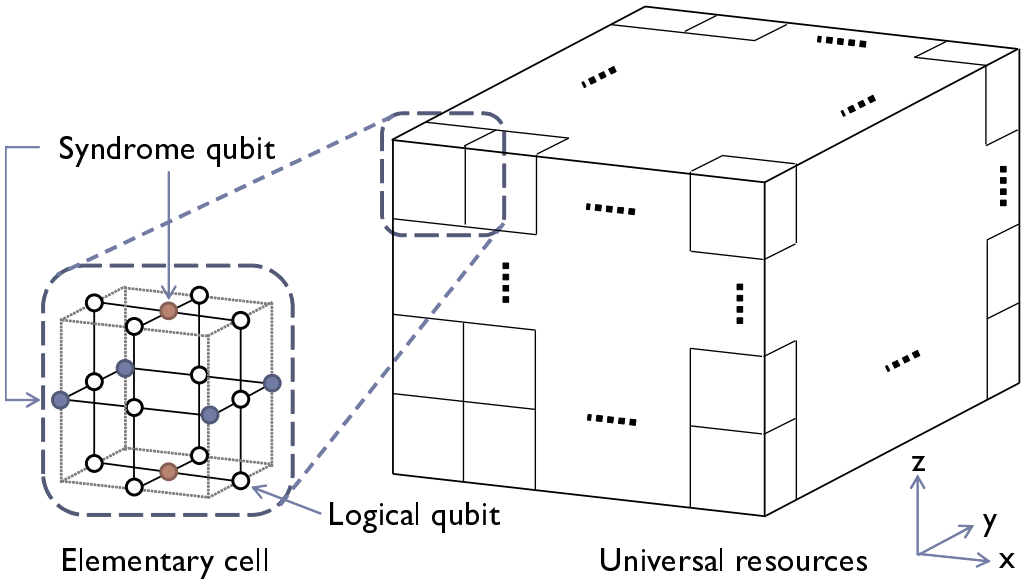

Figure 2.2: Elementary cell of a 3D cluster state consist of 18 qubits. Universal resources for 3D MBQC is recursively-generated by many elementary cells. The circles having an edge along the z-axis direction correspond to main qubits. The other circles correspond to syndrome qubits to detect errors. The size of each layer on xy-plane is determined by the number of logical qubits and the depth of the error correction codes. The height along the z-axis is determined by the number of quantum gates to be implemented.

phase change in the one cycle along the direction of the loop is $2\pi f$ when the external magnetic flux $f = \frac{\Phi}{\Phi_0}$ imposed through the loop. Here, $\Phi_0 = \frac{h}{2e}$ denotes the flux quantum, and h denotes Planck's constant. When the wave function make a round of the loop, the phase return to the initial values. Due to this fact, the amount of magnetic flux through the loop is quantized to integer multiples of the flux quantum. This phenomenon is called "flux quantization".

A (SIS type) Josephson junction consists of two superconductors which are coupled via a insulator. The persistent current I_S in the Josephson junction is described as follows:

$$I_S = I_C \sin(\phi) \tag{2.7}$$

where I_C denotes the critical current of the Josephson junction, and the phase of the Josephson junction ϕ corresponds to the phase difference between the two superconductors. We point out two important parameters defining the properties

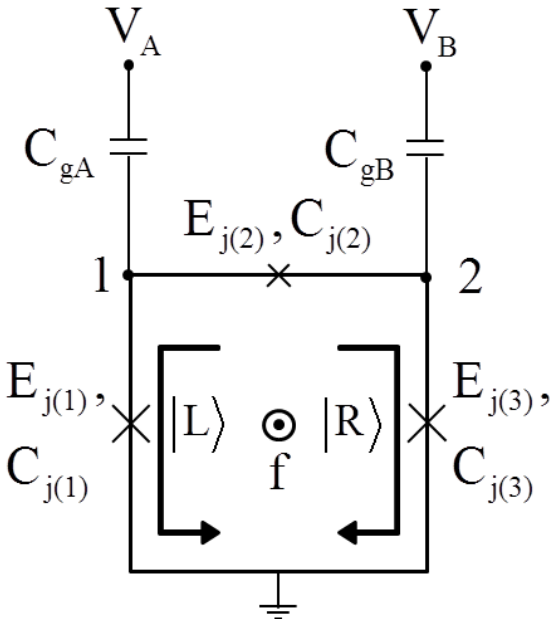

Figure 2.3: The circuit of a three-Josephson junction (JJ) flux qubit. $E_{j(n)}$ and $C_{j(n)}$ denote the Josephson energy and capacitance of n-th Josephson junction JJn. The loop is threaded by an external magnetic flux f, and we can control the energy bias of the qubit via the magnetic flux. Node 1 and 2 represents the superconducting island. The voltage bias $V_A(V_B)$ is applied to the flux qubit via gate capacitance $C_{gA}(C_{gB})$.

of Josephson junction as follows:

- The Josephson coupling energy: $E_j = \hbar\frac{I_C}{2e}$
- The Coulomb energy (for single charge): $E_c = \frac{e^2}{2C_j}$

where C_j denotes the capacitance of Josephson junction. The Josephson coupling energy is the coupling strength between two cooper-pairs in the two superconductors via barrier, and decides I_C. The relation between these energies will determine the nature of Josephson junction and thus, the properties of superconducting qubit. In case of flux qubits (persistent-current qubits), the relation is $E_j >> E_c$.

2.3.1 Qubit-qubit coupling scheme

Practical scheme to perform the two-qubit operation, such as controlled-phase gate, needs coupling between a pair of physical qubit. Traditionally, interaction between the flux qubits is realized by inductive coupling. We introduce such examples as follows.

Plourde *et al.* proposed a scheme for tunable coupling using a superconducting quantum interference device (SQUID), which is composed of a superconducting loop interrupted by two Josephson junctions, in 2004 [80]. In this scheme, a SQUID is coupled to both of two flux qubits through an identical mutual inductance. The coupling strength is determined by the mutual inductance and the current bias applied to the SQUID. We show the circuit model for this scheme in Fig. 2.4. The same SQUID can be used to measure the qubit state. The above

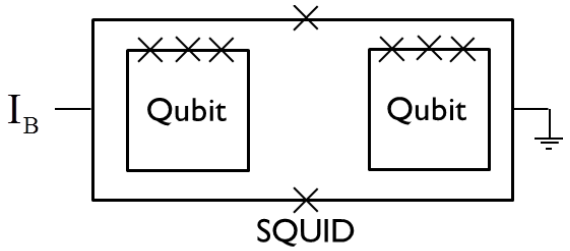

Figure 2.4: Schematic of the coupler circuit proposed by Plourde *et al.* [80]. The interaction strength between two flux qubits depends strongly on the bias current I_B.

proposal is expanded to three-qubit, two-coupler system by Groszkowski *et al.* in 2011 [42]. They showed the optimal parameter sets to suppress the unwanted interactions such as the cross talk. Hime *et al.* demonstrated the system for Plourde's scheme in 2006 [50]. They use two independent bias fluxes to determine the applied SQUID flux Φ_S. The dynamic inductance of SQUID and coupling strength depend on Φ_S. They showed that after the applied fluxes are adjusted, they can turn the coupling on and off by simply switching the bias current through the SQUID. using only the switching of the bias current through the SQUID.

Grajcar *et al.* proposed a tunable coupling scheme with a coupler loop con-

taining three Josephson junctions in 2006 [41]. The coupler loop assembled between two flux qubits on the same circuit. In this scheme, the coupling strength between flux qubits is controlled by the transition frequency of the flux through the coupler loop and a combination frequency of two flux qubits. We show the circuit model for this scheme in Fig. 2.5. Van der Ploeg *et al.* demonstrated a

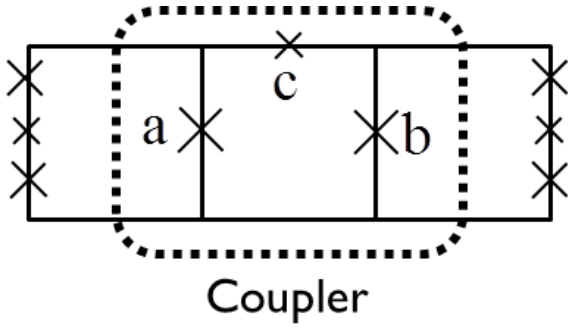

Figure 2.5: Schematic of the three junction coupler and two flux qubits circuit. Josephson junction a, b, and c compose a tunable coupler. Each flux qubit share a Josephson junction with coupler.

controllable coupling scheme between two flux qubits using inserting the additional coupler loop containing three Josephson junctions in 2007 [108]. Same as the Grajcar's scheme, the interaction strength between two qubits a and b can be tuned by changing the coupler's flux bias f_c. They controlled the fluxes through the qubits and the coupler by bias currents I_{b1}, I_{b2}, and I_{b3} and dc-current I_{bT} in the coil around the qubits circuit. This scheme is the first demonstration of the sign-tunable coupling using Josephson coupler between two three-junctions flux qubits.

Niskanen *et al.* demonstrated a controllable coupling scheme using three four-junctions flux qubit. We show the circuit model for this scheme in Fig. 2.6. The middle qubit (qubit 3) has larger qubit energy than other qubits 1 and 2 at the coherence optimal bias point. They showed that when qubit 3 is prepared in its ground state, one can perform single qubit operations on the qubit 1 and 2, because the coupling between qubits 1 and 2 is weak. Furthermore, they coupled qubits 1 and 2 via excited qubit 3 which is biased far from optimal point whereas

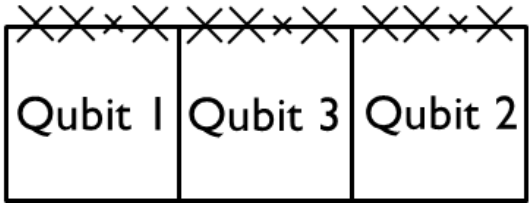

Figure 2.6: Schematic diagram of three four-junctions flux qubits coupler circuit. In each qubit, one of the Josephson junction has Josephson energy and capacitance that are 0.5 times smaller than those of other junctions.

qubits 1 and 2 are at the optimal point. This feature is expected to provide the long coherence time of tunable coupled qubits, and it is important to achieve scalability.

2.3.2 Measurement

The SQUID is a device to measure the state of the superconducting flux qubits. The SQUID is used for magnetic field detection with high sensitivity. A particular state of the qubit makes the SQUID to switch from zero-voltage to finite-voltage. However, the readout of a flux qubit using a SQUID destroys the system to support a two-level system, so that we cannot perform the measurement sequentially.

The measurement by Josephson bifurcation amplifier (JBA) overcome this problem. The JBA use the non-linearity of a resonant circuit which is connected to a capacitor across the Josephson junction. This resonant circuit has a bistability, a high- and a low-amplitude state, caused by a driving field with the suitable frequency. The ability of the JBA to detect the magnetic field is sensitive enough to measure the flux qubit state. Furthermore, the connected Josephson junction is maintained at zero-voltage in this measurement process, so that the system to support qubit is not destroyed by JBA measurement.

Chapter 3

Scalable architecture of quantum computation with always-on Ising interaction using superconducting circuit

3.1 Introduction

In this chapter, we propose a way to control the interaction between qubits with always-on Ising interaction. Unlike the standard method to change the interaction strength with unitary operations, we fully make use of non-unitary properties of projective measurements, so that we can effectively turn the interaction on or off via feedforward. We then show how to generate a two- or three-dimensional cluster state that are universal resource for fault-tolerant quantum computation with this scheme. Our scheme provides an alternative way to realize a scalable quantum processor.

The remainder of this chapter is organized as follows. Section 3.3 presents the detail of our scheme to show how always-on interaction is effectively turned on/off via projective measurement to ancillary qubits and quantum feedforward. In Sec. 3.4 and Sec. 3.5, we propose the way to generate two and three-dimensional cluster states using qubits arranged on a plane. In Section 3.7, we discuss about experimental parameters for our scheme. Section 3.8 concludes our discussion.

3.2 Experimental setup

All experiments are carried out in Mathematica 8 on a Linux server with Intel Core i7-4770K at 3.50 GHz (4 physical cores) and 32GB of main memory.

3.3 Effective interaction control via projective measurements and quantum feedforward

3.3.1 Physical setup

Now, we consider the physical setup of the qubit in this chapter. We use the cross-shape type superconducting flux qubit as shown in Fig. 3.1. When we apply the

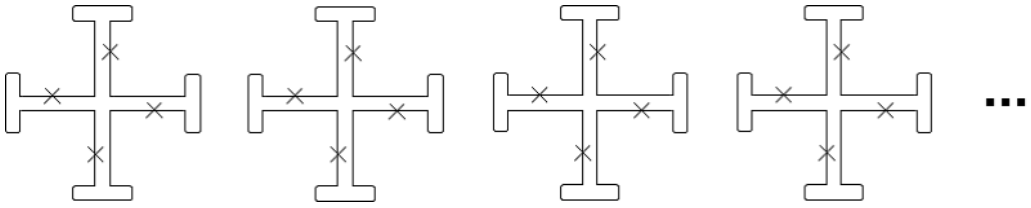

Figure 3.1: A setup of physical qubits on one-dimensional array. The flux qubit consists of superconducting loop and four-Josephson junctions. We increase the area of the loop around the edge of the cross-shape, so that we can increase the coupling strength between nearest neighbor qubits. Each pair of nearest neighbor qubits can be coupled via magnetic field generated by their persistent current. Due to the cross-shape structure, the distance between non-nearest neighbor qubits becomes large, so that the non-nearest neighbor coupling should be negligible in our setup.

suitable magnetic field to the n qubits on one-dimensional array for coupling the nearest neighbor qubits, the system Hamiltonian become as follows:

$$\hat{H} \;=\; \sum_{l=1}^{n} \varepsilon \hat{Z} + \sum_{l,l'|(|l-l'|=1)}^{n} \frac{g_{(l,l')}}{4} \hat{Z}_l \hat{Z}_{l'} \tag{3.1}$$

3.3.2 Hamiltonian

We introduce a Hamiltonian to realize our scheme to turn the interaction on or off effectively via projective measurements and quantum feedforward. Since we consider superconducting flux qubits that are known to have excellent con-

trollability, we can assume that every qubit can be individually controlled by a microwave pulse and there are always-on interaction between nearest neighbor qubits. Throughout of this chapter, we assume the following Hamiltonian corresponding to $G(V, E)$

$$\begin{aligned}
\hat{H} &= \hat{H}^{system}_{G(V,E)} + \hat{H}^{interaction}_{G(V,E)} && (3.2)\\
\hat{H}^{system}_{G(V,E)} &= \sum_{l\in V}\Big(\frac{\omega_l}{2}\hat{Z}_l + \lambda_l(t)\cos\big(\omega'_l t+\theta\big)\hat{X}_l\Big) && (3.3)\\
\hat{H}^{interaction}_{G(V,E)} &= \sum_{(l,l')\in E}\frac{g_{(l,l')}}{4}\hat{Z}_l\hat{Z}_{l'} && (3.4)
\end{aligned}$$

where ω, $\lambda(t)$, ω', θ, and g denote the qubit energy, Rabi frequency, microwave frequency, a phase of the microwave, and interaction strength, respectively. In the superconducting flux qubit systems, it is possible to control the value of $\lambda(t)$ by changing the power of the microwave with much higher accuracy than in the case of two-qubit gates. We move to a rotating frame defined by

$$\hat{U} = e^{-i\sum_l^N \frac{\omega'_l}{2}\hat{Z}_l t} \tag{3.5}$$

where ω'_l denotes the angular frequency of the rotating frame at site l, and we use a rotating wave approximation as follows. From the Schrödinger equation

$$\hat{H}(t)|\psi(t)\rangle = i\frac{d}{dt}|\psi(t)\rangle \tag{3.6}$$

and

$$|\psi'(t)\rangle = \hat{U}|\psi(t)\rangle \iff |\psi(t)\rangle = \hat{U}^\dagger|\psi'(t)\rangle, \tag{3.7}$$

we could obtain the rotated Hamiltonian

$$\hat{H}'(t) = \hat{U}\hat{H}(t)|\psi(t)\rangle\hat{U}^\dagger - i\hat{U}\frac{d\hat{U}^\dagger}{dt}. \tag{3.8}$$

Therefore, the local Hamiltonian could be approximated to

$$\hat{H}^{system}_{G(V,E)} = \sum_{l\in V}\frac{1}{2}\begin{pmatrix} \omega_l-\omega_l' & \lambda_l(e^{i(\theta+2\omega t)}+e^{-i\theta}) \\ \lambda_l(e^{i\theta}+e^{-i(\theta+2\omega t)}) & -(\omega_l-\omega_l') \end{pmatrix} \tag{3.9}$$

$$\simeq \sum_{l\in V}\left(\frac{\omega_l-\omega_l'}{2}\hat{Z}_l+\frac{\lambda_l}{2}\hat{X}_l\right). \tag{3.10}$$

Here, we used

$$\cos\left(\omega_l' t+\theta\right)=\frac{1}{2}\left(e^{-i(\omega t+\theta)}+e^{i(\omega t+\theta)}\right) \tag{3.11}$$

and ignored high-frequency components $\lambda e^{i2\omega t}$ and $\lambda e^{-i2\omega t}$. Hence, we obtain the following Hamiltonian

$$\hat{H} \simeq \sum_{l\in V}\left(\frac{\omega_l-\omega_l'}{2}\hat{Z}_l+\frac{\lambda_l}{2}\hat{A}_l^{\theta}\right)+\sum_{(l,l')\in E}\frac{g_{(l,l')}}{4}\hat{Z}_l\hat{Z}_{l'} \tag{3.12}$$

where

$$\hat{A}^{\theta}=\begin{pmatrix} 0 & e^{-i\theta} \\ e^{i\theta} & 0 \end{pmatrix}. \tag{3.13}$$

Unless required to perform single qubit gates, we turn off the microwave and set all $\lambda = 0$, and therefore the Hamiltonian introduced here is effectively the same as an Ising model with always-on interaction. On the other hand, for the implementation of accurate single-qubit rotations, we assume a large Rabi frequency, $\lambda \gg g$, so that the coupling strength from the nearest neighbor qubit can be negligible. We will later discuss an error accumulation due to imperfect single qubit rotation in detail.

The Hamiltonian described above has the interesting property that an interaction from other qubits can be turned off by preparing the state of a qubit in a ground state. To explain this, we consider a specific qubit A and other qubits

interacting with the qubit A, and the Hamiltonian of those is described as

$$\hat{H}'_A = \left(\sum_{(A,j)\in E} \frac{\omega_j - \omega'_j}{2} \hat{Z}_j + \frac{g_{(A,j)}}{4} \hat{Z}_A \hat{Z}_j \right) + \frac{\omega_A - \omega'_A}{2} \hat{Z}_A \tag{3.14}$$

$$= \sum_{(A,j)\in E} \left(g_{(A,j)} \frac{\mathbf{1} + \hat{Z}_A}{2} \frac{\mathbf{1} + \hat{Z}_j}{2} + \frac{\omega_j - \omega'_j - \frac{g_{(A,j)}}{2}}{2} \hat{Z}_j \right) \tag{3.15}$$

with

$$\omega_A - \omega'_A = \sum_{(A,j)\in E} \frac{1}{2} g_{(A,j)}, \lambda_A = 0 \tag{3.16}$$

Interestingly, if qubit A is prepared in a ground state, the interaction from qubit A cancels out because of

$$g_{(A,j)} \frac{\mathbf{1} + \hat{Z}_A}{2} \frac{\mathbf{1} + \hat{Z}_j}{2} |\downarrow\rangle_A = 0. \tag{3.17}$$

This means that preparing a specific qubit in a ground state effectively turns off the interaction between this qubit and the nearest-neighbor qubit. Therefore, if all nearest-neighbor qubits are in the ground state, the qubit is not effected by any interactions, which is the striking feature of our scheme. Also, if qubit A is prepared in a excited state, the interaction causes an extra phase shift in qubit B.

It is worth mentioning that we need precise control of the frequency of the microwave in our scheme. We investigate the effect of a small detuning from the target frequency of the microwave. Supposing that there is a detuning of $\delta\omega_j$ from the target frequency, we have

$$\omega'_j = \omega_j - \frac{g_{(A,B)}}{2} + \delta\omega'_j. \tag{3.18}$$

In this case, we can rewrite the Hamiltonian (3.15) as follows.

$$\hat{H}''_{AB} = \sum_{(A,j)\in E} \left(g_{(A,j)} \frac{\mathbf{1} + \hat{Z}_A}{2} \frac{\mathbf{1} + \hat{Z}_j}{2} + \frac{\delta\omega'_j}{2} \hat{Z}_j \right). \tag{3.19}$$

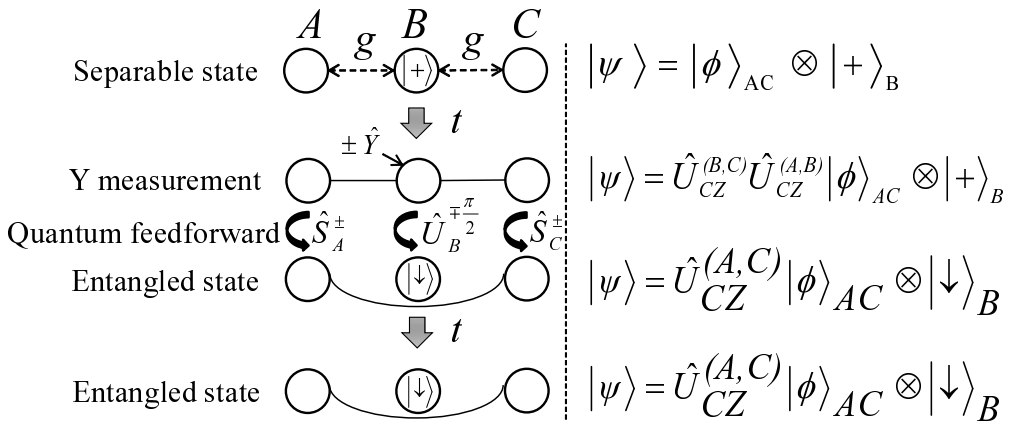

Figure 3.2: Schematic of our scheme to implement two-qubit gates via projective measurements and quantum feedforward udner the effect of always-on Ising interaction. We let evolve the state $|\phi\rangle_{AC} \otimes |+\rangle_B$ according to the Hamiltonian, perform a projective measurement onto the middle qubit, and rotate the middle qubit back into a ground state, so that a C-Phase can be implemented between the qubit A and C. Due to the engineered Hamiltonian form that we make, this guarantees that the qubit A and C does not evolve anymore even under the effect of the always-on Ising type Hamiltonian.

Hence, frequency errors cause a phase shift error on each qubit. Fortunately, due to recent developments in microwave technology, accurate control of the microwave frequency is possible. Therefore, in this paper, we assume that we can choose the exact microwave frequency to avoid this kind of error.

3.3.3 Interaction switching with quantum feedforward

Although we will later discuss the case of two or three-dimensional cluster state that is a universal resource for quantum computation [83] , we start by explaining how to generate a one-dimensional three-qubit cluster state (Fig. 3.2) to illustrate our concept about how to control the effective interaction via projective measurements and quantum feedforward. Suppose that we have three qubits, A, B, and C, in a row and that all coupling strengths between the nearest neighbor qubits

are equally g. Then, the system Hamiltonian becomes as follows.

$$\begin{aligned}\hat{H} &= \sum_{j=A,B,C}\Big(\frac{\omega_j}{2}\hat{Z}_j + \lambda_j(t)\cos\big(\omega_j' t+\theta\big)\hat{X}_j\Big) \\ &\quad + \frac{g_{(A,B)}}{4}\hat{Z}_A\hat{Z}_B + \frac{g_{(B,C)}}{4}\hat{Z}_B\hat{Z}_C \qquad (3.20)\\ &\simeq g_{(A,B)}\frac{\mathbf{1}+\hat{Z}_A}{2}\frac{\mathbf{1}+\hat{Z}_B}{2} + g_{(B,C)}\frac{\mathbf{1}+\hat{Z}_B}{2}\frac{\mathbf{1}+\hat{Z}_C}{2} \qquad (3.21)\end{aligned}$$

with

$$\omega_A' = \omega_A - \frac{1}{2}g, \omega_B' = \omega_B - g, \omega_C' = \omega_C - \frac{1}{2}g, \lambda_A = \lambda_B = \lambda_C = 0. \qquad (3.22)$$

As written in Eq. (3.20), the state of the qubit B changes the energies of qubits A and C. When we set the qubit B to ground state, all eigen states of qubits A and C degenerate therefore $\hat{H}$ does not change the system in time. We show these energy diagrams in Fig. 3.3.

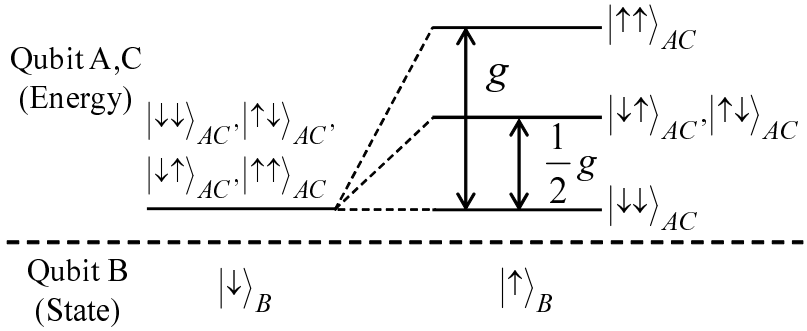

Figure 3.3: The energy diagrams of qubit A and C. The energies depend on the state of the qubit B. The energies of qubit A and C are degenerate when the qubit B is in a ground state. However, once the qubit B is excited, degeneracy is removed so that the energy difference occurs between the states of qubit A and C.

The ancillary qubit induces a conditioned dynamics. The excited state of the ancillary qubit causes the phase rotation on the other qubits, while the ground state of the ancillary qubit does not induce any phase shift on them. Therefore, if we have a superposition of the ancillary qubit, the other two qubits are entangled via such a conditioned dynamics. In order to see this effect more clearly, we

describe how such conditioned dynamics occur in Subsection 3.3.7.

Here, we show the procedure of our scheme for controlled-phase gate. Firstly, we prepare a separable $|+\rangle$ state for the qubit B, and prepare an arbitrary pure state for the qubit A and C. An initial state is described by

$$\rho = |\phi\rangle\langle\phi|_{AC} \otimes |+\rangle\langle+|_B. \tag{3.23}$$

Secondly, we let the system evolves by the Hamiltonian for a time

$$t = \frac{\pi}{g}. \tag{3.24}$$

The total unitary evolution $\hat{U}_{CZ}^{(A,B)}\hat{U}_{CZ}^{(B,C)}$ can be described by

$$\hat{U} = \exp\Big(- ig_{(A,B)}t\frac{\mathbf{1}+\hat{Z}_A}{2}\frac{\mathbf{1}+\hat{Z}_B}{2} - ig_{(B,C)}t\frac{\mathbf{1}+\hat{Z}_B}{2}\frac{\mathbf{1}+\hat{Z}_C}{2}\Big), \tag{3.25}$$

up to local equivalent.

Thirdly, we perform $\hat{Y}$ basis

$$|\pm 1_{\hat{Y}}\rangle = \frac{1}{\sqrt{2}}(|\uparrow\rangle \pm i|\downarrow\rangle) \tag{3.26}$$

measurement on the middle qubit B.

The state after the measurement is written as

$$\rho'_{\pm} = \hat{P}_B^{\pm} e^{-i\hat{H}t}\rho e^{i\hat{H}t}\hat{P}_B^{\pm} \tag{3.27}$$

where $\pm$ denotes the measurement result. Here,

$$\hat{P}^{\pm} = \frac{1}{2}\left(\mathbf{1} \pm \hat{Y}\right) \tag{3.28}$$

denotes a projection operator on the qubit B.

Y measurement

We can perform arbitrary basis measurement using single qubit rotations and a certain basis measurement in combination. For example, we can perform a $\hat{Y}$ basis measurement by a combination of phase shift gates, Hadamard gates, and $\hat{Z}$ basis measurement

$$\hat{P}^{\pm}_{\hat{Z}} = \frac{1}{2}\left(\mathbf{1} \pm \hat{Z}\right). \tag{3.29}$$

This works because the Y basis measurement can be implemented as follows:

$$\hat{P}^{\pm} = S^{-1} H \hat{P}^{\pm}_{\hat{Z}} H S, \tag{3.30}$$

where S^{-1} denotes

$$S^{-1} = |\uparrow\rangle\langle\uparrow| - i|\downarrow\rangle\langle\downarrow| = \begin{pmatrix} 1 & 0 \\ 0 & -i \end{pmatrix}. \tag{3.31}$$

Finally, we perform a quantum feedforward operation, that is an implementation of different local operations depending on the measurement results, onto the qubit B, so that the qubit B can be prepared in a ground state. We define a feedforward operator as

$$\hat{F}^{\pm}_{ABC} = \hat{S}^{\pm}_{A} \hat{U}_{B}^{\frac{\mp\pi}{2},\hat{X}} \hat{S}^{\pm}_{C} \tag{3.32}$$

where $\hat{S}^{\pm}$ denotes a shift gate defined as

$$\begin{pmatrix} 1 & 0 \\ 0 & \pm i \end{pmatrix} \tag{3.33}$$

and $\hat{U}^{\theta,\hat{X}}$ denotes a single-qubit rotating around x-axis rotation with an angle of

θ. The state after the quantum feedforward is described as

$$\rho_{\text{final}} = \hat{F}^{+}_{ABC}\hat{P}^{+}_{B}\rho\hat{P}^{+}_{B}\hat{F}^{+\dagger}_{ABC} + \hat{F}^{-}_{ABC}\hat{P}^{-}_{B}\rho\hat{P}^{-}_{B}\hat{F}^{-\dagger}_{ABC} \tag{3.34}$$

$$= \hat{U}^{(A,C)}_{CZ}|\phi\rangle\langle\phi|_{AC}\hat{U}^{(A,C)}_{CZ} \otimes |\downarrow\rangle\langle\downarrow|_{B}. \tag{3.35}$$

Therefore, after these operations, controlled-phase operations are performed between the qubit A and C, and the state does not evolve anymore because the qubit B is prepared in a ground state. As shown in Fig. 3.3, the states of qubits A and C degenerate and hence interactions are effectively turned off.

Meanwhile, if we set the qubit B in an excited state using a quantum feedforward operation, the final state become as follows.

$$\rho'_{\text{final}} = e^{-i\hat{H}t'}\left(\hat{U}^{(A,C)}_{CZ}\rho_{AC}\hat{U}^{(A,C)}_{CZ} \otimes |\uparrow\rangle\langle\uparrow|_{B}\right)e^{i\hat{H}t'} \tag{3.36}$$

$$= e^{-i\hat{H}'t'}\hat{U}^{(A,C)}_{CZ}\rho_{AC}\hat{U}^{(A,C)}_{CZ}e^{i\hat{H}'t'} \otimes |\uparrow\rangle\langle\uparrow|_{B} \tag{3.37}$$

where $\hat{H}'$ denotes the following Hamiltonian

$$\hat{H}' = g_{(A,B)}\frac{\mathbf{1}+\hat{Z}_A}{2} + g_{(B,C)}\frac{\mathbf{1}+\hat{Z}_C}{2}. \tag{3.38}$$

The energy eigenstates are not degenerate as shown in Fig. 3.3 and hence interactions cause the extra phase shift to qubits A and C. In principle, we can correct these extra phases by performing single qubit rotation. However, unless single qubit rotation can be perfectly performed, such operations induce another error, which makes it difficult to perform fault-tolerant quantum computation. In addition, it is usually difficult to keep the state in an exited state due to the existence of the energy relaxation. For these reasons, we set the qubit B in a ground state after the projective measurement.

Since the interaction is Ising type, the eigenvectors are represented by the computational basis ($|\uparrow\rangle, |\downarrow\rangle$ basis). This means that the ancillary qubit induces a conditional dynamics such that the target qubits evolve differently depending on the state of the ancillary qubit. If we have a superposition of the ground state and excited state of the ancillary qubit, it becomes possible to realize the

superposition of such two dynamics. This is the key to entangle the ancillary qubit with the target qubits.

3.3.4 Unavoidable error of feedforward operation

It is worth mentioning that we could not avoid a detuning error to perform a single qubit rotation in our always-on interaction system. In the superconducting flux qubit system, it is possible to perform a high-fidelity single qubit rotation by applying a on-resonant microwave pulse whose frequency is the same as the qubit energy. However, in our case, the target qubit has an unknown energy shift due to the interaction when a state of nearest neighbor qubits contains a superposition. As an example, we again consider a case of three-qubit one-dimensional chain, and estimate the fidelity to perform a $\frac{\pi}{2}$ pulse on the middle qubit prepared in a ground state, and the Hamiltonian of this system is described as follows.

$$\hat{H}_{ABC} \simeq \sum_{l\in A,B,C} \frac{\omega_l - \omega_l'}{2}\hat{Z}_l + \frac{\lambda_B(t)}{2}\hat{A}_B^{\theta} + \sum_{(l,l')\in(A,B),(B,C)} \frac{g_{(l,l')}}{4}\hat{Z}_l\hat{Z}_{l'}. \quad (3.39)$$

Here, we set mixing angle

$$\theta = \frac{\pi}{2} \quad (3.40)$$

and microwave frequency

$$\omega_B' = \omega_B - g \quad (3.41)$$

to obtain the following Hamiltonian.

$$\hat{H}'_{ABC} = \sum_{l\in A,C} \frac{1}{2}\left(\omega_l - \omega_l' - \frac{g}{2}\right)\hat{Z}_l + \frac{\lambda_B}{2}\hat{Y}_B + \sum_{(l,l')\in(A,B),(B,C)} g\frac{1+\hat{Z}_l}{2}\frac{1+\hat{Z}_{l'}}{2} \quad (3.42)$$

We show the effective Hamiltonian of the qubit B of this case in Table 3.1. Since the resonant frequency of the qubit B depends on the state of the qubit A and C, it becomes impossible to apply on-resonant pulse on the qubit B if one of these states have a superposition. To implement our scheme to control the interaction,

Table 3.1: The effective Hamiltonian of qubit B depends on the states of qubit A and C in Fig. 3.2. When the states of the qubit A and C contains superposition, the resonant frequency of the qubit B is not uniquely determined. Since the microwave frequency is fixed, $\hat{Z}_B$ component induce the detuning error $\epsilon_{\frac{\pi}{2}}$ when we rotate qubit B. As the table shows, the detuning error $\epsilon_{\frac{\pi}{2}}$ becomes maximum for the case of $|\uparrow\uparrow\rangle_{AC}$.

Qubit A and C (state)	Qubit B (effective Hamiltonian)
$\|\uparrow\uparrow\rangle_{AC}$	$H_B = g\hat{Z}_B + \frac{\lambda_B}{2}\hat{Y}_B$
$\|\uparrow\downarrow\rangle_{AC}$, $\|\downarrow\uparrow\rangle_{AC}$	$H_B = \frac{g}{2}\hat{Z}_B + \frac{\lambda_B}{2}\hat{Y}_B$
$\|\downarrow\downarrow\rangle_{AC}$	$H_B = \frac{\lambda_B}{2}\hat{Y}_B$

we have already chosen the frequency of $(\omega_B - g)$ for the microwave $\frac{\pi}{2}$ pulse and the worst fidelity (when the actual effective Hamiltonian of the qubit B is $H_B = g\hat{Z}_B + \frac{\lambda_B}{2}\hat{Y}_B$) can be calculated as follows.

$$\epsilon_{\frac{\pi}{2}} = 1 - \left|\langle\downarrow|e^{-i\hat{H}_B t}|+\rangle\right|^2 \tag{3.43}$$

$$= 1 - \left|\frac{\cos(\frac{1}{2}t\sqrt{4g^2+\lambda_B^2}) + \sin(\frac{1}{2}t\sqrt{4g^2+\lambda_B^2})\frac{2gi+\lambda_B}{\sqrt{4g^2+\lambda_B^2}}}{\sqrt{2}}\right|^2 . \tag{3.44}$$

where $t\left(=\frac{\pi}{2\lambda}\right)$ denotes the duration of the microwave $\frac{\pi}{2}$ pulse. This means that, by increasing the Rabi frequency λ_B, we can suppress this detuning error. We plot this error $\epsilon_{\frac{\pi}{2}}$ against the coupling strength g and the Rabi frequency λ_B in Fig. 3.4.

Throughout of this chapter, when we calculate a fidelity, we always consider the worst case for detuning error as discussed above. The effective Hamiltonian of the target qubit to be rotated by the microwave is described by

$$H_{target} = \frac{\lambda}{2}\hat{X}_{target} \tag{3.45}$$

when all nearest neighbor qubits are in a ground state while the worst case of the Hamiltonian is

$$H_{target} = \frac{g}{2}n\hat{Z}_{target} + \frac{\lambda}{2}\hat{X}_{target} \tag{3.46}$$

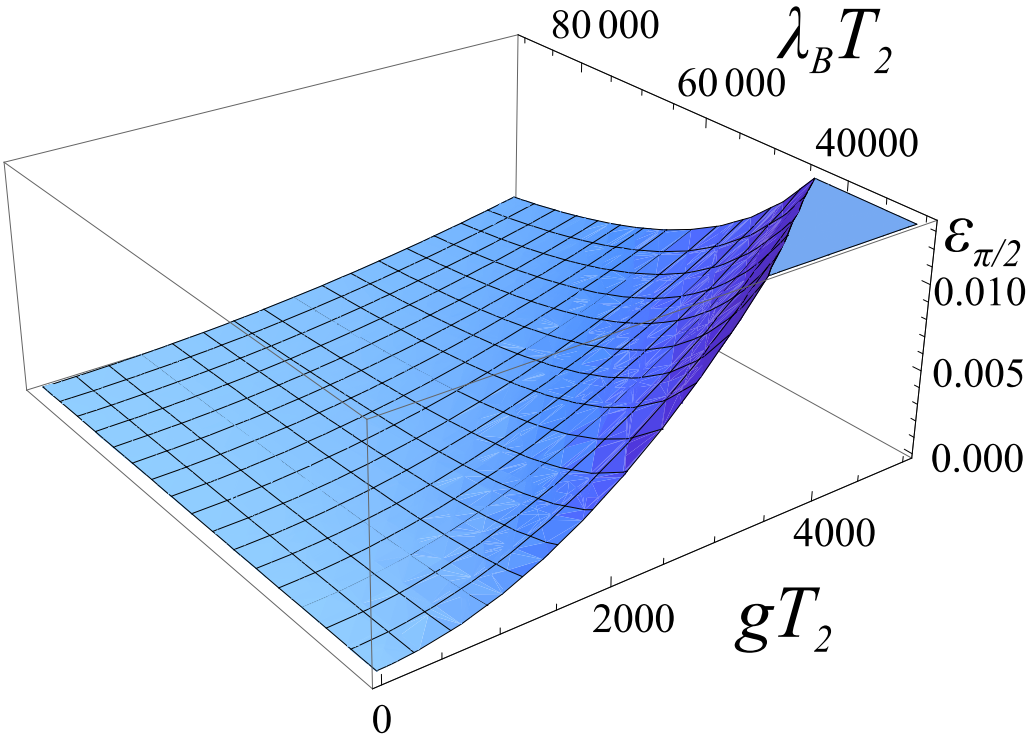

Figure 3.4: The worst rotating error ($\epsilon_{\frac{\pi}{2}}$) and the interaction strength (gT_2) between each pair of nearest neighbor qubits in switching scheme (Fig. 3.2) against various Rabi frequency ($\lambda_B T_2$). Here, T_2 denotes the coherence time of the qubit.

when all nearest neighbor qubit is in an excited state, and we fix the frequency of ($\omega_{target} - \frac{g}{2}n$) for the microwave $\frac{\pi}{2}$ pulse. Here, ω_{target} is the original resonant frequency of the target qubit and n denotes the number of qubits interacting with the target qubit. This will enable us to evaluate the performance of our scheme for the fault tolerant quantum computation.

3.3.5 Optimal interaction strength

Here, we discuss the optimal interaction strength between the qubits to perform a high fidelity controlled-phase gate. Since the coherenece of the quantum states degrades due to decoherence, we need to perform a controlled-phase operation much faster time scale than the coherence time of the qubit. For this purpose, we need to increase the coupling strength to realize a fast controlled-phase gate. However, the strong coupling strength makes it difficult to perform an accu-

rate quantum feedforward operations because the always-on coupling between qubits induces unknown energy detuning of the qubit frequency as described before. Then, there should exist an optimal interaction strength to minimize the controlled-phase gate error that comes from the decoherence of the qubits and imperfect quantum feedforward operations. Decoherence error that we consider is general Markovian noise. We assume that the error rate increases exponentially against time as

$$\epsilon_d = \frac{1}{2}(1 - e^{-\frac{T_{CZ}}{T_2}}). \tag{3.47}$$

Here, T_2 denotes the coherence time of the qubit and $T_{CZ}(= \frac{\pi}{g})$ denotes the gate operation time. Since we consider a parameter regime for $T_{CZ} \ll T_2$, we can simplify the decoherence error as

$$\epsilon_d = \frac{T_{CZ}}{T_2}. \tag{3.48}$$

We assume that the single-qubit operations can be implemented much faster than the coherence time, and hence the decoherence effect during the single qubit operations is negligible compared with other effect such as decoherence during the controlled-phase gate. The setup we consider for the estimation of the optimal coupling strength is as follows. As described in Fig. 3.2, to perform a controlled-phase gate, we use two main qubits A and C and one ancillary qubit B that is inserted between the main qubits. Initially, an ancillary is prepared in a ground state and main qubit are prepared in arbitrary states. Also, for simplicity, we assume that all nearest-neighbor coupling strength between qubits are equal between these three qubits. We evaluate the achievable fidelity during the implementation of a controlled-phase gate in our scheme (Fig. 3.2). Firstly, by performing $\frac{\pi}{2}$ pulse, we rotate the ancillary qubit B from ground state into $|+\rangle$ state. At this time, the qubit B have unknown energy shift due to the coupling from qubit A and C during the rotation, so that a detuning error occurs. Secondly, let evolve the system according to the Hamiltonian. During this time evolution, every qubit is affected by environmental noise, and so decoherence er-

ror accumulates. Finally, we measure $\hat{Y}$ and perform quantum feedforward on the qubit B. Again, due to the coupling from nearest neighbor qubits, qubit A and C suffers the detuning error for the feedforward rotations while the qubit B can be accurately rotated by a resonant microwave pulse. Therefore, the achievable fidelity is calculated as

$$F = 1 - (2\epsilon_{\frac{\pi}{2}} + 3\epsilon_d), \tag{3.49}$$

where we assume that the error makes the state orthogonal to the ideal one to consider the worst case. We plot the achievable fidelity F and interaction strength g corresponding to the range of the Rabi frequency λ in Fig. 3.5(a). Also, we plot the relationship between an achievable fidelity, the optimal interaction strength and Rabi frequency in Fig. 3.5(b). This shows that an achievable fidelity (F) monotonically increase with the increasing Rabi frequency (λ) and interaction strength g has the optimal point against λ.

In this chapter, we do not discuss about the details of the errors in projective measurements and quantum feedforward operations. But we can treat these errors as a type of additional dephasing error. For example, in our switching scheme of 3.3.3, we assume that we fail to perform measurement or feedforward operation with a probability of ϵ_m. The ancillary qubit B become

$$\rho_B = (1-\epsilon_m)|\downarrow\rangle\langle\downarrow|_B + \epsilon_m|\uparrow\rangle\langle\uparrow|_B. \tag{3.50}$$

At this time, the state of the total system is written as

$$\begin{aligned}\rho_{ABC} &= (1-\epsilon_m)\hat{U}_{CZ}^{(A,C)}|\phi\rangle\langle\phi|_{AC}\hat{U}_{CZ}^{(A,C)} \otimes |\downarrow\rangle\langle\downarrow|_B \\ &\quad +\epsilon_m e^{-i\hat{H}t}\hat{U}_{CZ}^{(A,C)}|\phi\rangle\langle\phi|_{AC}\hat{U}_{CZ}^{(A,C)} \otimes |\uparrow\rangle\langle\uparrow|_B e^{i\hat{H}t}.\end{aligned} \tag{3.51}$$

Where

$$\hat{H} = \sum_{(l,l')\in(A,B),(B,C)} g\frac{1+\hat{Z}_l}{2}\frac{1+\hat{Z}_{l'}}{2} \tag{3.52}$$

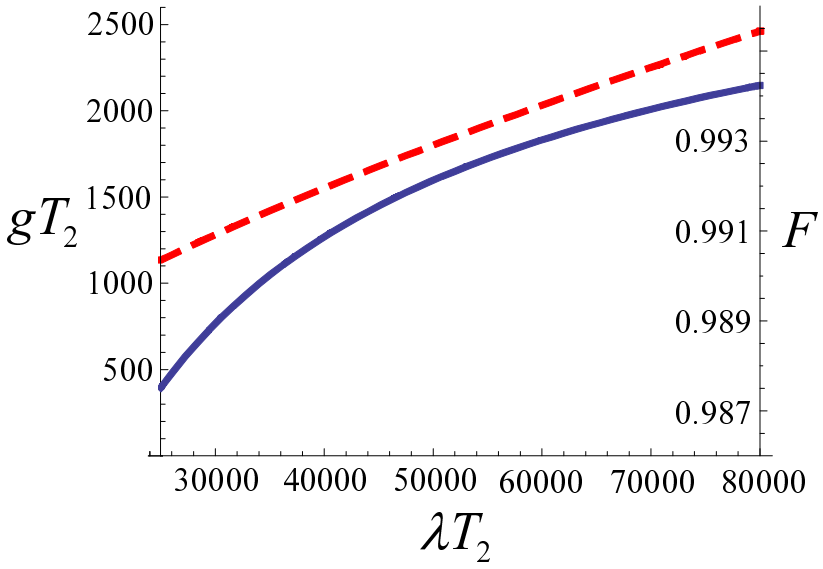

(a)

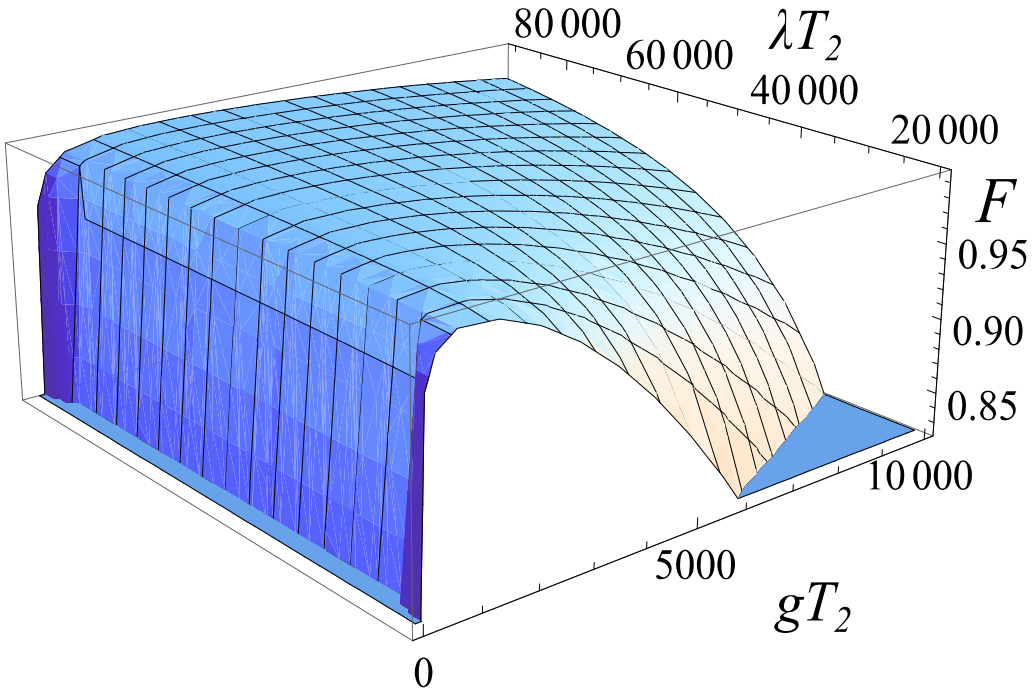

(b)

Figure 3.5: (a) An achievable fidelity (F) and the optimal coupling strength (gT_2) of a controlled-phase gate in our scheme (Fig. 3.2) against various Rabi frequency (λT_2) . The solid line denotes F and the dashed line denotes gT_2. (b) An achievable fidelity (F) against interaction strength (gT_2) and Rabi frequency (λT_2).

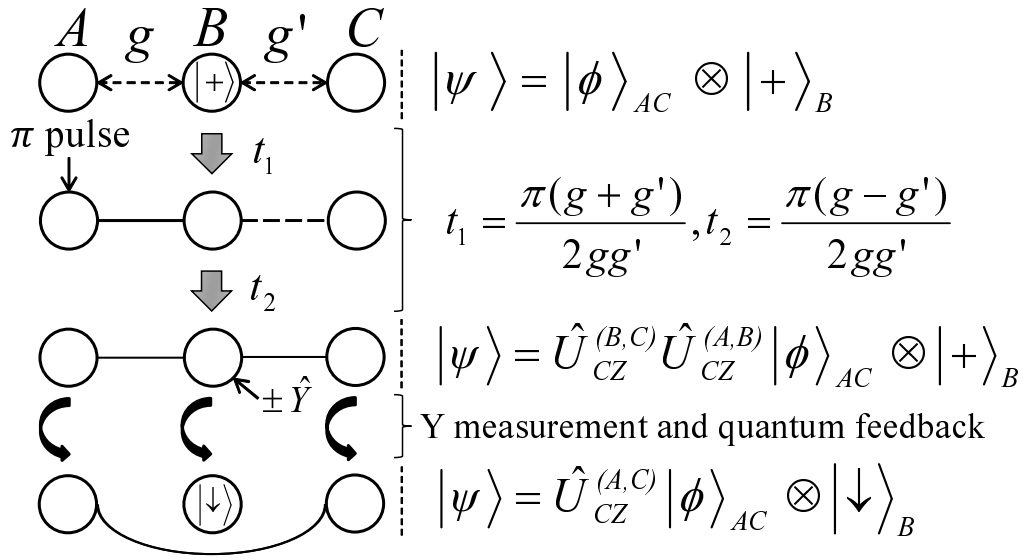

Figure 3.6: Controlled-phase operations using a spin echo technique with asymmetric coupling strength. $\hat{U} = \hat{U}_{CZ}^{(A,B)} \hat{U}_{CZ}^{(B,C)}$ is performed on the initial state at a specific timing due to the implementation of a π pulse where $\hat{U}_{CZ}^{(j,k)}$ denotes a controlled-phase operation between qubit j and k.

denotes Ising type interactions between qubit A, B and B, C. By trace out of the ancillary qubit B, we can treat the effects of the interactions $\hat{H}$ as dephasing errors at most $\epsilon_m \sigma_Z$ on the qubit A and C. Such error can be corrected by the quantum error correction as long as the error is less than the threshold.

3.3.6 Asymmetric coupling strength case

Interestingly, our scheme to perform controllable controlled-phase gates under the effect of always-on interaction works even when the coupling strength between qubits is different. We adopt a spin echo technique [26, 105, 62] to balance the interaction. In the spin echo technique, implementation of a π pulse can refocus the dynamics of the spin, so that the effect of the interaction should be canceled. Suppose that we have three qubits in a raw, and the coupling strengths between the nearest neighbor qubits are $g_{(A,B)}$ and $g'_{(B,C)}$ as shown in Fig. 3.6 where we assume $g_{(A,B)} > g'_{(B,C)}$ without loss of generality. Then, the system Hamiltonian

becomes as follows.

$$\begin{aligned}\hat{H} &= \sum_{j=A,B,C}\Big(\frac{\omega_j}{2}\hat{Z}_j + \lambda_j(t)\cos\big(\omega_j' t+\theta\big)\hat{X}_j\Big) \\ &\quad + \frac{g_{(A,B)}}{4}\hat{Z}_A\hat{Z}_B + \frac{g'_{(B,C)}}{4}\hat{Z}_B\hat{Z}_C \qquad (3.53)\\ &\simeq g_{(A,B)}\frac{\mathbf{1}+\hat{Z}_A}{2}\frac{\mathbf{1}+\hat{Z}_B}{2} + g'_{(B,C)}\frac{\mathbf{1}+\hat{Z}_B}{2}\frac{\mathbf{1}+\hat{Z}_C}{2} \qquad (3.54)\end{aligned}$$

with

$$\begin{aligned}\omega_A' &= \omega_A - \frac{1}{2}g_{(A,B)}, \omega_B' = \omega_B - \frac{g_{(A,B)}+g'_{(B,C)}}{2},\\ \omega_C' &= \omega_C - \frac{1}{2}g'_{(B,C)}, \lambda_A = \lambda_B = \lambda_C = 0. \qquad (3.55)\end{aligned}$$

Here, we introduce

$$t_1 = \frac{\pi(g_{(A,B)}+g'_{(B,C)})}{2g_{(A,B)}g'_{(B,C)}} \qquad (3.56)$$

and

$$t_2 = \frac{\pi(g_{(A,B)}-g'_{(B,C)})}{2g_{(A,B)}g'_{(B,C)}} \qquad (3.57)$$

to satisfy

$$g_{(A,B)}(t_1-t_2) = g'_{(B,C)}(t_1+t_2) = \pi. \qquad (3.58)$$

We let the state evolve for a time t_1, perform π pulse to qubit A, and let the state evolve for a time t_2. The total unitary evolution can be described by

$$\hat{U} = \exp\left(-ig_{(A,B)}(t_1-t_2)\frac{\mathbf{1}+\hat{Z}_A}{2}\frac{\mathbf{1}+\hat{Z}_B}{2} - ig'_{(B,C)}(t_1+t_2)\frac{\mathbf{1}+\hat{Z}_B}{2}\frac{\mathbf{1}+\hat{Z}_C}{2}\right), \qquad (3.59)$$

up to local equivalent, and so,

$$\hat{U}|\phi\rangle_{ABC} = \hat{U}_{CZ}^{(B,C)}\hat{U}_{CZ}^{(A,B)}|\phi\rangle_{ABC}, \qquad (3.60)$$

so that we can perform controlled-phase gates even if the coupling strength is asymmetric. The details are explained in Subsection 3.3.7.

After this evolution, we use projective measurements and quantum feedforward to effectively turn off the interaction as long as qubit B is prepared in a ground state. Therefore, we succeed in performing controlled-phase operation between qubit A and C.

3.3.7 The details of implementation of controlled-phase gate

Here, we show the details of our scheme to perform controlled-phase gate. We set the initial state of the system as following.

$$|\Psi_1\rangle \quad = \quad |+\downarrow+\rangle_{ABC}. \tag{3.61}$$

From the Hamiltonian $\hat{H}'$ in Eq. (3.38), we define the following local Hamiltonians.

$$\hat{H}'_A = g_{(A,B)}\frac{\mathbf{1}+\hat{Z}_A}{2}, \hat{H}'_C = g'_{(B,C)}\frac{\mathbf{1}+\hat{Z}_C}{2}. \tag{3.62}$$

Firstly, we perform $\frac{\pi}{2}$ pulse to the qubit B, so that we can obtain the following state

$$|\Psi_2\rangle \quad = \quad |+++\rangle_{ABC}. \tag{3.63}$$

Secondly, we let the state evolve for a time t_1 in Eq. (3.56). The state becomes as follows.

$$|\Psi_3\rangle \quad = \quad \frac{1}{\sqrt{2}}(|\downarrow\rangle_B + e^{i(\hat{H}'_A+\hat{H}'_C)t_1}|\uparrow\rangle_B) \otimes |{+}{+}\rangle_{AC} \tag{3.64}$$

Thirdly, we perform π pulse to the qubit A to balance the effects of interaction strengths.

$$|\Psi_4\rangle = \frac{1}{\sqrt{2}}(|\downarrow\rangle_B|{+}{+}\rangle_{AC} + \hat{X}_A e^{i(\hat{H}'_A+\hat{H}'_C)t_1}|\uparrow\rangle_B|{+}{+}\rangle_{AC}) \tag{3.65}$$

Fourthly, we let the state evolve for a time t_2 in Eq. (3.57). Controlled-phase gates are performed between two pairs of qubits as follows.

$$
\begin{aligned}
|\Psi_5\rangle &= \frac{1}{\sqrt{2}}(|\downarrow\rangle_B|{+}{+}\rangle_{AC} + e^{i(\hat{H}'_A+\hat{H}'_C)t_2}\hat{X}_A e^{i(\hat{H}'_A+\hat{H}'_C)t_1}|\uparrow\rangle_B|{+}{+}\rangle_{AC}) && (3.66)\\
&= \frac{1}{\sqrt{2}}(|\downarrow\rangle_B|{+}{+}\rangle_{AC} + \hat{X}_A e^{i\hat{H}'_A(t_1-t_2)}e^{i\hat{H}'_C(t_1+t_2)}|\uparrow\rangle_B|{+}{+}\rangle_{AC}) && (3.67)\\
&= \frac{1}{\sqrt{2}}(|\downarrow\rangle_B|{+}{+}\rangle_{AC} - |\uparrow\rangle_B|{-}{-}\rangle_{AC}). && (3.68)
\end{aligned}
$$

Finally, we measure the qubit B on Y-basis. According to the measurement result, the states becomes as follows.

$$
\begin{aligned}
|\Psi_6^{\pm}\rangle &= \frac{1}{2}((|\uparrow\rangle_B \pm i|\downarrow\rangle_B)|{+}{+}\rangle_{AC} \mp i(|\uparrow\rangle_B \pm i|\downarrow\rangle_B)|{-}{-}\rangle_{AC}) && (3.69)\\
&= \frac{1}{\sqrt{2}}|\pm 1_{\hat{Y}}\rangle_B \otimes (|{+}{+}\rangle_{AC} \mp i|{-}{-}\rangle_{AC}). && (3.70)
\end{aligned}
$$

The operation of quantum feedforward is determined according to the measurement result. These operations are equivalent to perform a controlled-phase gate between qubits A and C as follows.

$$
\begin{aligned}
|\Psi_7^{\pm}\rangle &= \hat{F}^{\pm}_{ABC}|\Psi_6^{\pm}\rangle && (3.71)\\
&= \frac{1}{\sqrt{2}}\hat{U}_B^{\frac{\mp\pi}{2},\hat{X}}|\pm 1_{\hat{Y}}\rangle_B \otimes \hat{S}^{\pm}_A\hat{S}^{\pm}_C(|{+}{+}\rangle_{AC} \mp i|{-}{-}\rangle_{AC}) && (3.72)\\
&= \frac{1}{\sqrt{2}}(|\uparrow -\rangle_{AC} - |\downarrow +\rangle_{AC}) \otimes |\downarrow\rangle_B && (3.73)\\
&= \hat{U}_{CZ}^{(A,C)}|\Psi_1\rangle. && (3.74)
\end{aligned}
$$

3.3.8 One dimensional cluster state

We only explain about three-qubit case here. However, it is straightforward to generalize this idea to an arbitrary size of one-dimensional cluster state, because we can ignore the coupling from the other qubits as long as we insert an ancillary qubit prepared in an ground state as we discussed before. It is worth mentioning that the necesary number of the π pulses increases linearly against the number of the qubits, due to the use of such ancillary qubits to stop the interaction from the other qubits. Additionally, our scheme can be applied to two or three-dimensional

cluster state. In these cases, we repeatedly implement the similar procedure as we use in the case of a one-dimensional cluster state, so that we can balance the interactions just by adding a few operations. We discuss the details of those interaction-balancing schemes in Section 3.6. Hence, throughout of this chapter, we assume that all interactions are equal.

3.4 Generation of a two dimensional cluster state under the effect of always-on interaction for surface coding scheme

In this section, we show how to apply our scheme to generate a two-dimensional cluster state, which is a universal resource [87, 84] for quantum computation. We

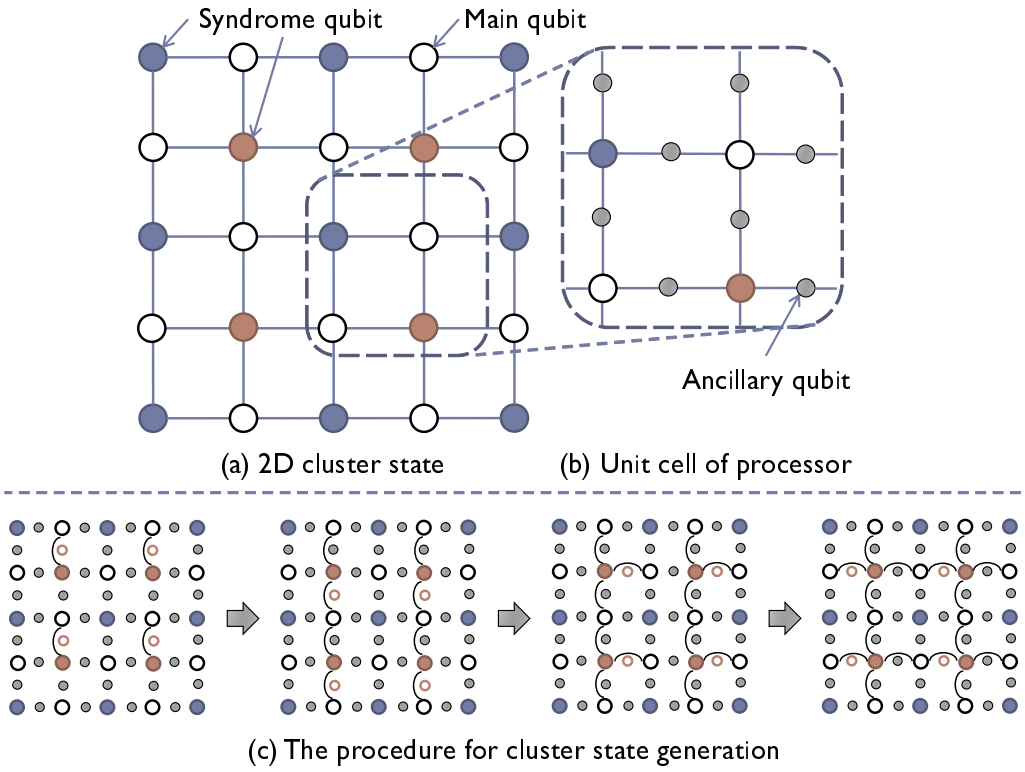

Figure 3.7: (a)Schematic to generate a two-dimensional cluster state with always-on interaction using our scheme. Hollow circles denote logical qubits and colored circles denote syndrome qubits for surface coding scheme. (b) A unit cell to generate a two-dimensional cluster state. The large circles denote main qubits while the small circles denote ancillary qubits for switching interactions. The edge between the qubits denote the Ising type interaction between those qubits.

now give the overview of our setting in Fig. 3.7(a) and the physical implementation in Fig. 3.7(b). Ancillary qubits for effectively turning on/off interactions are set on the midpoint of these main qubits. There are Ising type interactions between each pair of nearest neighbor main qubit and ancillary qubit. To generate a whole two-dimensional cluster state, we need to perform controlled-phase operations between every pair of the nearest logical and syndrome qubits as described in the following procedure. Firstly, we prepare all ancillary qubits between main and syndrome qubit to $|+\rangle$ state. Secondly, we let the states evolve for a time $t = \frac{\pi}{g}$. Finally, we perform projective measurements and quantum feedforward operations to all ancillary qubits for generating two-dimensional cluster state. In these operations, each ancillary qubit has no effect on the state of other ancillary qubits, so that we can handle the effect of each operation as individual three-qubits system and we can proceed all controlled-phase operations simultaneously. Furthermore, similar to the case of a one-dimensional cluster state, the energies of ancillary qubits have unknown energy shifts as described in Table 3.1, so that the upper bound fidelities and optimal interaction strengths of each controlled-phase operations coincide with three-qubit case shown in Fig. 3.5(a). Since scalable surface coding scheme require the error rate around below 1 %, this result shows that the Rabi frequency should be tens of thousands times larger than the decay rate ($\frac{1}{T_2}$) and the coupling strength should be thousands times larger than that.

3.5 Generation of a three dimensional cluster state under the effect of always-on interaction for topological quantum computation

Although we discussed how to generate a two-dimensional cluster state above, we can apply our scheme to generate a three-dimensional cluster state, which is a universal resource for the topological quantum computation [83].

We can use either a cubic cluster state or bilayer cluster state for the topological quantum computation, and we choose the latter one to avoid an unnecessary decoherence effect, as previous authors did [73]. In this case, it is necessary to generate the bilayer cluster state again and again, after the implementation of

the measurements on one of the layers. We discuss how to generate a bilayer 3D cluster state under the effect of always-on Ising interaction by using projective measurements and quantum feedforward. We again assume that the Ising type Hamiltonian described in Eq. 3.12 dominates this system, and there is an interaction between every nearest neighbor qubit pairs. In our approach, unit cell to generate a bilayer three-dimensional cluster state is composed of 28 qubits (6 main qubits and 22 ancillary qubits), and we repeatedly put these cells on the same plane as shown in the Fig. 3.8. Interestingly, although these qubits are located in a two-dimensional plane, it becomes possible to implement a 3D topological quantum computation.

Let us consider qubits located on the cross-shape structure, which is a part of the unit cell (See the illustration (c) in the Fig. 3.8). The 5 ancillary qubits are used to implement a controlled-phase gate between an arbitrary pair of two main qubits in this cross shape structure without changing the states of the other main qubits. Interestingly, by preparing two of the ancillary qubits in ground states and preparing the other ancillary qubits in the $|+\rangle$ state as described in Fig. 3.8, only two main qubits will be involved in the implementation of the controlled-phase gate while the other main qubits do not affect the operation due to the existence of the ancillary qubits prepared in a ground state, which has the same analogy with the case of a one-dimensional cluster state.

3.5.1 Optimal interaction strength

Next, we estimate the optimal interaction strength of the above system for generating a three-dimensional cluster state. We consider the same noise as in 3.3.5. For this estimation, we introduce the following setup. As described in Fig. 3.8, we use three ancillary qubits inserted between the target main qubits for performing controlled-phase gate. We name these qubits as qubit A, B, C, D, and E where A and E denote the main qubits and B, C, and D denote ancillary qubits (See Fig. 3.9).

Initially, all ancillary qubits are prepared in a ground state and main qubit are prepared in arbitrary states. We evaluate the error accumulation during the

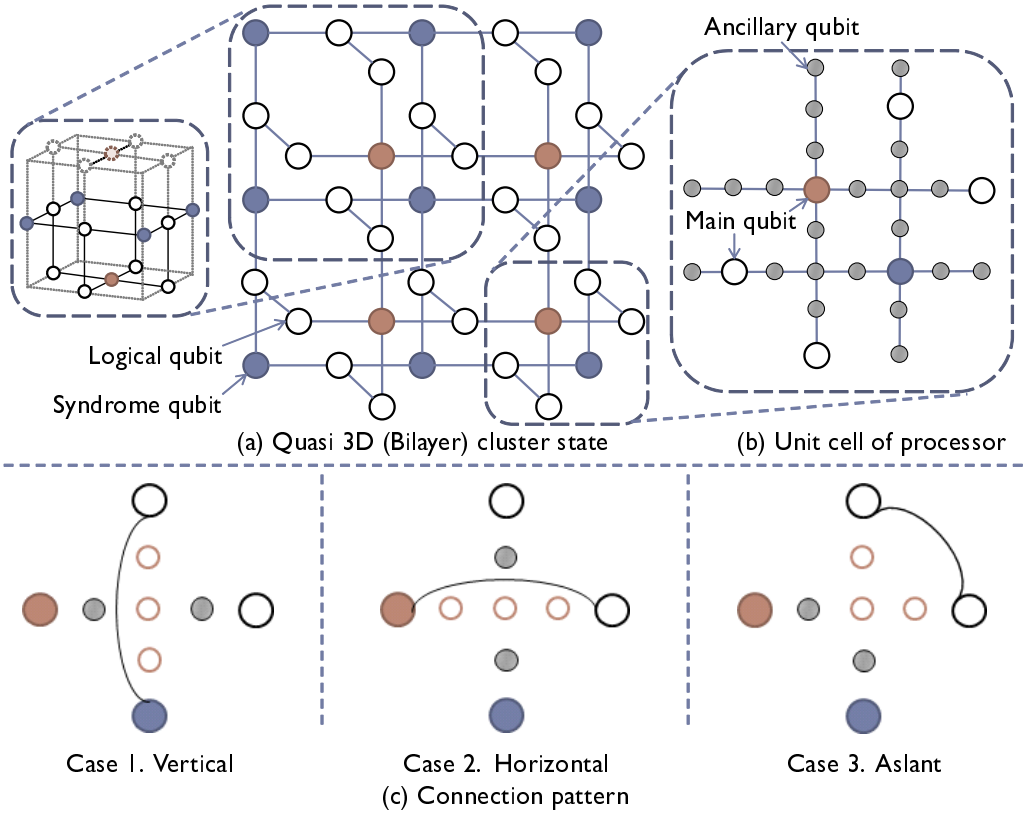

Figure 3.8: (a)Schematic to perform 3D topological quantum computation in our scheme by using qubits embedded in a two-dimensional plane. (b) Unit cell to generate a bilayer 3D cluster state. We repeatedly put this cell in the two-dimensional plane. The large circles denote main qubits while small circles denote ancillary qubits. The edge between the qubits denotes the interaction between them. (c) Cross-shape structure composed of 4 main qubits and 5 ancillary qubits. We can implement a controlled-phase gate operation between an arbitrary pair of main qubits in this structure.

implementation of a controlled-phase gate in our scheme using three ancillary qubits (Fig. 3.9). Firstly, by performing $\frac{\pi}{2}$ pulse, we rotate the ancillary qubit C into $|+\rangle$ state, and subsequently rotate the other ancillary qubit B and D into $|+\rangle$ state. In this case, since all nearest neighbor qubits for the qubit C are prepared in a ground state, the qubit C is not affected by the coupling strength from any other qubits and can be accurately rotated by a microwave resonant pulse. However, the qubit B (D) have unknown energy shift due to the coupling from qubit A (E) and C during the rotation, so that a detuning error occurs.

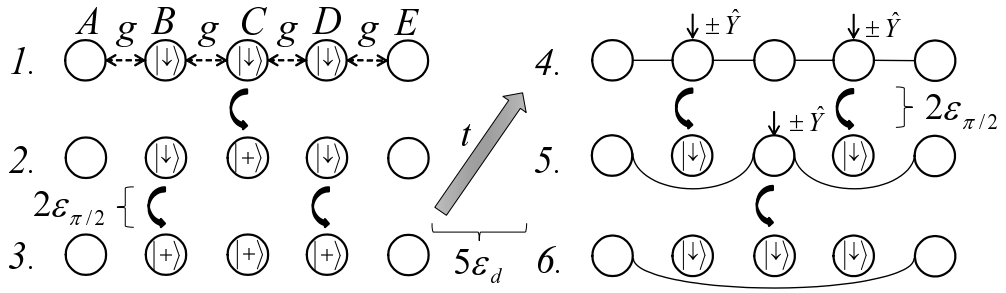

Figure 3.9: Error accumulation during the implementation of a controlled-phase gate between the main qubits. There are two main qubits A and E initially prepared in arbitrary state. Between these qubits, we insert three ancillary qubits B, C, and D initially prepared in a ground state. As long as the state of the nearest neighbor qubit contains a superposition, we cannot determine a resonant frequency of the qubit due to the always-on interaction, which induces a detuning error $\epsilon_{\frac{\pi}{2}}$ to rotate the qubit. Also, we assume a decoherence error ϵ_d that occurs during the time evolution to entangle nearest neighbor qubits by the interaction.

Secondly, we wait the appropriate time evolution of system with the Hamiltonian. During this time evolution, decoherence error of every qubit accumulates. Finally, we measure $\hat{Y}$ and perform quantum feedforward on the qubit B and D, and subsequently implement the same operation on the qubit C. Again, due to the coupling from nearest neighbor qubits, qubit B and D suffers the detuning error for the feedforward rotations while the qubit C can be accurately rotated by a resonant microwave pulse. To generate a whole three-dimensional cluster state, we should perform this type of controlled-phase gates, vertically, horizontally, and aslantly, as shown in Fig. 3.8. During this 3 steps, additional decoherence error accumulate. Therefore, we calculate and plot an achievable fidelity

$$F = 1 - (4\epsilon_{\frac{\pi}{2}} + 15\epsilon_d) \tag{3.75}$$

in Fig. 3.10. Also, we plot the optimal interaction strength and an achievable fidelity against each λ in Fig. 3.5(b). Since scalable topological quantum computation require the error rate around below 1 %, this result shows that the Rabi frequency should be tens of thousands times larger than the decay rate and the coupling strength should be thousands times larger than that.

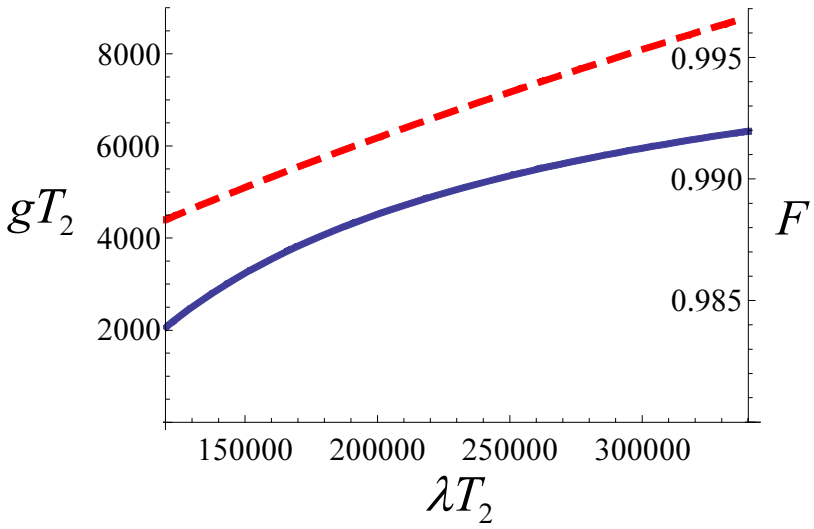

Figure 3.10: The optimal coupling strength (gT_2) and an achievable fidelity of a controlled-phase operation in our scheme using three ancillary qubits against the Rabi frequency (λT_2). The solid line denotes F and the dashed line denotes gT_2. as with Fig. 3.5(a).

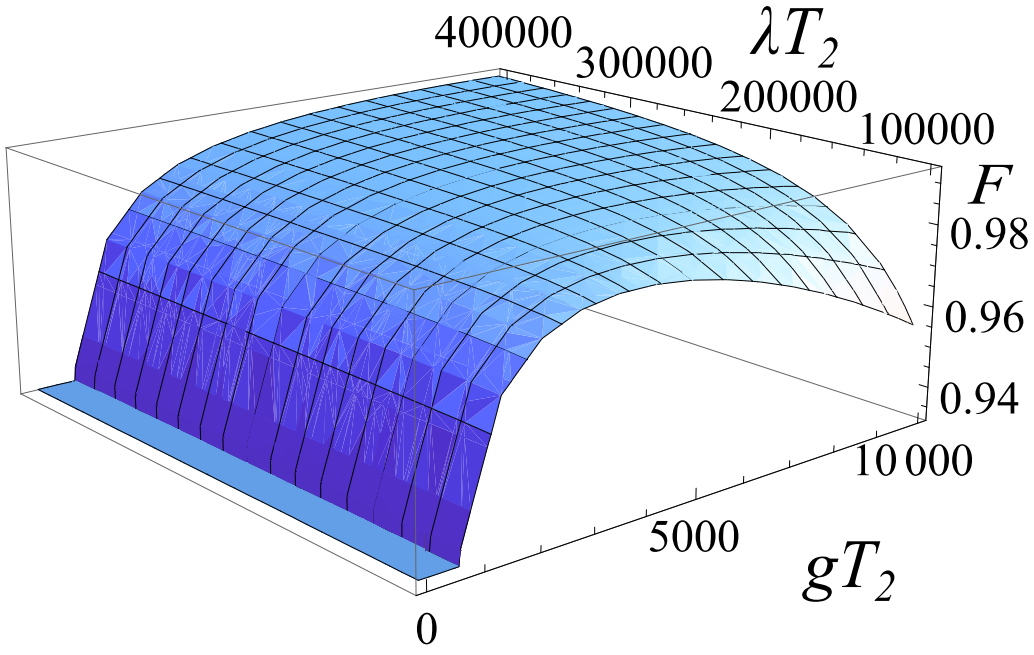

Figure 3.11: An achievable fidelity (F) of a controlled-phase operation in our scheme using three ancillary qubits against interaction strength (gT_2) and Rabi frequency (λT_2).

3.6 Generating cluster state with asymmetric interaction strength

In this section, we discuss how to generate a cluster state with asymmetric coupling strength. Suppose that only three qubits are involved in, and the other qubits are set not to interact with these three qubits by controlling the state of the ancillary qubits. As we described before, by using unitary evolution, implementation of a spin echo, quantum measurements and quantum feedforward, we can perform a controlled-phase gate between two main qubits where a single ancillary qubit is inserted between two main qubits for this case. This is a two-step elementary operation to implement controlled-phase gate between main qubits under the effect of always-on interaction. We will use this operation recursively to make a large cluster state.

3.6.1 Generating one-dimensional cluster state

First, we aim for generating a one-dimensional cluster state using qubits that are arranged in a raw. In order to avoid an exponentially large number of implementations of π pulses, we use the two-step procedure for generating one-dimensional cluster state with m main qubits and $m-1$ ancillary qubits as shown in Fig. 3.12. In this setting, interaction strengths differ from each other. Firstly, we perform

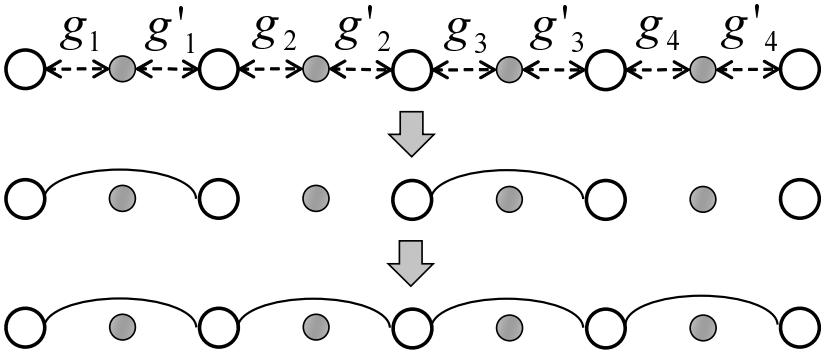

Figure 3.12: Due to the ancillary qubits prepared in a ground state, the number of qubits interacting with the main qubit is equal to or less than one, so that we can use the scheme described in Fig. 3.6. We create $\frac{m}{2}$ bell pairs in the first step, and create a one-dimensional cluster state in the second step. This makes the necessary number of π pulses the same as the number of ancillary qubits.

controlled-phase operation between $2n-1^{\text{th}}$ main qubit and $2n^{\text{th}}(n=1,2,..,\frac{m}{2})$ main qubit, so that $\frac{m}{2}$ bell pairs are created. Since the $2k^{\text{th}}(k=1,2,..,\frac{m}{2})$ ancillary qubits are prepared in a ground state, we only need to consider the dynamics of three-qubit during the time evolution, and so we can apply the scheme to turn on/off effective interaction for three-qubit case as described in Fig. 3.2. Secondly, we perform controlled-phase operations between $2n^{\text{th}}$ main qubit and $2n+1^{\text{th}}$ main qubit, so that a one-dimensional cluster state can be created. Here, the $2k-1^{\text{th}}$ ancillary qubits are in a ground state, and $2k^{\text{th}}$ ancillary qubits interact with two main qubits. Again, only three qubits interact with each other, and so we can apply the scheme described in Fig. 3.2.

3.6.2 Generating a two-dimensional cluster state

Next, we aim for generating a two-dimensional cluster state using m^2 main qubits and $2m(m-1)$ ancillary qubits that are arranged on two-dimensional lattice with asymmetric coupling strength. For this purpose, we suggest a four-step procedure as shown in Fig. 3.13. Firstly, we generate $\frac{m}{2}$ Bell-pairs between each nearest pairs

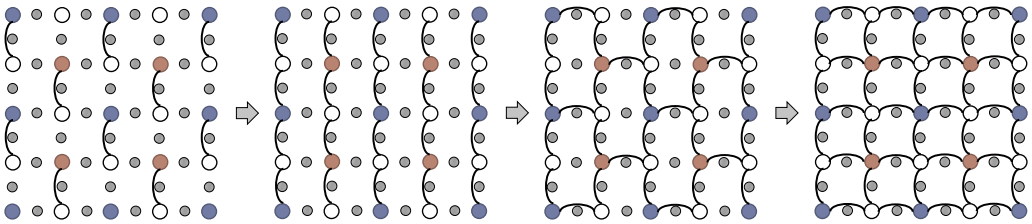

Figure 3.13: The procedure for generating a two-dimensional cluster state over logical qubits and syndrome qubits. At each step, every main qubits effectively interacts with at most one nearest-neighbor ancillary qubit, because the other nearest-neighbor ancillary qubit is prepared in a ground state, so that the interaction of these are effectively turned off. In this figure, large circles denote main qubits while small circles denote ancillary qubits. Main qubits are classified for three-types of qubits. White big circles denote logical qubits, blue (red) big circles denote syndrome qubits for bit-flip detection (dephasing detection).

of logical and syndrome qubits at each column. At every step, ancillary qubits, which are not used for controlled-phase operations, prepared in ground state. Secondly, we perform controlled-phase operations between each Bell-pairs in the

same column to generate one-dimensional cluster states. Thirdly, we perform controlled-phase operations in horizontal direction. At each controlled-phase operation, the syndrome qubit is arranged at the left side and the logical qubit is arranged at the right side. Finally, we perform controlled-phase operation between all the remaining nearest-neighbor pair of logical and syndrome qubits, so that we can obtain a two-dimensional cluster state.

3.6.3 Generating a three-dimensional cluster state

In this subsection, we suggest a procedure to make a three-dimensional cluster state as shown in Fig. 3.14. For this procedure, we use $\frac{3}{2}m^2$ main qubits and $\frac{11}{2}m^2$

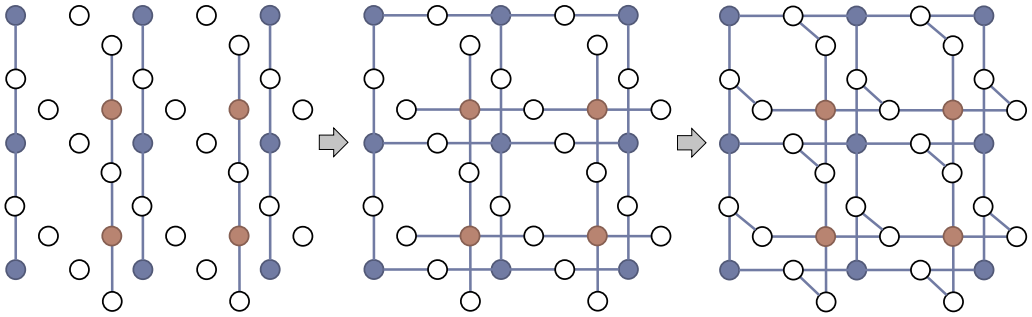

Figure 3.14: Only main qubits are presented in this figure. Firstly, we generate one-dimensional cluster states using logical and syndrome qubits on the same column. Secondly, we generate two separable two-dimensional graph states. Finally, we generate a three-dimensional cluster state.

ancillary qubits that are arranged on a two-dimensional plane with asymmetric coupling strength. Here, we show how to perform controlled-phase operation between two-main qubits A and E via three-ancillary qubits B, C, and D with asymmetric interactions as in Fig. 3.15. Firstly, we perform controlled-phase operation between qubit A and C using our technique in Fig. 3.6. Secondly, we perform controlled-phase operation between qubit C and E using the same technique. Finally, we perform $\hat{Y}$ basis measurement quantum feedforward operations on qubit C, so that controlled-phase operation can be implemented between qubit A and E. We use this three-step controlled-phase operation recursively to make a large three-dimensional cluster state in following procedure.

The details of procedure for generating a three-dimensional cluster state are described as follows. Firstly, we generate m-qubit one-dimensional cluster states composed of $\frac{m}{2}$ logical qubits and $\frac{m}{2}$ syndrome qubits in vertical direction. For these operations, we use the same process as described in Subsection 3.6.1. Secondly, we generate two separable two-dimensional graph states as shown in Fig. 3.15. One of the two-dimensional cluster state is composed of logical qubits and bit-flip-detection syndrome qubits. The other one is composed of logical qubits and dephasing-detection syndrome qubits. Interactions between these two-dimensional cluster states are effectively turned off by ancillary qubits prepared in a ground state. Finally, we perform controlled-phase operations on a slant direction as shown in Fig. 3.8(c) between pairs of logical qubits to connect these two-dimensional cluster states, so that we can generate a three-dimensional cluster state.

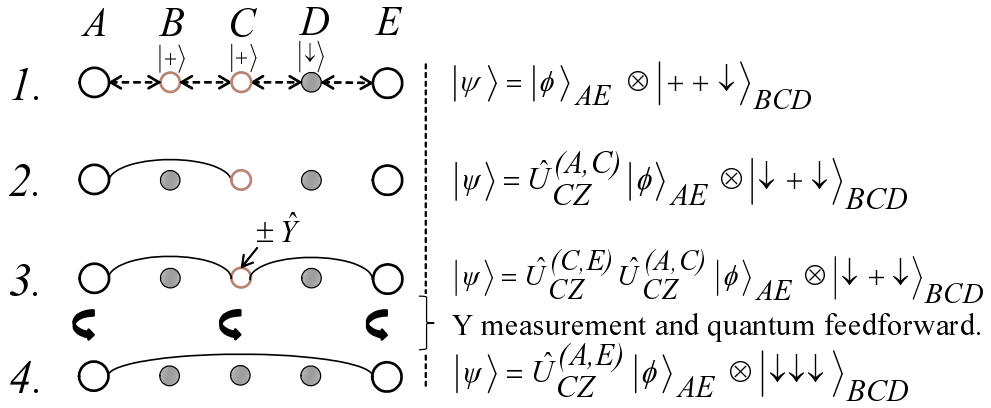

Figure 3.15: Controlled-phase operations via three-ancillary qubits using our technique with asymmetric coupling strength. Qubit A and E are main qubits, and qubit C, D, and E are ancillary qubits. Firstly, we prepare ancillary qubits D to ground state. Secondly, we perform controlled-phase operation between qubit A and C by applying our technique described in Fig. 3.6. Thirdly, we perform controlled-phase operation between qubit C and E in the same way. Finally, we perform $\hat{Y}$ basis measurements to qubit C and feedforward operations.

3.7 Experimental parameters

We show the optimal interaction strength gT_2 and Rabi frequency λT_2 for our scheme in Subsection 3.5.1. The best observed coherence time of the flux qubit is 10 or 20 μs [18, 101]. In these demonstration, flux qubits are located in the middle of the three-dimensional microwave cavity. Furthermore, the Rabi frequency with 1.7 GHz [114] and the interaction strength with 0.5 GHz [66] are demonstrated. In the former case, the flux qubit is strongly inductively-coupled with a microwave line and has a large anharmonicity. Hence, the Rabi frequency can be up to an order of few GHz without significant additional decoherence. In the latter case, two flux qubits are located on the same circuit with fixed coupling. Assuming that we can achieve these results on the same system, gT_2 and λT_2 can be up to 10000 and 34000 (with $T_2 = 20\mu$s). As shown in Fig. 3.5(b) and Fig. 3.11, these values satisfy conditions of the fidelity $F \geq 0.99$ which exceed the threshold for fault-tolerant quantum computation.

3.8 Conclusion

In this chapter, we show a scalable way to generate two and three-dimensional cluster state with always-on Ising interaction. Here, we use projective measurements and quantum feedforward to effectively turn on/off the interaction in this system. Our schemes provide a novel way to construct a surface code quantum computation and topological quantum computation.

Chapter 4

Toward the realization of generating Ising interaction using capacitive coupling for superconducting flux qubits

4.1 Introduction

In this Chapter, we propose a scheme to generate a controllable Ising interaction between superconducting flux qubits. Existing schemes rely on inductive couplings to realize Ising interactions between flux qubits, and the interaction strength is controlled by an applied magnetic field. We have found an alternative way to generate an interaction between the flux qubits via capacitive couplings. This has an advantage in individual addressability, because we can control the interaction strength by changing an applied voltage that can be easily localized. This is a crucial step toward realizing superconducting flux qubit quantum computation.

The rest of this chapter is organized as follows: In Section 4.2, we describe the experimental setup for simulations. In Section 4.3, we present the design details of our flux qubit and the effects on a flux qubit from changes to the parameters. In Section 4.4, we propose our scheme for generating Ising type interaction between capacitively coupled superconducting flux qubits. Moreover, we show the relationship between coupling strength and two types of errors caused by operation accuracy, the fluctuation of applied voltage and timing jitter. In

Section 4.5, we present the analysis of our scheme for use in a multi-qubit system. Additionally, we discuss how to suppress the non-nearest neighbor interactions by changing parameters and performing π pulses. Finally, we show our procedure for generating a one and two-dimensional cluster state using qubits on a square lattice in constant steps.

4.2 Experimental setup

Experiments for Hamiltonian analysis are carried out in Matlab R2013a on a Linux server with Intel Xeon X5675 processors at 3.07 GHz (6 physical cores) and 288GB of main memory. In each simulation, wave functions are represented to as 13x13 matrices in the momentum space.

4.3 Voltage controlled α-tunable flux qubit

Let us first show the circuit of a flux qubit that we propose in Fig. 4.1. Here,

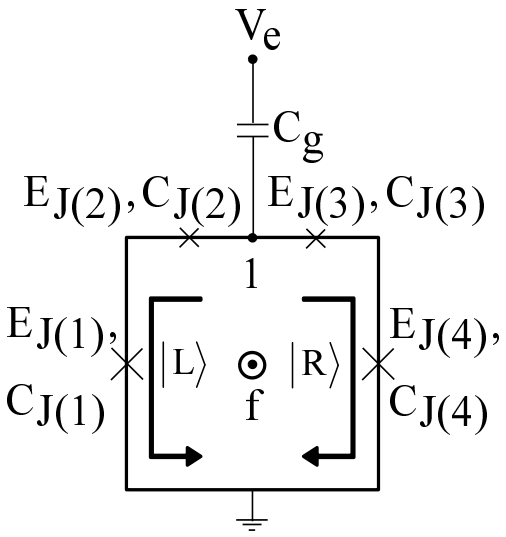

Figure 4.1: The circuit of a flux qubit in our design. This flux qubit has four Josephson junctions (JJ). $E_{J(n)}$ and $C_{J(n)}$ denote the Josephson energy and capacitance of the n th Josephson junction JJn. The loop is threaded by an external magnetic flux f, and we can control the energy bias of the qubit via the magnetic flux. Node 1 represents the superconducting island. The electric potential of node 1 is V_I.

X-shaped crosses denote Josephson junctions (JJ). The first Josephson junction (JJ1) and the fourth Josephson junction (JJ4) both have the same Josephson coupling energies E_J and capacitances C_J. The second Josephson junction (JJ2) and the third Josephson junction (JJ3) both have the same Josephson energies and capacitances, α times larger than those of JJ1 and JJ4.

4.3.1 Hamiltonian

The Josephson phases φ_n, which are given by the gauge-invariant phase of each JJn, are subject to the following equation:

$$\varphi_1 + \varphi_2 + \varphi_3 + \varphi_4 = -2\pi f \tag{4.1}$$

due to fluxoid quantization around the loop containing phases of Josephson junctions. f denotes the external magnetic flux through the loop of the qubit in units of the magnetic flux quantum

$$\Phi_0 = \frac{h}{2e}. \tag{4.2}$$

The Josephson enegy of each JJn is

$$U_n = E_{J(n)}(1 - \cos\varphi_n). \tag{4.3}$$

Then, the total Josephson energy U can be described as follows:

$$U = \sum_{k=1}^{4} E_{J(k)} \left(1 - \cos\varphi_k\right). \tag{4.4}$$

The capacitance energy of each JJn is

$$T_n = \frac{1}{2} C_{J(n)} \left(\frac{\Phi_0}{2\pi}\right)^2 \dot{\varphi}_i^2 \tag{4.5}$$

where $\dot{\varphi}$ denotes the time derivative of φ. Then, including the energy of voltage application, the total electric energy T can be described as follows:

$$T = \frac{1}{2}\sum_{k=1}^{4} C_{J(k)} \left(\frac{\Phi_0}{2\pi}\dot{\varphi}_k\right)^2 + \frac{1}{2}C_g \left(V_e - V_I\right)^2 \tag{4.6}$$

where C_g, V_e and V_I denote the capacitance of the gate capacitor, applied external voltage and the electric potential of node 1, respectively. Here, node 1 represents the superconducting island.

From the phase constraints in (4.1), each phase φ_k and the time derivative of phase $\dot{\varphi}_k$ can be described using φ' and $\dot{\varphi}'$ as follows:

$$\varphi = \begin{pmatrix} \boldsymbol{\varphi_1} \\ \boldsymbol{\varphi_2} \\ \boldsymbol{\varphi_3} \\ \boldsymbol{\varphi_4} \end{pmatrix}, \ \varphi_k = \sum_j B_{kj}\varphi'_j + F_k, \varphi' = \begin{pmatrix} \boldsymbol{\varphi'_1} \\ \boldsymbol{\varphi'_2} \\ \boldsymbol{\varphi'_3} \end{pmatrix}, \tag{4.7}$$

$$\dot{\varphi} = \begin{pmatrix} \boldsymbol{\dot{\varphi}_1} \\ \boldsymbol{\dot{\varphi}_2} \\ \boldsymbol{\dot{\varphi}_3} \\ \boldsymbol{\dot{\varphi}_4} \end{pmatrix}, \ \dot{\varphi}_k = \sum_j B_{kj}\dot{\varphi}'_j, \dot{\varphi}' = \begin{pmatrix} \boldsymbol{\dot{\varphi}'_1} \\ \boldsymbol{\dot{\varphi}'_2} \\ \boldsymbol{\dot{\varphi}'_3} \end{pmatrix}, \tag{4.8}$$

Here, we introduce the following terms B and F

$$B = \begin{pmatrix} \mathbf{1} & \mathbf{0} & \mathbf{0} \\ \mathbf{0} & \mathbf{1} & \mathbf{0} \\ \mathbf{0} & \mathbf{0} & \mathbf{1} \\ \mathbf{-1} & \mathbf{-1} & \mathbf{-1} \end{pmatrix}, F = \begin{pmatrix} \mathbf{0} \\ \mathbf{0} \\ \mathbf{0} \\ \boldsymbol{-2\pi f} \end{pmatrix}. \tag{4.9}$$

Then, we can rewrite the total Josephson energy U as follows:

$$U = E_J \sum_k A_k(1 - \cos\varphi_k) \tag{4.10}$$

$$= E_J \sum_k A_k(1 - \cos(\sum_j B_{kj}\varphi'_j + F_k)) \tag{4.11}$$

Here, we introduce the area ratio A_n of each JJn as follows:

$$A_1 = A_4 = 1,\ A_2 = A_3 = \alpha. \tag{4.12}$$

Then, the capacitance and the critical current of each Josephson junction are proportional to A_j.

We define V_j as the voltage difference between JJ_j and JJ_{j+1}. The voltage of the ground is set to virtual zero. Then the electric potential of node 1 (V_I) becomes

$$V_I = V_2 = \frac{\Phi_0}{2\pi}(\dot{\varphi}_1 + \dot{\varphi}_2). \tag{4.13}$$

Furthermore, each V_j can be described using matrix D as follows:

$$V = \begin{pmatrix} \boldsymbol{V_1} \\ \boldsymbol{V_2} \\ \boldsymbol{V_3} \end{pmatrix},\ V_j = \sum_i D_{ji} \left(\frac{\Phi_0}{2\pi}\right) \dot{\varphi}_i,\ D = \begin{pmatrix} \mathbf{1} & \mathbf{0} & \mathbf{0} & \mathbf{0} \\ \mathbf{1} & \mathbf{1} & \mathbf{0} & \mathbf{0} \\ \mathbf{1} & \mathbf{1} & \mathbf{1} & \mathbf{0} \end{pmatrix}. \tag{4.14}$$

From the formula (4.6), the total electric energy T becomes as follows:

$$T = \sum_k \frac{A_k e^2}{4E_C} \left(\frac{\Phi_0}{2\pi}\dot{\varphi}_k\right)^2 + \sum_i \frac{1}{2} C_{gi} \left(V_{Ei} - V_I\right)^2 \tag{4.15}$$

$$= \sum_k \frac{e^2}{4E_C} \left(\frac{\Phi_0}{2\pi}\right)^2 A_k \left(\sum_i B_{ki}\dot{\varphi}'_i\right)^2 + \frac{1}{2} C_g \left(V_{Ei} - \sum_{jk} D_{i,j} B_{j,k} \dot{\varphi}'_j \frac{\Phi_0}{2\pi}\right)^2 \tag{4.16}$$

where C_{gi} denotes the capacitance of the gate capacitor which is connected to the island between JJ_i and JJ_{i+1}. V_{Ei} denotes the external voltage to the same island. In this case, C_{g2} and V_{Ei} are C_g and V_e in Fig. 4.1. Here, we introduce the ratio of capacitance C_{gi} as follows:

$$\Gamma_1 = \Gamma_3 = 0,\ \Gamma_2 = \gamma. \tag{4.17}$$

Γ_i satisfies the following conditions

$$C_{gi} = C_{J(1)}\Gamma_i = \frac{e^2}{2E_C}\Gamma_i. \tag{4.18}$$

Then, the second term of formula (4.16) becomes

$$\begin{aligned} & \frac{e^2}{4E_C}\left(\frac{\Phi_0}{2\pi}\right)^2 \sum_i \Gamma_i \left(V_{Ei}\frac{2\pi}{\Phi_0} - \sum_{jk} D_{i,j}B_{j,k}\dot{\varphi}'_k \right)^2 \\ = & \frac{e^2}{4E_C}\left(\frac{\Phi_0}{2\pi}\right)^2 \sum_{ijk} \Gamma_i \left(\left(D_{i,j}B_{j,k}\dot{\varphi}'_k\right)^2 - 2V_{Ei}D_{i,j}B_{j,k}\dot{\varphi}'_k\frac{2\pi}{\Phi_0} \right) + const. \end{aligned} \tag{4.19}$$

Here, we can ignore $\sum_i \Gamma_i \left(V_{Ei}\frac{2\pi}{\Phi_0}\right)^2$ because it is constant.

Furthermore,

$$\sum_{ijkl} A_i\delta_{ij}B_{jk}\dot{\varphi}'_k B_{il}\dot{\varphi}'_l = \sum_{ijkl} \dot{\varphi}'_l B^{\mathrm{T}}_{li}(A_i\delta_{ij})_{ij}B_{jk}\dot{\varphi}'_k, \tag{4.20}$$

and we introduce the following matrices A_{mat} and Γ_{mat}:

$$A_{mat} = \begin{pmatrix} \mathbf{1} & \mathbf{0} & \mathbf{0} & \mathbf{0} \\ \mathbf{0} & \boldsymbol{\alpha} & \mathbf{0} & \mathbf{0} \\ \mathbf{0} & \mathbf{0} & \boldsymbol{\alpha} & \mathbf{0} \\ \mathbf{0} & \mathbf{0} & \mathbf{0} & \mathbf{1} \end{pmatrix}, \Gamma_{mat} = \begin{pmatrix} \mathbf{0} & \mathbf{0} & \mathbf{0} \\ \mathbf{0} & \boldsymbol{\gamma} & \mathbf{0} \\ \mathbf{0} & \mathbf{0} & \mathbf{0} \end{pmatrix}. \tag{4.21}$$

Using above equations, we can rewrite T as follows:

$$\begin{aligned} T = & \frac{e^2}{4E_C}\left(\frac{\Phi_0}{2\pi}\right)^2 \dot{\varphi}'^{\mathrm{T}} B^{\mathrm{T}} A_{mat} B\dot{\varphi}' \\ & + \frac{e^2}{4E_C}\left(\frac{\Phi_0}{2\pi}\right)^2 \left(\dot{\varphi}'^{\mathrm{T}} B^{\mathrm{T}} D^{\mathrm{T}} \Gamma_{mat} DB\dot{\varphi}' - 2V_E\Gamma_{mat}D\dot{\varphi}\frac{\Phi_0}{2\pi} \right) \end{aligned} \tag{4.22}$$

$$\begin{aligned} = & \frac{e^2}{4E_C}\left(\frac{\Phi_0}{2\pi}\right)^2 \dot{\varphi}'^{\mathrm{T}} B^{\mathrm{T}} \left(A_{mat} + D^{\mathrm{T}}\Gamma_{mat}D \right) B\dot{\varphi}' \\ & - \frac{e^2}{2E_C}\frac{\Phi_0}{2\pi}V_E\Gamma_{mat}DB\dot{\varphi}' \end{aligned} \tag{4.23}$$

where V_E denotes

$$V_E = \begin{pmatrix} 0 & V_e & 0 \end{pmatrix}. \tag{4.24}$$

Here, we introduce Lagrangian $\mathcal{L} = T - U$ and generalized momentum $\mathcal{P}_i$

$$\mathcal{P}_i = \frac{\partial \mathcal{L}}{\partial \dot{\varphi}_i'} = \frac{\partial T}{\partial \dot{\varphi}_i'} \tag{4.25}$$

and define the effective mass M as follows:

$$M = \frac{e^2}{2E_C} \left(\frac{\Phi_0}{2\pi} \right)^2 \left(B^{\mathrm{T}} A_{mat} B + B^{\mathrm{T}} D^{\mathrm{T}} \Gamma_{mat} D B \right). \tag{4.26}$$

Then T becomes as follows:

$$T = \sum_{kl} \frac{1}{2} \dot{\varphi}_k' M_{kl} \dot{\varphi}_l' - \frac{e^2}{2E_C} \frac{\Phi_0}{2\pi} \sum_i \left(V_E \Gamma_{mat} D B \right)_i \dot{\varphi}_i', \tag{4.27}$$

and $\mathcal{P}$ becomes as follows:

$$\mathcal{P}_i = \frac{1}{2} \left(\delta_{ik} M_{kl} \dot{\varphi}_l' + \delta_{il} M_{kl} \dot{\varphi}_k' \right) - \frac{e^2}{2E_C} \frac{\Phi_0}{2\pi} \left(V_E \Gamma_{mat} D B \right)_i \tag{4.28}$$

$$\mathcal{P} = M \dot{\varphi}' - \frac{e^2}{2E_C} \frac{\Phi_0}{2\pi} V_E \Gamma_{mat} D B \tag{4.29}$$

For quantization, we replace the generalized momentum $\mathcal{P}_i$ with

$$P_i = -i\hbar \frac{\partial}{\partial \varphi_i'}. \tag{4.30}$$

Then the circuit Hamiltonian becomes as follows:

$$H = \frac{1}{2} \left(P^{\mathrm{T}} + \frac{e^2}{E_C} \frac{\Phi_0}{2\pi} B^{\mathrm{T}} D^{\mathrm{T}} \Gamma_{mat} V_E^{\mathrm{T}} \right) M^{-1} \left(P + \frac{e^2}{E_C} \frac{\Phi_0}{2\pi} V_E \Gamma_{mat} D B \right) + U. \tag{4.31}$$

Here we use

$$M^{\mathrm{T}} = M. \tag{4.32}$$

4.3.2 Simulation

Next, we show how to simulate the Hamiltonian in Eq. (4.31). For this purpose, we rewrite that Hamiltonian using the following functions.

$$H_{sim} \quad = \quad E_J U(N, B, F, A_{mat}) + E_C T(N, M, K) \tag{4.33}$$

where N denotes the size of matrices. We use $2N+1$ x $2N+1$ momentum based matrix to denote each φ. It is because $\varphi(\theta)$ can be rewrite as follows:

$$\varphi(\theta) = \sum_{k=-N}^{N} p_k e^{ik\theta}, \tag{4.34}$$

where p denotes momentum term. Larger N give higher accuracy and long simulation time. We set $N = 6$ in every simulation.

Table 4.1: Functions used in simulations. These functions are the standard in Matlab and Octave.

Functions	Descriptions	Examples
$zeros(n)$	A square matrix of dimension n where every component is zero.	$zeros(3) = \begin{pmatrix} 0 & 0 & 0 \\ 0 & 0 & 0 \\ 0 & 0 & 0 \end{pmatrix}$
$eye(n)$	An identity square matrix of dimension (n).	$eye(2) = \begin{pmatrix} 1 & 0 \\ 0 & 1 \end{pmatrix}$
$ones(n, m)$	Returns the n by m matrix where every component is one.	$ones(2, 3) = \begin{pmatrix} 1 & 1 & 1 \\ 1 & 1 & 1 \end{pmatrix}$

$diag(P, q)$ p:The elements number of P.	Returns a square matrix of dimension $p + q$ with elements of P on qth diagonal. When $q > 0$ ($q < 0$), qth diagonal is located in the upper (lowner) part of the matrix. 0th diagonal means the main diagonal.	$P = \begin{pmatrix} 1 & 2 \end{pmatrix}$ $diag(P, 1) = \begin{pmatrix} 0 & 1 & 0 \\ 0 & 0 & 2 \\ 0 & 0 & 0 \end{pmatrix}$ $diag(P, -2) = \begin{pmatrix} 0 & 0 & 0 & 0 \\ 0 & 0 & 0 & 0 \\ 1 & 0 & 0 & 0 \\ 0 & 2 & 0 & 0 \end{pmatrix}$

Here, we define L_V is the number of components in the vector (or line of matrix) V. We show details of function $U(N, B, F, A_{mat})$ as follows:

function $U($ int N, matrix B, vector F, matrix $A_{mat})$

Input: The size of matrices N, phase constraints B and F in Eq. (4.9), and the area ratio of Junctions A_{mat} in Eq. (4.21).

Output: $2N + 1$ x $2N + 1$ matrix of potential energy U.

$U = zeros((2N + 1)^{L_B})$.
for $k = 1 : L_U$ **do**
  for $l = 1 : L_B$ **do**
    $s(l) = diag(ones(1, 2N + 1 - |B(k, l)|), +B(k, l))$
    $t(l) = diag(ones(1, 2N + 1 - |B(k, l)|), -B(k, l))$
  end for
  $S = s(1) \otimes s(2) \otimes .. \otimes s(L_B)$.
  $T = t(1) \otimes t(2) \otimes .. \otimes t(L_B)$.
  $COS(N, B(k, :), F(k)) = (Se^{F(k)i} + Te^{-F(k)i})/2$
  $U = U + A_{mat}(k, k)(eye((2N + 1)^{L_B}) - COS(N, B(k, :), F(k)))$
end for
return U
end function

Next, we define K is

$$K = -V\Gamma_{mat}DB. \tag{4.35}$$

We show details of the function $T(N, M, K)$ as follows:

function T(int N, matrix M, vector K)

Input: The size of matrices N, the effective mass M in Eq. (4.26), and effects of external voltage K in Eq. (4.35).

Output: $2N + 1$ x $2N + 1$ matrix of momentum energy T.

$T = 0$

$M_{inv} = M^{-1} \otimes eye((2N + 1)^{L_M})$

for $l = 1 : L_K$ **do**

for $k = 1 : L_K$ **do**

$t(k) = eye(2N + 1)$

end for

$t(l) = diag((-N : N) + K(l), 0)$

$P_{mat} = t(1) \otimes t(2) \otimes .. \otimes t(L_k)$.

end for

$T = 4P_{mat}^T M_{inv} P_{mat}$

return T

end function

By diagonalization of H_{sim}, we can determine eigenvectors and eigenvalues of this circuit.

Although the system Hamiltonian H has many energy levels, the system can be described as a two-level system (qubit) due to a strong unharmonicity by choosing suitable α. We show the α dependence of the energy of this system Fig. 4.2, where E_{01} (E_{12}) denotes the energy splitting between the ground (first excited) and the first excited (second excited) state. This clearly shows that system has an unharmonicity so that we can control only the ground state and first excited state by using frequency selectivity.

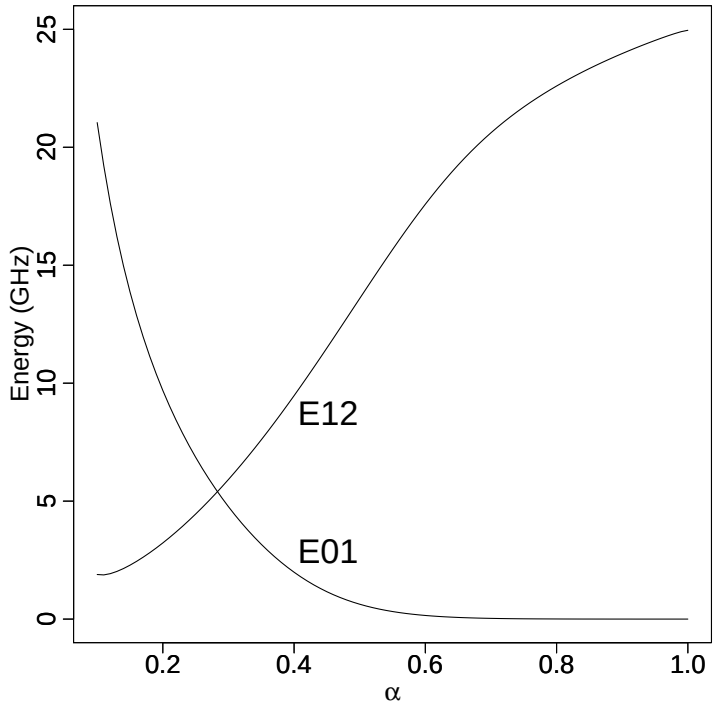

Figure 4.2: The α dependence of E_{01} and E_{12} where E_{01} denotes energy difference between the ground state and the first excited state, E_{12} denotes energy difference between the first excited state and the second excited state. Here, we set $E_{J(1)} = E_{J(4)} = 200$ GHz, $E_{J(2)} = E_{J(3)} = 40$ GHz, and $E_{J(k)}/E_{C(k)} = 80(k = 1, 2, .., 4)$.

$|g\rangle$ and $|e\rangle$ are the ground and the first excited state of the system Hamiltonian H for $f = 0.5$. In this regime, the ground state and the first excited state of this system contains a superposition of clockwise and anticlockwise persistent currents. Here, $|L\rangle = \frac{1}{\sqrt{2}}(|g\rangle + |e\rangle)$ corresponds anticlockwise persistent current and $|R\rangle = \frac{1}{\sqrt{2}}(|e\rangle - |g\rangle)$ corresponds clockwise one.

While f is around 0.5, due to the unharmonicity, we can consider only the ground state and first excited state in the Hamiltonian H, and so we can simplify the H into $\hat{H}_{ge}$ spanned by $|g\rangle$ and $|e\rangle$ as follows:

$$\hat{H}_{ge} = \frac{1}{2}(\Delta\sigma_Z + \varepsilon\sigma_Y) \tag{4.36}$$

where $\sigma_Z = |e\rangle\langle e| - |g\rangle\langle g|$ and $\sigma_Y = -i|e\rangle\langle g| + i|g\rangle\langle e|$ are Pauli matrices, Δ denotes the tunneling energy between $|L\rangle$ and $|R\rangle$, ε denotes the energy bias

between $|L\rangle$ and $|R\rangle$. The energy of the qubit is described as $E_{01} = \sqrt{\varepsilon^2 + \Delta^2}$.

In this chapter, unless indicated otherwise, we fix parameters as $\alpha = 0.2$ and $E_{J(1)} = 200$ GHz and $E_{J(k)}/E_{C(k)}$ ratio is 80. Here, $E_{C(k)} = e^2/2C_{J(k)}$ is charge energy of each Josephson junction. In this parameter regime, E_{01} is about three times larger than E_{12} as shown in Fig. 4.2 so that we could consider this system as an effective two-level system. When f is set to be near 0.5, the derivative of the qubit energy against the magnetic flux $|\frac{dE_{01}}{df}|$ takes the minimum value, so that the qubit should be well decoupled from flux noise, and we achieve the maximum coherent times. We call this regime "optimal point". On the other hand, we can control the value of ε by changing the value of f. When the energy bias ε is much larger than the tunneling energy Δ, the persistent current states are the eigenvectors of the Hamiltonian so that we can read out the qubit state with SQUID[25] in $\{|L\rangle, |R\rangle\}$ base. Here we show the dependence of ε and Δ against magnetic field with no bias voltage applied in Fig. 4.3. It is worth mentioning

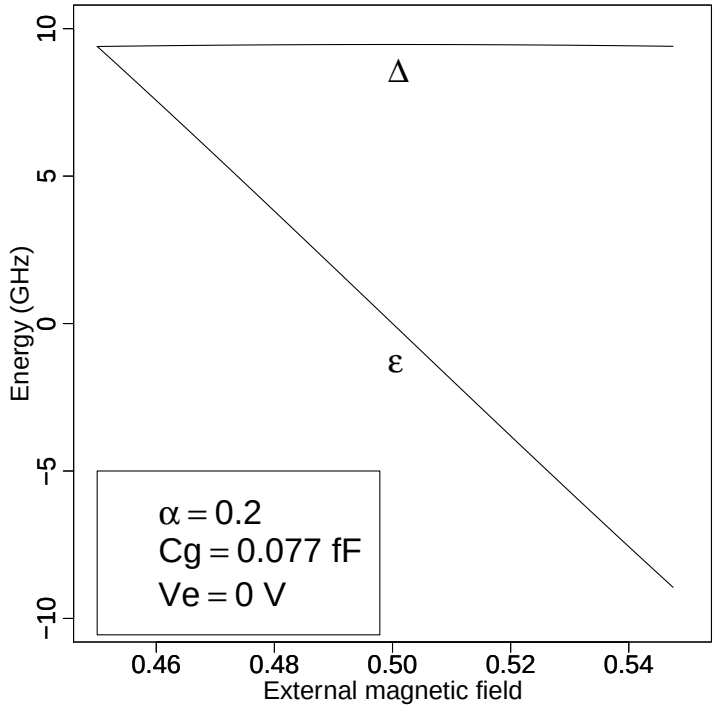

Figure 4.3: The tunneling energy Δ and the energy bias ε against the magnetic flux f. ε decreases monotonically as we increase f, while Δ is almost independent of f.

that we can control the energy of the qubit by tuning the applied voltage V_e while operating at the optimal point. We show the relationship between Δ and f with several values of V_e in Fig. 4.4. In addition, we show the relationship between Δ

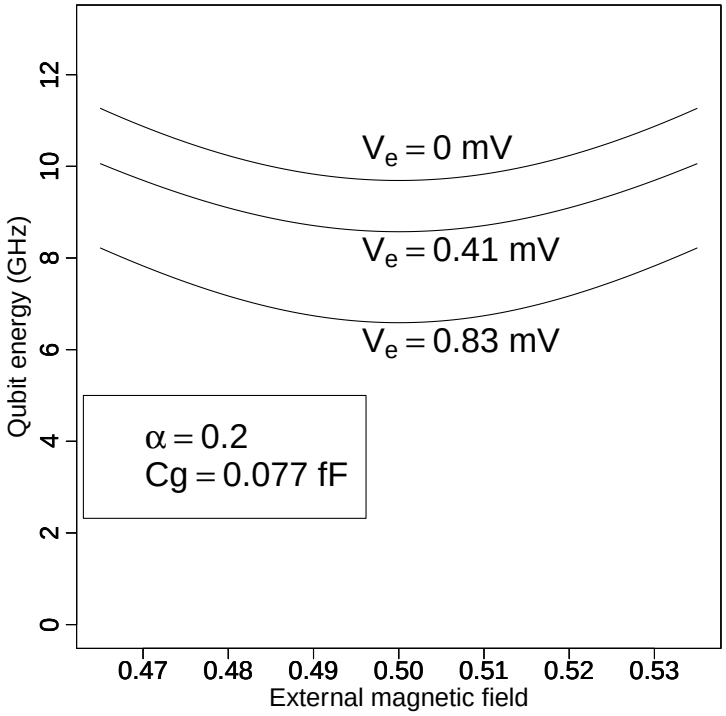

Figure 4.4: The relationship between the external magnetic flux f and the energy of the qubit $E_{01}(= \Delta + \varepsilon)$ with different voltage levels. Here, we set the $\alpha = 0.2$ and the gate capacitance $Cg = 0.077$ fF.

and f with several values of α in Fig. 4.5.

4.4 Ising type interaction using capacitive coupling

4.4.1 Generating interaction between two-qubit system

In this section, we show how to generate an Ising type interaction using charge coupling for superconducting flux qubits. As a novel feature of our scheme, we use only external voltages to switch on and off the interaction between two flux qubits. Unlike previous schemes, an external magnetic field is not required to control the interaction in our scheme. Since the voltage can be applied locally compared with the case of applying magnetic field, we may have an advantage in

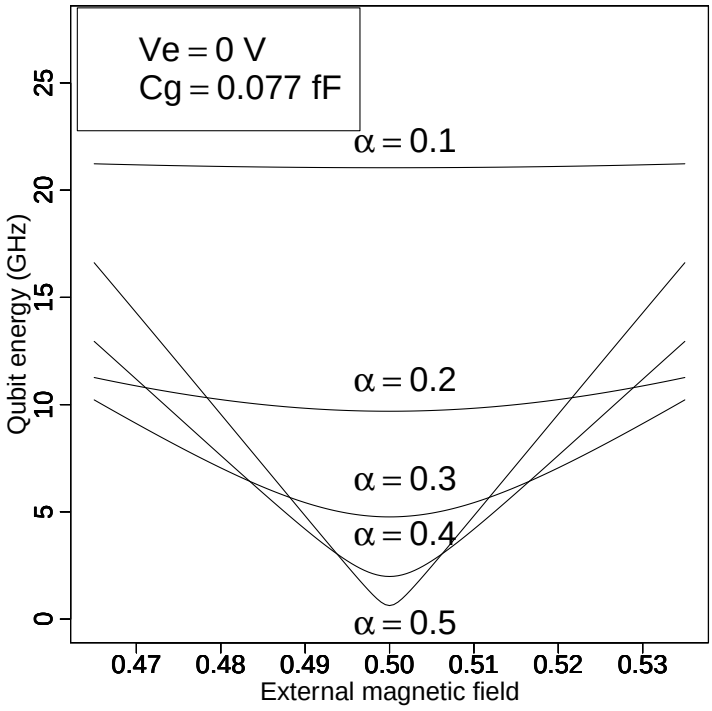

Figure 4.5: The relationship between f and $E_{01}(= \Delta + \varepsilon)$ with different α.

this scheme for scalability due to possibly smaller cross-talk problems when we try to control individual qubits.

Here, we show the circuit for our scheme using two superconducting flux qubits in Fig. 4.6. The structure of each qubit is the same as that shown in Fig. 4.1. When we apply an external voltage $V_e^{(l)}$ on each qubit, the qubit interact with each other across the capacitor $C_c^{(1,2)}$. We describe the details of this circuit in the following subsections.

4.4.2 Hamiltonian

Josephson phases $\varphi_n^{(k)}$ are subject to the following equation:

$$\varphi_1^{(k)} + \varphi_2^{(k)} + \varphi_3^{(k)} + \varphi_4^{(k)} = -2\pi f^{(k)} \tag{4.37}$$

where $\varphi_n^{(k)}$ and $f^{(k)}$ denote the phase of each Josephson junction JJn and external magnetic flux of qubit k.

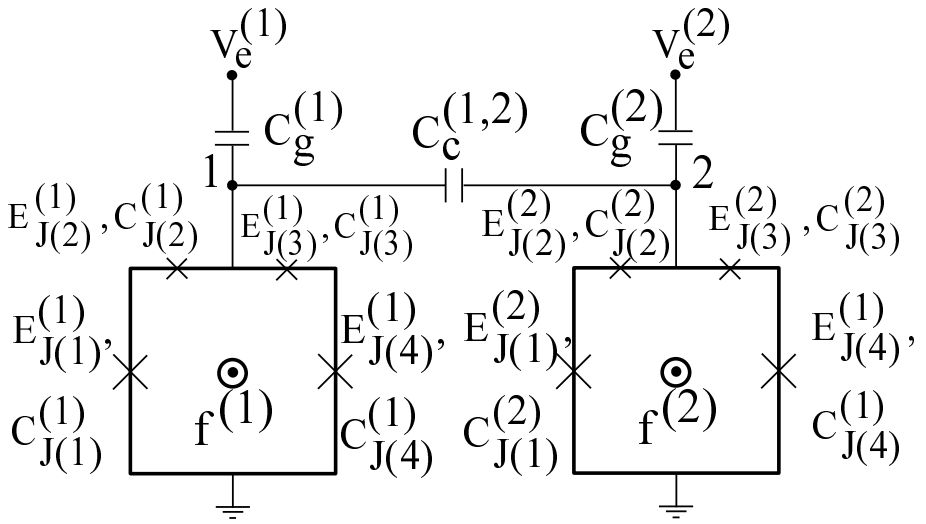

Figure 4.6: Two flux qubits 1, 2 are coupled via capacitance $Cc^{(1,2)}$. Each flux qubit is threaded by an external magnetic flux $f^{(l)}$, and we can control the energy bias of the qubit via the magnetic flux. Node 1 and node 2 represent the superconducting islands. JJ2 and JJ3 at each qubit have the same Josephson energies and capacitances that are α times larger than those of all remaining Josephson junctions. The electric potential of the island include node 1 (2) is $V_i^{(1)}$ ($V_i^{(2)}$). $Cc^{(1,2)}$, $C_{J(n)}^{(l)}$, and $Cg^{(l)}$ denote coupling capacitance between two qubits, capacitance of the n th Josephson junction JJn of qubit l, and gate capacitance between external voltage and node, respectively.

We now consider the total potential energy U and the total electric energy T of the circuit in Fig. 4.6 as follows:

$$U = \sum_{l=1}^{2}\sum_{k=1}^{4} E_{J(k)}^{(l)}\left(1-\cos\varphi_k^{(l)}\right), \tag{4.38}$$

$$T = \frac{1}{2}\sum_{l=1}^{2}\sum_{k=1}^{4} C_{J(k)}^{(l)}\left(\frac{\Phi_0}{2\pi}\dot{\varphi}_k^{(l)}\right)^2 + \frac{1}{2}\sum_{l=1}^{2} C_g^{(l)}\left(V_e^{(l)}-V_I^{(l)}\right)^2 + \frac{1}{2}C_c^{(1,2)}\left(V_I^{(1)}-V_I^{(2)}\right)^2 \tag{4.39}$$

where $E_{J(n)}^{(l)}$ and $C_{J(n)}^{(l)}$ denote the Josephson energy and capacitance of the n th Josephson junction JJn and $C_g^{(l)}$, $V_e^{(l)}$, and $V_I^{(l)}$ denote gate capacitance, applied external voltage, and the electric potential of the island including node l for the l th qubit respectively. Here, node l represents the superconducting islands. The

last term of Eq. (4.39) denotes the energy of capacitive coupling between two qubits.

From the phase constraints in Eq. (4.37), each phase φ_k and the time derivative of phase $\dot{\varphi}_k$ can be described using φ' and $\dot{\varphi}'$ as follows:

$$\varphi = \begin{pmatrix} \boldsymbol{\varphi_1^{(1)}} \\ \boldsymbol{\varphi_2^{(1)}} \\ \boldsymbol{\varphi_3^{(1)}} \\ \boldsymbol{\varphi_4^{(1)}} \\ \boldsymbol{\varphi_1^{(2)}} \\ \boldsymbol{\varphi_2^{(2)}} \\ \boldsymbol{\varphi_3^{(2)}} \\ \boldsymbol{\varphi_4^{(2)}} \end{pmatrix}, \ \varphi_k = \sum_j B_{kj}\varphi'_j + F_k, \varphi' = \begin{pmatrix} \boldsymbol{\varphi'_1} \\ \boldsymbol{\varphi'_2} \\ \boldsymbol{\varphi'_3} \\ \boldsymbol{\varphi'_4} \\ \boldsymbol{\varphi'_5} \\ \boldsymbol{\varphi'_6} \end{pmatrix}, \tag{4.40}$$

$$\dot{\varphi} = \begin{pmatrix} \boldsymbol{\dot{\varphi}_1^{(1)}} \\ \boldsymbol{\dot{\varphi}_2^{(1)}} \\ \boldsymbol{\dot{\varphi}_3^{(1)}} \\ \boldsymbol{\dot{\varphi}_4^{(1)}} \\ \boldsymbol{\dot{\varphi}_1^{(2)}} \\ \boldsymbol{\dot{\varphi}_2^{(2)}} \\ \boldsymbol{\dot{\varphi}_3^{(2)}} \\ \boldsymbol{\dot{\varphi}_4^{(2)}} \end{pmatrix}, \ \dot{\varphi}_k = \sum_j B_{kj}\dot{\varphi}'_j, \dot{\varphi}' = \begin{pmatrix} \boldsymbol{\dot{\varphi}'_1} \\ \boldsymbol{\dot{\varphi}'_2} \\ \boldsymbol{\dot{\varphi}'_3} \\ \boldsymbol{\dot{\varphi}'_4} \\ \boldsymbol{\dot{\varphi}'_5} \\ \boldsymbol{\dot{\varphi}'_6} \end{pmatrix}, \tag{4.41}$$

Here, we introduce following B and F

$$B = \begin{pmatrix} \mathbf{1} & \mathbf{0} & \mathbf{0} & \mathbf{0} & \mathbf{0} & \mathbf{0} \\ \mathbf{0} & \mathbf{1} & \mathbf{0} & \mathbf{0} & \mathbf{0} & \mathbf{0} \\ \mathbf{0} & \mathbf{0} & \mathbf{1} & \mathbf{0} & \mathbf{0} & \mathbf{0} \\ \mathbf{-1} & \mathbf{-1} & \mathbf{-1} & \mathbf{0} & \mathbf{0} & \mathbf{0} \\ \mathbf{0} & \mathbf{0} & \mathbf{0} & \mathbf{1} & \mathbf{0} & \mathbf{0} \\ \mathbf{0} & \mathbf{0} & \mathbf{0} & \mathbf{0} & \mathbf{1} & \mathbf{0} \\ \mathbf{0} & \mathbf{0} & \mathbf{0} & \mathbf{0} & \mathbf{0} & \mathbf{1} \\ \mathbf{0} & \mathbf{0} & \mathbf{0} & \mathbf{-1} & \mathbf{-1} & \mathbf{-1} \end{pmatrix}, F = \begin{pmatrix} \mathbf{0} \\ \mathbf{0} \\ \mathbf{0} \\ \mathbf{-2\pi f^{(1)}} \\ \mathbf{0} \\ \mathbf{0} \\ \mathbf{0} \\ \mathbf{-2\pi f^{(2)}} \end{pmatrix}. \tag{4.42}$$

Then, we can rewrite the total Josephson energy U as follows:

$$\begin{aligned} U &= E_J \sum_k A_k (1 - \cos \varphi_k) && (4.43) \\ &= E_J \sum_k A_k (1 - \cos(\sum_j B_{kj} \varphi'_j + F_k)). && (4.44) \end{aligned}$$

Here, we introduce the area ratio $A_n^{(l)}$ of each JJn of qubit l as follows:

$$A_1^{(l)} = A_4^{(l)} = 1,\ A_2^{(l)} = A_3^{(l)} = \alpha,\ \text{where } l \in \{1, 2\}. \tag{4.45}$$

Then, the capacitance and the critical current of each Josephson junction are proportional to $A_j^{(l)}$.

We define $V_j,\ j \in \{1, 2, 3\}$ as the voltage difference between the ground voltage and the voltage between two Josephson junctions JJ_j and JJ_{j+1} of qubit 1. We also define $V_j,\ j \in \{4, 5, 6\}$ as the voltage difference between the ground voltage and the voltage between JJ_{j-3} and JJ_{j-2} of qubit 2. Then, the electric potential $V_I^{(k)}$ becomes

$$V_I^{(1)} = V_2 = \frac{\Phi_0}{2\pi}(\dot{\varphi}_1 + \dot{\varphi}_2), \tag{4.46}$$

$$V_I^{(2)} = V_5 = \frac{\Phi_0}{2\pi}(\dot{\varphi}_4 + \dot{\varphi}_5), \tag{4.47}$$

Furthermore, each V_j can be described using matrix D as follows:

$$V = \begin{pmatrix} \boldsymbol{V_1} \\ \boldsymbol{V_2} \\ \boldsymbol{V_3} \\ \boldsymbol{V_4} \\ \boldsymbol{V_5} \\ \boldsymbol{V_6} \end{pmatrix}, \; V_j = \sum_i D_{ji} \left(\frac{\Phi_0}{2\pi} \right) \dot{\varphi}_i, \; D = \begin{pmatrix} \mathbf{1} & \mathbf{0} & \mathbf{0} & \mathbf{0} & \mathbf{0} & \mathbf{0} & \mathbf{0} & \mathbf{0} \\ \mathbf{1} & \mathbf{1} & \mathbf{0} & \mathbf{0} & \mathbf{0} & \mathbf{0} & \mathbf{0} & \mathbf{0} \\ \mathbf{1} & \mathbf{1} & \mathbf{1} & \mathbf{0} & \mathbf{0} & \mathbf{0} & \mathbf{0} & \mathbf{0} \\ \mathbf{0} & \mathbf{0} & \mathbf{0} & \mathbf{0} & \mathbf{1} & \mathbf{0} & \mathbf{0} & \mathbf{0} \\ \mathbf{0} & \mathbf{0} & \mathbf{0} & \mathbf{0} & \mathbf{1} & \mathbf{1} & \mathbf{0} & \mathbf{0} \\ \mathbf{0} & \mathbf{0} & \mathbf{0} & \mathbf{0} & \mathbf{1} & \mathbf{1} & \mathbf{1} & \mathbf{0} \end{pmatrix}. \quad (4.48)$$

From the formula (4.39), the total electric energy T becomes as follows:

$$\begin{aligned} T \; =& \sum_k \frac{A_k e^2}{4E_C} \left(\frac{\Phi_0}{2\pi} \dot{\varphi}_k \right)^2 + \sum_i \frac{1}{2} C_{gi} \left(V_{Ei} - V_i \right)^2 + \sum_{ij} \frac{1}{2} C_{cij} \left(V_i - V_j \right)^2 \quad (4.49) \\ =& \sum_k \frac{e^2}{4E_C} \left(\frac{\Phi_0}{2\pi} \right)^2 A_k \left(\sum_i B_{ki} \dot{\varphi}'_i \right)^2 + \frac{1}{2} C_g \left(V_{Ei} - \sum_{jk} D_{i,j} B_{j,k} \dot{\varphi}'_j \frac{\Phi_0}{2\pi} \right)^2 \\ & + \frac{1}{2} \sum_{ij} \left(V_i^2 + V_j^2 - 2 V_i V_j \right) C_{cij} \quad (4.50) \end{aligned}$$

where C_{gi} denotes the capacitance of the gate capacitor which is connected to the island between two junctions. When $i = 1, 2, 3$, two junctions denote JJ_i and JJ_{i+1} of qubit 1. When $i = 4, 5, 6$, two junctions denote JJ_{j-3} and JJ_{j-2} of qubit 2. V_{Ei} denotes the external voltage to the island which is determined from above rules. C_{cij} denotes the capacitance between two island which are also determined from above rules. In this case, C_{g2}, C_{g5}, V_{E2}, V_{E5}, and C_{c25} are $C_g^{(1)}$, $C_g^{(2)}$, $V_e^{(1)}$, $V_e^{(2)}$ and $C_c^{(1,2)}$in Fig. 4.6. Here, we introduce the ratio of capacitance C_{gi} as follows:

$$\Gamma_1 = \Gamma_3 = \Gamma_4 = \Gamma_6 = 0, \; \Gamma_2 = \Gamma_5 = \gamma. \quad (4.51)$$

Γ_i satisfies the following conditions:

$$C_{gi} \;\; = \;\; C_{J(1)} \Gamma_i = \frac{e^2}{2E_C} \Gamma_i. \quad (4.52)$$

Then, as in the case of one qubit system, the second term of formula (4.50) becomes

$$\begin{aligned} & \frac{e^2}{4E_C}\left(\frac{\Phi_0}{2\pi}\right)^2 \sum_i \Gamma_i \left(V_{Ei}\frac{2\pi}{\Phi_0} - \sum_{jk} D_{i,j}B_{j,k}\dot{\varphi}'_k \right)^2 \\ = & \frac{e^2}{4E_C}\left(\frac{\Phi_0}{2\pi}\right)^2 \sum_{ijk} \Gamma_i \left(\left(D_{i,j}B_{j,k}\dot{\varphi}'_k\right)^2 - 2V_{Ei}D_{i,j}B_{j,k}\dot{\varphi}'_k\frac{2\pi}{\Phi_0} \right) + const. \end{aligned} \tag{4.53}$$

Here, we can ignore $\sum_i \Gamma_i \left(V_{Ei}\frac{2\pi}{\Phi_0}\right)^2$ because it is constant term.
Furthermore, the last term of formula (4.50) becomes

$$\sum_k V_k^2 \sum_l C_{c(k,l)} - \sum_{ij} V_i C_{c(i,j)} V_j = \frac{e^2}{2E_C} V^{\mathrm{T}} C'_c V \tag{4.54}$$

$$= \frac{e^2}{2E_C}\left(\frac{\Phi_0}{2\pi}\right)^2 \dot{\varphi}'^{\mathrm{T}} B^{\mathrm{T}} D^{\mathrm{T}} C'_c D B \dot{\varphi}' \tag{4.55}$$

where

$$\frac{e^2}{2E_C} C'_{c(i,j)} \equiv -C_{c(i,j)} + \delta_{i,j} \sum_k C_{c(i,k)}. \tag{4.56}$$

Next, we introduce following matrices A^{2q}_{mat} and Γ^{2q}_{mat}:

$$A^{2q}_{mat} = \begin{pmatrix} \mathbf{1} & \mathbf{0} & \mathbf{0} & \mathbf{0} & \mathbf{0} & \mathbf{0} & \mathbf{0} & \mathbf{0} \\ \mathbf{0} & \boldsymbol{\alpha} & \mathbf{0} & \mathbf{0} & \mathbf{0} & \mathbf{0} & \mathbf{0} & \mathbf{0} \\ \mathbf{0} & \mathbf{0} & \boldsymbol{\alpha} & \mathbf{0} & \mathbf{0} & \mathbf{0} & \mathbf{0} & \mathbf{0} \\ \mathbf{0} & \mathbf{0} & \mathbf{0} & \mathbf{1} & \mathbf{0} & \mathbf{0} & \mathbf{0} & \mathbf{0} \\ \mathbf{0} & \mathbf{0} & \mathbf{0} & \mathbf{0} & \mathbf{1} & \mathbf{0} & \mathbf{0} & \mathbf{0} \\ \mathbf{0} & \mathbf{0} & \mathbf{0} & \mathbf{0} & \mathbf{0} & \boldsymbol{\alpha} & \mathbf{0} & \mathbf{0} \\ \mathbf{0} & \mathbf{0} & \mathbf{0} & \mathbf{0} & \mathbf{0} & \mathbf{0} & \boldsymbol{\alpha} & \mathbf{0} \\ \mathbf{0} & \mathbf{0} & \mathbf{0} & \mathbf{0} & \mathbf{0} & \mathbf{0} & \mathbf{0} & \mathbf{1} \end{pmatrix}, \Gamma^{2q}_{mat} = \begin{pmatrix} \mathbf{0} & \mathbf{0} & \mathbf{0} & \mathbf{0} & \mathbf{0} & \mathbf{0} \\ \mathbf{0} & \boldsymbol{\gamma} & \mathbf{0} & \mathbf{0} & \mathbf{0} & \mathbf{0} \\ \mathbf{0} & \mathbf{0} & \mathbf{0} & \mathbf{0} & \mathbf{0} & \mathbf{0} \\ \mathbf{0} & \mathbf{0} & \mathbf{0} & \mathbf{0} & \mathbf{0} & \mathbf{0} \\ \mathbf{0} & \mathbf{0} & \mathbf{0} & \mathbf{0} & \boldsymbol{\gamma} & \mathbf{0} \\ \mathbf{0} & \mathbf{0} & \mathbf{0} & \mathbf{0} & \mathbf{0} & \mathbf{0} \end{pmatrix}. \tag{4.57}$$

Using above equations, we can rewrite T as follows:

$$\begin{aligned} T &= \frac{e^2}{4E_C}\left(\frac{\Phi_0}{2\pi}\right)^2 \dot{\varphi}'^{\mathrm{T}} B^{\mathrm{T}} A_{mat}^{2q} B\dot{\varphi}' \\ &\quad + \frac{e^2}{4E_C}\left(\frac{\Phi_0}{2\pi}\right)^2 \left(\dot{\varphi}'^{\mathrm{T}} B^{\mathrm{T}} D^{\mathrm{T}} \Gamma_{mat}^{2q} DB\dot{\varphi}' - 2V_E \Gamma_{mat}^{2q} D\dot{\varphi}\frac{\Phi_0}{2\pi}\right) \\ &\quad + \left(\frac{\Phi_0}{2\pi}\right)^2 \dot{\varphi}'^{\mathrm{T}} B^{\mathrm{T}} D^{\mathrm{T}} C_c' DB\dot{\varphi}' \qquad (4.58) \\ &= \frac{e^2}{4E_C}\left(\frac{\Phi_0}{2\pi}\right)^2 \dot{\varphi}'^{\mathrm{T}} B^{\mathrm{T}} \left(A_{mat}^{2q} + D^{\mathrm{T}}\Gamma_{mat}^{2q} D + 2D^{\mathrm{T}} C_c' D\right) B\dot{\varphi}' \\ &\quad - \frac{e^2}{2E_C}\frac{\Phi_0}{2\pi} V_E \Gamma_{mat}^{2q} DB\dot{\varphi}' \qquad (4.59) \end{aligned}$$

where V_E denotes

$$V_E = \begin{pmatrix} 0 & V_e^{(1)} & 0 & 0 & V_e^{(2)} & 0 \end{pmatrix}. \qquad (4.60)$$

Here, we introduce Lagrangian $\mathcal{L} = T - U$ and generalized momentum $\mathcal{P}_i$

$$\mathcal{P}_i = \frac{\partial \mathcal{L}}{\partial \dot{\varphi}_i'} = \frac{\partial T}{\partial \dot{\varphi}_i'} \qquad (4.61)$$

and define the effective mass M as follows:

$$M = \frac{e^2}{2E_C}\left(\frac{\Phi_0}{2\pi}\right)^2 \left(B^{\mathrm{T}} A_{mat}^{2q} B + B^{\mathrm{T}} D^{\mathrm{T}} \left(\Gamma_{mat}^{2q} + 2C_c'\right) DB\right). \qquad (4.62)$$

Then, T and $\mathcal{P}$ become as follows:

$$\begin{aligned} T &= \sum_{kl} \frac{1}{2}\dot{\varphi}_k' M_{kl} \dot{\varphi}_l' - \frac{e^2}{2E_C}\frac{\Phi_0}{2\pi}\sum_i \left(V_E \Gamma_{mat}^{2q} DB\right)_i \dot{\varphi}_i', \qquad (4.63) \\ \mathcal{P} &= M\dot{\varphi}' - \frac{e^2}{2E_C}\frac{\Phi_0}{2\pi} V_E \Gamma_{mat}^{2q} DB \qquad (4.64) \end{aligned}$$

For quantization, we replace the generalized momentum $\mathcal{P}_i$ with

$$P_i = -i\hbar\frac{\partial}{\partial \varphi_i'}. \qquad (4.65)$$

Then, the circuit Hamiltonian becomes as follows:

$$H = \frac{1}{2}\left(P^{\mathrm{T}} + \frac{e^2}{E_C}\frac{\Phi_0}{2\pi}B^{\mathrm{T}}D^{\mathrm{T}}\Gamma_{mat}^{2q}V_E^{\mathrm{T}}\right)M^{-1}\left(P + \frac{e^2}{E_C}\frac{\Phi_0}{2\pi}V_E\Gamma_{mat}^{2q}DB\right) + U. \quad (4.66)$$

4.4.3 Simulation

The size of Hamiltonian in Eq. (4.66) is too large to diagonalize with high accuracy. We can derive the effective four-level ($|gg\rangle_{12}$, $|ge\rangle_{12}$, $|eg\rangle_{12}$, and $|ee\rangle_{12}$) Hamiltonian $\hat{H}_{ge}$ of the eigenspace spanned by $|g^{(k)}\rangle$ and $|e^{(k)}\rangle$ using the following steps. Here, $|g^{(k)}\rangle$ and $|e^{(k)}\rangle$ denote the ground state and first excited state of the k^{th} qubit without interactions for $f^{(1)} = f^{(2)} = 0.5$.

Step 1 We construct the local Hamiltonian of each qubit $H_{local}^{(k)}$ without considering capacitive coupling. $H_{local}^{(k)}$ and the one qubit Hamiltonian in Eq. 4.31 are the same except for the parameters F and V_E.

Step 2 We set $f^{(k)} = 0.5$ to calculate the ground state $|g^{(k)}\rangle$ and the first excited state $|e^{(k)}\rangle$ from $H_{local}^{(k)}$ using the scheme in 4.3.2.

Step3 We set $C_c^{(1,2)}$ and calculate the inverse of the effective mass M^{-1} in Eq. (4.62).

Step4 We simulate the following functions to obtain $\hat{H}_{ge}$:

$$\hat{H}_{ge} = \sum_{v_L^{(1)},v_R^{(1)},v_L^{(2)},v_R^{(2)}} |v_L^{(1)}v_L^{(2)}\rangle\langle v_L^{(1)}v_L^{(2)}|H|v_R^{(1)}v_R^{(2)}\rangle\langle v_R^{(1)}v_R^{(2)}| \quad (4.67)$$

$$\begin{aligned}\langle v_L^{(1)}v_L^{(2)}|H|v_R^{(1)}v_R^{(2)}\rangle &= E_J U(v_L^{(1)}, v_R^{(1)}, v_L^{(2)}, v_R^{(2)}, U^{(1)}, U^{(2)}) \\ &\quad + E_C T(v_L^{(1)}, v_R^{(1)}, v_L^{(2)}, v_R^{(2)}, N, M^{-1}, K) \quad (4.68)\end{aligned}$$

where N denotes the size of matrices, $v_L^{(k)}$ and $v_R^{(k)}$ satisfy the following conditions,

$$v_L^{(1)}, v_R^{(1)} \in \{g^{(1)}, e^{(1)}\}, \qquad v_L^{(2)}, v_R^{(2)} \in \{g^{(2)}, e^{(2)}\}. \quad (4.69)$$

$U^{(1)}, U^{(2)}$ denote

$$U^{(1)} = E_J \sum_{k=1}^{4} A_k (1 - \cos(\sum_j B_{kj}\varphi'_j + F_k)) \tag{4.70}$$

$$U^{(2)} = E_J \sum_{k=5}^{8} A_k (1 - \cos(\sum_j B_{kj}\varphi'_j + F_k)), \tag{4.71}$$

and K denotes

$$K = \frac{e^2}{E_C}\frac{\Phi_0}{2\pi} V_E \Gamma_{mat} DB. \tag{4.72}$$

Here, the function $U(v_L^{(1)}, v_R^{(1)}, v_L^{(2)}, v_R^{(2)}, U^{(1)}, U^{(2)})$ denotes

$$\begin{aligned} & U(v_L^{(1)}, v_R^{(1)}, v_L^{(2)}, v_R^{(2)}, U^{(1)}, U^{(2)}) \\ = \; & \langle v_L^{(1)}|U^{(1)}|v_R^{(1)}\rangle\langle v_L^{(2)}|v_R^{(2)}\rangle + \langle v_L^{(1)}|v_R^{(1)}\rangle\langle v_L^{(2)}|U^{(2)}|v_R^{(2)}\rangle. \end{aligned} \tag{4.73}$$

Next, we show details of the function $T(v_L^{(1)}, v_R^{(1)}, v_L^{(2)}, v_R^{(2)}, N, M^{-1}, K)$ as follows:

function T(vector $v_L^{(1)}$, vector $v_R^{(1)}$,vector $v_L^{(2)}$, vector $v_R^{(2)}$, int N, matrix M^{-1}, vector K)

Input: Set vectors $v_L^{(i)}$ and $v_R^{(i)}$in Eq. (4.68), the size of matrices N, the inverse of the effective mass M^{-1} in Eq. (4.62), and effects of external voltage K in Eq. (4.72).

Output: $2N + 1$ x $2N + 1$ matrix of momentum energy T.

$q = 2$ **: number of qubits**

$w = length(K);$ **: number of wave functions**

for $k = 0 : w - 1$ **do**

$PMatrix_{(k)} = diag((-N : N) + K(k), 0)$

end for

for $k = 0 : \frac{w}{q} - 1$ **do**

$IMatrix_{(k)} = identity(2 * N + 1)$ **: matrix for initialization**

end for

for $a = 0 : w - 1$ **do**

for $b = 0 : w - 1$ **do**

$P_0 = P_1 = \{IMatrix\}$ **: initialize**

$Phi_{(0)} = Phi_{(1)} = identity((2 * N + 1)^3)$ **: initialize**

$P_{0(a\%3)} = PMatrix_{(a)}$

$P_{1(b\%3)} = PMatrix_{(b)}$

$\Phi_{(a/3)*} = P_{0(0)} \otimes P_{0(1)} \otimes P_{0(2)}$

$\Phi_{(b/3)*} = P_{1(0)} \otimes P_{1(1)} \otimes P_{1(2)}$

$T = T + M^{-1}_{(a,b)} \langle v^{(1)}_L | \Phi_{(0)} | v^{(1)}_R \rangle \langle v^{(2)}_L | \Phi_{(1)} | v^{(2)}_R \rangle$

end for

end for

return T

end function

For an arbitrary $f^{(l)}$, the effective Hamiltonian $\hat{H}_{ge}$ becomes as follows:

$$\begin{aligned} \hat{H}_{ge} &= \sum_{l=1}^{2} \frac{1}{2} \left(\Delta^{(l)} \sigma_Z^{(l)} + \varepsilon^{(l)} \sigma_Y^{(l)} \right) + g \sigma_Z^{(1)} \sigma_Z^{(2)} \\ &\quad + g' \sigma_Y^{(1)} \sigma_Z^{(2)} + g'' \sigma_Z^{(1)} \sigma_Y^{(2)} + g''' \sigma_Y^{(1)} \sigma_Y^{(2)} \end{aligned} \tag{4.74}$$

where g denotes the Ising type interaction strength between qubit 1 and 2. g', g'', and g''' are suppressed to zero as long as $f^{(1)} = f^{(2)} = 0.5$. In this chapter, we use this regime. We show the change of the qubit energy E_{01} in Fig. 4.7 and the interaction strength g as a function of applied voltages in Fig. 4.8.

Large interaction strength and small derivative of qubit energy against voltage can be achieved by the large coupling capacitance Cc between each qubits. This seems to show that one can suppress errors by increasing Cc. We discuss about the errors during controlled-phase gate operation in following section.

4.4.4 Effects on interaction from change in electric field

To evaluate the performance of our scheme, we focus on two types of errors due to the fluctuation of applied voltage and time jittering.

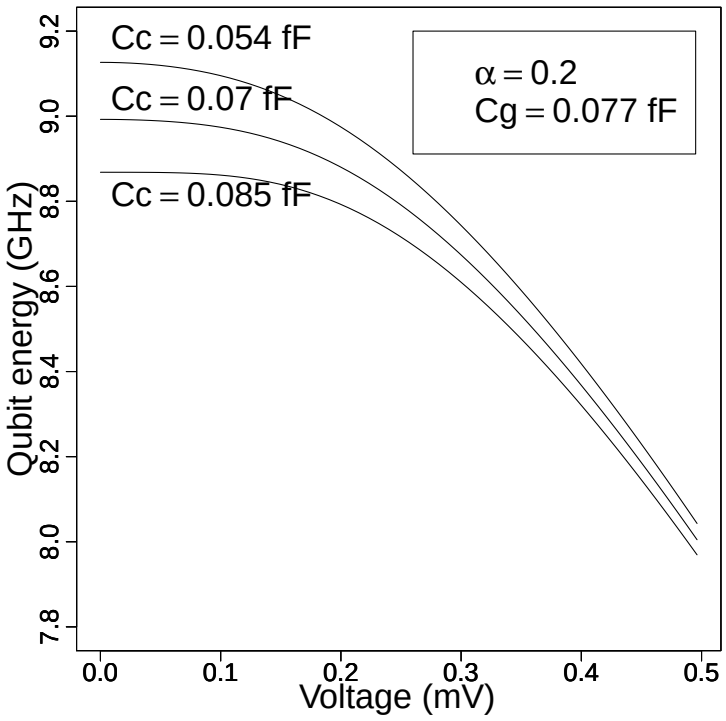

Figure 4.7: The voltage dependence of the qubit energy Δ of the circuit in Fig. 4.6. Here, both of the gate capacitance $C_g^l = 0.077$ fF.

The fluctuation of applied voltage

Firstly, we analyze the dephasing errors due to the fluctuations of applied voltage. We define this type of error ϵ_d and dephasing time T_2 as follows:

$$\epsilon_d = \frac{t_{cp}}{T_2}, t_{cp} = \frac{\pi}{g}, T_2 = \frac{1}{|\frac{dE_{01}}{dv}|\delta v} \tag{4.75}$$

where we assume $t_{cp} << T_2$. Here, t_{cp} denotes the necessary time to perform a controlled-phase gate with Ising type interaction, v denotes the external voltage of each qubit, and δv denotes the fluctuation width of v. It is worth mentioning that ϵ_d has a linear relationship with δv. To make ϵ_d smaller, We should obtain a parameter set where the absolute value of the gradient of the qubit energy E_{01} is small and the interaction strength g is large.

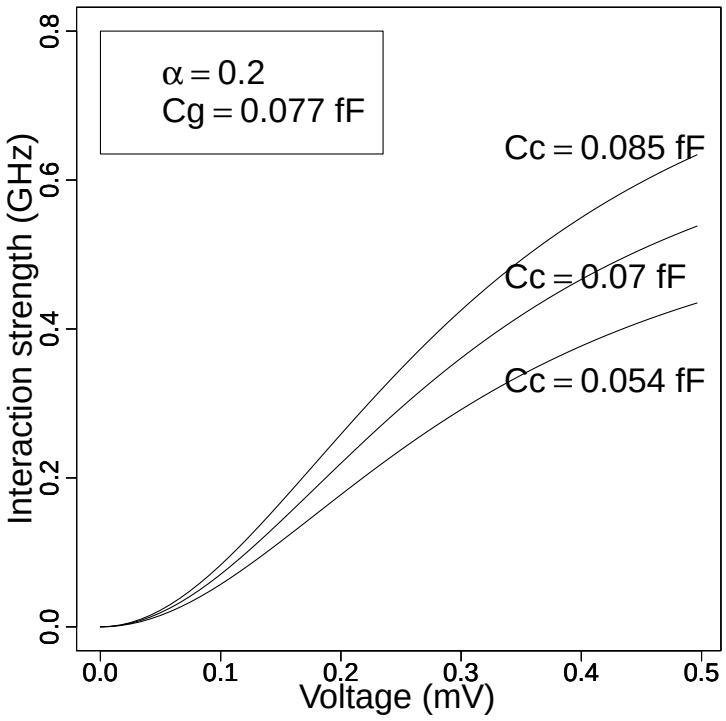

Figure 4.8: Interaction strength g between two qubits of the circuit in Fig. 4.6. Here, both of the gate capacitance $C_g^l = 0.077$ fF.

Time jittering

Secondly, we investigate the jitter error of a two-qubit gate operation. The Ising type interaction can implement the controlled-phase gate

$$U_{CZ}^{(1,2)}(t) \quad = \quad \exp\left(-i4gt\frac{1+\sigma_Z^{(1)}}{2}\frac{1+\sigma_Z^{(2)}}{2}\right), \tag{4.76}$$

where g denotes the interaction strength in Eq. (4.74), $t = \frac{\pi}{4g}$ denotes the time to apply voltages, and $U_{CZ}^{(1,2)}$ denotes a controlled-phase gate between qubit 1 and 2. By performing the controlled-phase gate on two qubits which are initialized to $|{+}{+}\rangle_{12}$ state, we can obtain the two-qubit cluster state. But, the applied voltages may not create the desired state due to error in the timing $t' = t + \delta t$, where δt is timing jitter. We introduce the controlled-phase gate $U_{CZ}^{(1,2)}(t)$ including the

timing error to calculate a gate fidelity $F_{CZ} = |\langle\phi|\phi'\rangle|^2$ with

$$|\phi\rangle = U_{CZ}^{(1,2)}(t)|{+}{+}\rangle, |\phi'\rangle = U_{CZ}^{(1,2)}(t')|{+}{+}\rangle. \tag{4.77}$$

Here, we define the timing error $\epsilon_{tim} = 1 - F_{CZ}$, and the local error $\epsilon_{loc}(= \epsilon_d + \epsilon_{tim})$.

We discuss how much fluctuations of the voltage (δv) can be expected in the actual experiment. Usually, as we increase the applied voltage, the fluctuation of the voltage also increases so that we should have $\delta v \propto V$ where V denotes the applied voltage. Throughout of this paper, we set $\frac{\delta v}{V} = 0.01\% - 0.1\%$, which could be realized due to recent development of fabrication technologies. Hence, we decided to use a fluctuation of the voltage of 0.2 μV.

Also, we discuss the time jittering error. Throughout of this paper, we consider a coupling strength that is an order of tens of MHz or hundreds of MHz. (, which means that the pulse length for the two-qubit gate is an order of several tens to several hundreds of MHz.) We may have a time jittering that could be around 0.1% or 0.01% compared with the coupling length. So we decided to use a time jittering of $\delta t = 50$ ps.

We show the ϵ_{loc} against the applied voltage V_e with the particular values of Cc in Fig. 4.9. The threshold of local errors for fault tolerant quantum computation is known to be around 1%. Also, it is known that, if the error rate is close to the threshold, the necessary number of qubits for the computation drastically increases [84, 30]. Therefore, we set the threshold to $\epsilon_{loc} = 0.1\%$. As shown in Fig. 4.8, we can increase the coupling strength g by increasing Cc. Meanwhile, the strong coupling strength cause the large timing error. Therefore, as shown in Fig. 4.9, the optimal voltage exists for each of the Cc which minimize the total local error. In addition, by increasing Cc, the total error tends to be smaller. This result show that the large Cc has an advantage for quantum error correction against local errors. However, for multi-qubit systems, increasing Cc causes a different problem. Unwanted interaction strength between non-nearest neighbor qubits increases due to the large Cc. For this reason, the Cc should be set to be around 0.075 fF. The detail of this will be discussed in Subsection 4.5.4.

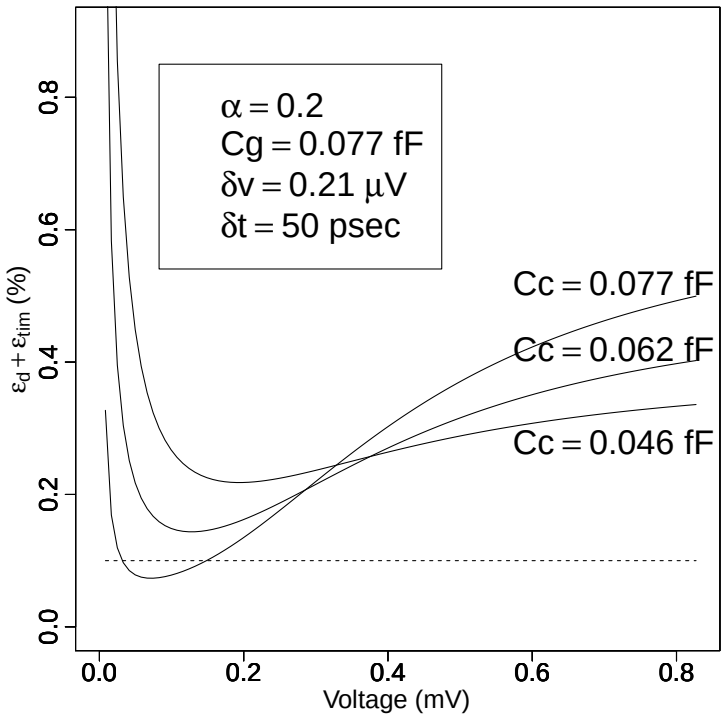

Figure 4.9: The total local error $\epsilon_{loc}(= \epsilon_d + \epsilon_{tim})$ as a function of voltage with different coupling capacitance Cc. Here, we set the fluctuation width of voltage $\delta v = 0.21$ μV and the timing jitter $\delta t = 50$ psec. Dashed line denotes an error of 0.1%.

4.5 Multi-qubit system

In this section, we generalize our scheme to multi-qubit system. Firstly, we discuss how to control the capacitive interactions between superconducting flux qubits via applied voltage. Secondly, we show how to apply our scheme to generate a two dimensional cluster state using superconducting flux qubits arranged on square lattice.

4.5.1 Generating interaction between multi-qubits system

Here, we discuss the interactions between capacitively coupled N flux qubits that are arranged in one dimensional line as shown in Fig. 4.10. For simplicity, we assume homogeneous flux qubits.

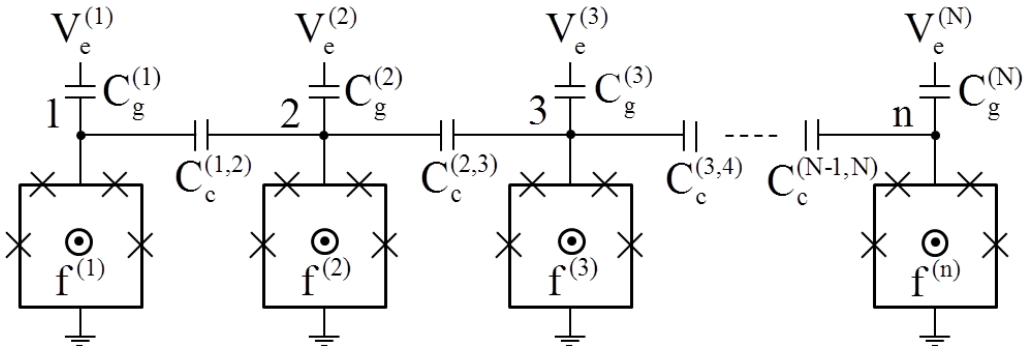

Figure 4.10: A flux qubit at the site $j(1 < j < N)$ couples with the nearest neighbor qubits via capacitance $C_c^{(j,j\pm1)}$. For simplicity, we assume homogeneous flux qubits. Each node j represents the superconducting islands. Each qubit has four Josephson junctions. Two Josephson junctions directly connected to the node have the Josephson energies and capacitances that are α times larger than the other two Josephson junctions.

4.5.2 Hamiltonian

Josephson phases $\varphi_n^{(k)}$ are subject to the following equation:

$$\varphi_1^{(k)} + \varphi_2^{(k)} + \varphi_3^{(k)} + \varphi_4^{(k)} = -2\pi f^{(k)} \tag{4.78}$$

where $\varphi_n^{(k)}$ and $f^{(l)}$ denote the phase of each Josephson junction and external magnetic flux of qubit k.

We now consider the total potential energy U and the total electric energy T of the circuit in Fig. 4.10 as follows:

$$U = \sum_{l=1}^{n}\sum_{k=1}^{4} E_{j(k)}^{(l)} \left(1 - \cos\varphi_k^{(l)}\right), \tag{4.79}$$

$$\begin{aligned} T = {} & \frac{1}{2}\sum_{l=n}^{2}\sum_{k=1}^{4} C_{j(k)}^{(l)} \left(\frac{\Phi_0}{2\pi}\dot{\varphi}_k^{(l)}\right)^2 + \frac{1}{2}\sum_{l=1}^{n} C_g^{(l)} \left(V_e^{(l)} - V_I^{(l)}\right)^2 \\ & + \sum_{l=1}^{n-1} \frac{1}{2} C_c^{(l,l+1)} \left(V_I^{(l)} - V_I^{(l+1)}\right)^2 \end{aligned} \tag{4.80}$$

where $C_g^{(l)}$, $V_e^{(l)}$, and $V_I^{(l)}$ denote gate capacitance, applied external voltage, and the electric potential of the island including node l for the l th qubit respectively.

$C_c^{(l,l+1)}$ denotes the coupling capacitance between node l and $l+1$.

From the phase constraints in (4.78), each phase φ_k and the time derivative of phase $\dot{\varphi}_k$ can be described using φ' and $\dot{\varphi}'$ as follows:

$$\varphi^{(k)} = \begin{pmatrix} \varphi_1^{(k)} \\ \varphi_2^{(k)} \\ \varphi_3^{(k)} \\ \varphi_4^{(k)} \end{pmatrix}, \varphi = \begin{pmatrix} \varphi^{(1)} \\ \varphi^{(2)} \\ \vdots \\ \varphi^{(n)} \end{pmatrix}, \ \varphi_k = \sum_j B_{kj}\varphi'_j + F_k, \varphi' = \begin{pmatrix} \boldsymbol{\varphi'_1} \\ \boldsymbol{\varphi'_2} \\ \vdots \\ \boldsymbol{\varphi'_{3n}} \end{pmatrix} \quad (4.81)$$

$$\dot{\varphi}^{(k)} = \begin{pmatrix} \dot{\varphi}_1^{(k)} \\ \dot{\varphi}_2^{(k)} \\ \dot{\varphi}_3^{(k)} \\ \dot{\varphi}_4^{(k)} \end{pmatrix}, \dot{\varphi} = \begin{pmatrix} \dot{\varphi}^{(1)} \\ \dot{\varphi}^{(2)} \\ \vdots \\ \dot{\varphi}^{(n)} \end{pmatrix}, \ \dot{\varphi}_k = \sum_j B_{kj}\dot{\varphi}'_j, \dot{\varphi}' = \begin{pmatrix} \boldsymbol{\dot{\varphi}'_1} \\ \boldsymbol{\dot{\varphi}'_2} \\ \vdots \\ \boldsymbol{\dot{\varphi}'_{3n}} \end{pmatrix}, \quad (4.82)$$

Here, we introduce following B and F

$$B^{(k)} = \begin{pmatrix} 1 & 0 & 0 \\ 0 & 1 & 0 \\ 0 & 0 & 1 \\ -1 & -1 & -1 \end{pmatrix} \quad , \quad B = \begin{pmatrix} B^{(1)} & & & 0 \\ & B^{(2)} & & \\ & & \ddots & \\ 0 & & & B^{(n)} \end{pmatrix}, \quad (4.83)$$

$$F^{(k)} = \begin{pmatrix} \mathbf{0} \\ \mathbf{0} \\ \mathbf{0} \\ \boldsymbol{-2\pi f^{(k)}} \end{pmatrix} \quad , \quad F = \begin{pmatrix} \boldsymbol{F^{(1)}} \\ \boldsymbol{F^{(2)}} \\ \vdots \\ \boldsymbol{F^{(n)}} \end{pmatrix}. \quad (4.84)$$

We also introduce the area ratio $A_n^{(l)}$ of each JJn of qubit l as follows:

$$A_1^{(l)} = A_4^{(l)} = 1, \ A_2^{(l)} = A_3^{(l)} = \alpha, \text{ where } l \in \{1, 2, .., n\}. \quad (4.85)$$

As with the two qubit system in 4.4.2, we can rewrite the total Josephson energy

U using B, F, and $A_n^{(l)}$.

$$U = E_J \sum_{k,l} A_k^{(l)} (1 - \cos(\sum_j B_{kj}\varphi_j' + F_k)). \tag{4.86}$$

Next, we define the effective mass M as follows:

$$M = \frac{e^2}{2E_C}\left(\frac{\Phi_0}{2\pi}\right)^2 \left(B^{\mathrm{T}} A_{mat}^{mul} B + B^{\mathrm{T}} D^{\mathrm{T}} \left(\Gamma_{mat}^{mul} + 2C_c^{'}\right) DB\right). \tag{4.87}$$

where, A_{mat}^{mul} and Γ_{mat}^{mul} denote following matrices:

$$A_{mat}^{(k)} = \begin{pmatrix} 1 & 0 & 0 & 0 \\ 0 & \alpha & 0 & 0 \\ 0 & 0 & \alpha & 0 \\ 0 & 0 & 0 & 1 \end{pmatrix} \quad , \quad A_{mat}^{mul} = \begin{pmatrix} \boldsymbol{A_{mat}^{(1)}} & & & 0 \\ & \boldsymbol{A_{mat}^{(2)}} & & \\ & & \ddots & \\ 0 & & & \boldsymbol{A_{mat}^{(n)}} \end{pmatrix}, \tag{4.88}$$

$$\Gamma_{mat}^{(k)} = \begin{pmatrix} \mathbf{0} & \mathbf{0} & \mathbf{0} \\ \mathbf{0} & \boldsymbol{\gamma} & \mathbf{0} \\ \mathbf{0} & \mathbf{0} & \mathbf{0} \end{pmatrix} \quad , \quad \Gamma_{mat}^{mul} = \begin{pmatrix} \boldsymbol{\Gamma_{mat}^{(1)}} & & & 0 \\ & \boldsymbol{\Gamma^{(2)}} & & \\ & & \ddots & \\ 0 & & & \boldsymbol{\Gamma^{(n)}} \end{pmatrix}. \tag{4.89}$$

Here, each γ correspond to the gate capacitor $C_g^{(k)}$ which is connected to the middle island of each qubit as shown in Fig. 4.10. In this case, the capacitance of $C_g^{(k)}$ satisfy the following conditions:

$$C_g^{(k)} \quad = \quad C_{J(1)}\gamma = \frac{e^2}{2E_C}\gamma. \tag{4.90}$$

C_c' denotes the coupling capacitance between each qubit and satisfy the following conditions:

$$\frac{e^2}{2E_C} C_{c(i,j)}^{'} \equiv -C_{c(i,j)} + \delta_{i,j} \sum_k C_{c(i,k)}. \tag{4.91}$$

To describe the circuit Hamiltonian, we also introduce V_E and P_i:

$$V_E^{(k)} = \begin{pmatrix} 0 & V_e^{(k)} & 0 \end{pmatrix}, V_E = \begin{pmatrix} V_E^{(1)} & V_E^{(2)} & \cdots & V_E^{(n)} \end{pmatrix}, P_i = -i\hbar \frac{\partial}{\partial \varphi_i'}. \quad (4.92)$$

Then, the circuit Hamiltonian becomes as follows:

$$H = \frac{1}{2}\left(P^{\mathrm{T}} + \frac{e^2}{E_C}\frac{\Phi_0}{2\pi} B^{\mathrm{T}} D^{\mathrm{T}} \Gamma_{mat}^{mul} V_E^{\mathrm{T}}\right) M^{-1} \left(P + \frac{e^2}{E_C}\frac{\Phi_0}{2\pi} V_E \Gamma_{mat}^{mul} D B\right) + U. \quad (4.93)$$

4.5.3 Simulation

In this simulation, we we can derive the effective 2^n-level ($|gg..g\rangle_{12..n}$, $|gg..e\rangle_{12..n}$, .. , and $|ee..e\rangle_{12..n}$) Hamiltonian $\hat{H}_{ge}$ of the eigenspace spanned by ground states and first excited states of each qubits without interactions for all $f^{(k)} = 0.5$.

Step 1 We construct the local Hamiltonian of each qubit $H_{local}^{(k)}$ without considering capacitive coupling. $H_{local}^{(k)}$ and the one qubit Hamiltonian in Eq. 4.31 are the same except for the parameters F and V_E.

Step 2 We set $f^{(k)} = 0.5$ and arbitrary $V_e^{(k)}$. After that we calculate the ground state $|g^{(k)}\rangle$ and the first excited state $|e^{(k)}\rangle$ from $H_{local}^{(k)}$ using the scheme in 4.3.2.

Step3 We set $C_c^{(1,2)}$ and calculate the inverse of the effective math M^{-1} in Eq. (4.87).

Step4 We simulate the following functions to obtain $\hat{H}_{ge}$:

$$\hat{H}_{ge} = \sum_{v_L^{(1)}, v_R^{(1)}, v_L^{(2)}, v_R^{(2)}, .., v_L^{(n)}, v_R^{(n)}} |v_L^{(1)} v_L^{(2)} .. v_L^{(n)}\rangle \langle v_L^{(1)} v_L^{(2)} .. v_L^{(n)}| H |v_R^{(1)} v_R^{(2)} .. v_R^{(n)}\rangle \langle v_R^{(1)} v_R^{(2)} .. v_R^{(n)}| \quad (4.94)$$

$$\begin{aligned} \langle v_L^{(1)} v_L^{(2)} .. v_L^{(n)}| H |v_R^{(1)} v_R^{(2)} .. v_R^{(n)}\rangle = & E_J U(v_L^{(1)}, v_R^{(1)}, v_L^{(2)}, v_R^{(2)}, .., v_L^{(n)}, v_R^{(n)}, U^{(1)}, U^{(2)}, .., U^{(n)}) \\ & + E_C T(v_L^{(1)}, v_R^{(1)}, v_L^{(2)}, v_R^{(2)}, .., v_L^{(n)}, v_R^{(n)}, N, M^{-1}, K) \end{aligned} \quad (4.95)$$

where N denotes the size of matrices, $v_L^{(k)}$ and $v_R^{(k)}$ satisfy the following conditions,

$$v_L^{(1)}, v_R^{(1)} \in \{g^{(1)}, e^{(1)}\},\ v_L^{(2)}, v_R^{(2)} \in \{g^{(2)}, e^{(2)}\},\ ..\ v_L^{(n)}, v_R^{(n)} \in \{g^{(n)}, e^{(n)}\}. \quad (4.96)$$

The potential energy of nth qubit $U^{(n)}$ becomes

$$U^{(1)} = E_J \sum_{k=4n-3}^{4n} A_k(1 - \cos(\sum_j B_{kj}\varphi'_j + F_k)), \quad (4.97)$$

Effects of external voltage K becomes

$$K = \frac{e^2}{E_C}\frac{\Phi_0}{2\pi} V_E \Gamma_{mat} DB, \quad (4.98)$$

$f^{(j)}$ denotes the external magnetic flux through the loop of the j th qubit.

Here, the function $U(v_L^{(1)}, v_R^{(1)}, v_L^{(2)}, v_R^{(2)}, .., v_L^{(n)}, v_R^{(n)}, U^{(1)}, U^{(2)}, .., U^{(n)})$ denotes

$$\begin{aligned} &U(v_L^{(1)}, v_R^{(1)}, v_L^{(2)}, v_R^{(2)}, .., v_L^{(n)}, v_R^{(n)}, U^{(1)}, U^{(2)}, .., U^{(n)}) \\ &= \langle v_L^{(1)}|U^{(1)}|v_R^{(1)}\rangle\langle v_L^{(2)} v_L^{(3)}..v_L^{(n)}|v_R^{(2)} v_R^{(3)}..v_R^{(n)}\rangle \\ &\quad + \langle v_L^{(1)}|v_R^{(1)}\rangle\langle v_L^{(2)}|U^{(2)}|v_R^{(2)}\rangle\langle v_L^{(3)} v_L^{(4)}..v_L^{(n)}|v_R^{(3)} v_R^{(4)}..v_R^{(n)}\rangle \\ &\quad + .. + \langle v_L^{(1)} v_L^{(2)}..v_L^{(n-1)}|v_R^{(1)} v_R^{(2)}..v_R^{(n-1)}\rangle\langle v_L^{(n)}|U^{(n)}|v_R^{(n)}\rangle. \end{aligned} \quad (4.99)$$

Next, we show details of the function $T(v_L^{(1)}, v_R^{(1)}, v_L^{(2)}, v_R^{(2)}, .., v_L^{(n)}, v_R^{(n)}, N, M^{-1}, K)$ as follows:

---

function T(vector $v_L^{(1)}$, vector $v_R^{(1)}$, vector $v_L^{(2)}$, vector $v_R^{(2)}$, .. , vector $v_L^{(n)}$, vector $v_R^{(n)}$, int N, matrix M^{-1}, vector K), Input: Set vectors $v_L^{(i)}$ and $v_R^{(i)}$in Eq. (4.95), the size of matrices N, the inverse of the effective mass M^{-1} in Eq. (4.87), and effects of external voltage K in Eq. (4.98).

Output: $2N + 1$ x $2N + 1$ matrix of momentum energy T.

Output: $2N + 1$ x $2N + 1$ matrix of momentum energy T.

$q = n$ **: number of qubits**

$w = length(K);$ **: number of wave functions**

for $k = 0 : w - 1$ **do**

$PMatrix_{(k)} = diag((-N : N) + K(k), 0)$

end for

for $k = 0 : \frac{w}{q} - 1$ **do**

$IMatrix_{(k)} = identity(2 * N + 1)$ **: matrix for initialization**

end for

for $a = 0 : w - 1$ **do**

for $b = 0 : w - 1$ **do**

$P_0 = P_1 = .. = P_{(n-1)} = \{IMatrix\}$ **: initialize**

$Phi_{(0)} = Phi_{(1)} = .. = Phi_{(n-1)} = identity((2 * N + 1)^3)$ **: initialize**

$P_{0(a\%3)} = PMatrix_{(a)}$

$P_{1(b\%3)} = PMatrix_{(b)}$

$\Phi_{(a/3)} * = P_{0(0)} \otimes P_{0(1)} \otimes P_{0(2)}$

$\Phi_{(b/3)} * = P_{1(0)} \otimes P_{1(1)} \otimes P_{1(2)}$

$T = T + M^{-1}_{(a,b)} \langle v^{(1)}_L | Phi_{(0)} | v^{(1)}_R \rangle \langle v^{(2)}_L | \Phi_{(1)} | v^{(2)}_R \rangle .. \langle v^{(n)}_L | \Phi_{(n-1)} | v^{(n)}_R \rangle$

end for

end for

return T

end function

When all flux $f^{(j)}$ are 0.5, the system Hamiltonian is described as follows.

$$\hat{H} = \sum_{l=1}^{N} \frac{1}{2} \Delta^{(l)} \sigma_Z^{(l)} + \sum_{l,l'=1}^{N} g_{(|l-l'|)} \sigma_Z^{(l)} \sigma_Z^{(l')} \tag{4.100}$$

where $\Delta_{(l)}$ denotes the energy of the l th qubit, $g_{(|l-l'|)}$ denotes the interaction strength between each pair of qubits at a site (l, l'), and $|l - l'|$ denotes the site distance between these qubits (e.g. when qubit l and l' are nearest neighbor pair, $|l - l'| = 1$.).

4.5.4 Generation of a one dimensional cluster state

Non-nearest neighbor interactions cause spatially-correlated errors that are difficult to correct by quantum error correction. In this subsection, we show the way

to evaluate this error. We define the ratio between nearest neighbor interaction $g(= g_{(1)})$ and next-nearest neighbor interaction $g_{(2)}$ as $R\left(= \frac{g_{(2)}}{g_{(1)}}\right)$ where all qubits are applied voltage V_e. We show that the interaction strength $g(|l-l'|)$ decreases exponentially as the site distance $|l-l'|$ increases, and the Ratio R depends on the coupling capacitance Cc between each qubit. We show the interaction strengths of 6 qubits system as a function of Cc in Fig. 4.11.

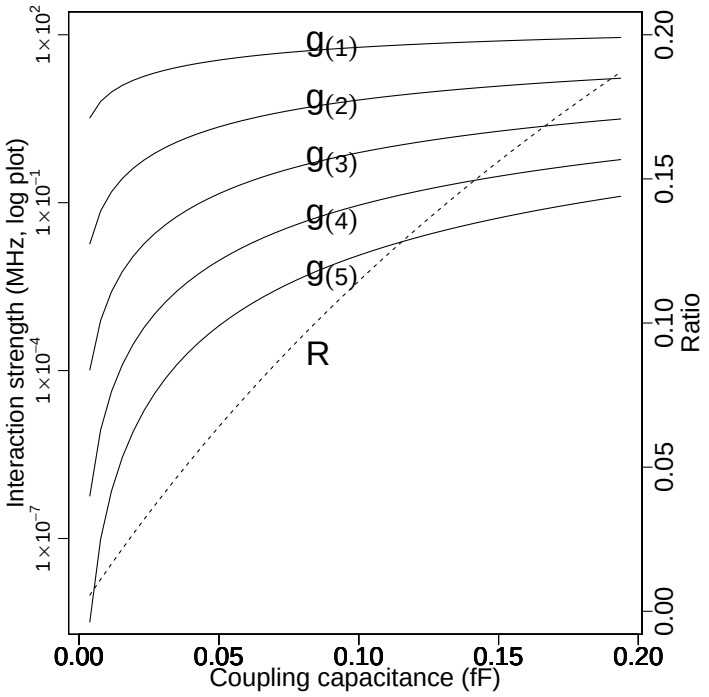

Figure 4.11: The Cc dependence of the interaction strengths and the coupling ratio $R\left(= \frac{g_{(2)}}{g_{(1)}}\right)$ where $g(|l-l'|)$ denotes the interaction strength between a pair of qubits at a site $(l-l')$.

If we apply voltage on all qubits, interaction occurs between such qubits. The total error $\epsilon_{non}^{(j)}$ caused by non-nearest neighbor interactions on j th qubit during controlled-phase operation is calculated as follows:

$$\epsilon_{non}^{(j)} = \sum_{n=2}^{N/2} g_{(n)} t_{cp} m_{(n)} = \sum_{n=2}^{N/2} \frac{\pi}{4} R^{(n-1)} m_{(n)} \tag{4.101}$$

where n denotes the site distance between the j th qubit and the coupled non-

nearest neighbor qubits, $m_{(n)}^{(j)}$ denotes the number of such non-nearest qubits.

Such existence of the spatially-correlated error will increase the threshold for quantum error correction [2]. Large capacitance tends to decrease local errors as shown in Fig. 4.9, while large capacitance induces more spatially-correlated errors as shown in Fig. 4.11. However, when we consider the spatially-correlated error, the error threshold value of the surface code is not well studied. Thus, we set the upper bound of the spatially-correlated error on each qubit $\epsilon_{non} \leq \frac{1}{10000}$ which is an order of magnitude smaller than the threshold of local error for surface coding scheme. If this condition is satisfied, we assume that spatially-correlated error is small enough to perform a fault-tolerant quantum computation. When we apply voltage on all qubits to perform controlled-phase gates to all pairs of nearest neighbor qubit, we cannot make both local errors and spatially-correlated error smaller than these threshold for any value of Cc. Therefore, we do not apply voltage on all qubits but apply voltage on some of them. We choose pairs of nearest neighbor qubits that we will apply the voltage, and we set a site distance p between the pairs. Then, if R is small enough, ϵ_{non} of each qubit is the following equation:

$$\epsilon_{non}^{(j)} = \sum_{n=p}^{N/2} \frac{\pi}{4} R^{(n-1)} \leq \frac{1}{10000} \tag{4.102}$$

where p is the site distance between qubits applied by voltage.

Since there are many parameters on the interaction Hamiltonian, it is difficult to find an optimum set of parameters that minimize both of local and spatially-correlated errors. Therefore, we fix the following parameters: $\alpha = 0.2$, $\delta_v = 0.21$ μV, $\delta_t = 50$ psec. To determine a minimum site distance p while suppressing the correlated errors to be under 0.01 %, we show the Cc and V dependences of the errors with $p = 4, 5$ in Fig. 4.12 and Fig. 4.13. As shown in Fig. 4.12, when $p = 4$, the ϵ_{non} exceeds 0.01 % around $Cc = 0.04$ fF. We cannot sufficiently suppress local errors using coupling capacitance smaller than 0.04 as shown in Fig. 4.9. Thus, the site distance p should be larger than 5. Meanwhile, when $p = 5$, the ϵ_{non} exceeds 0.01 % around $Cc = 0.09$ fF. Then the total error of the controlled-

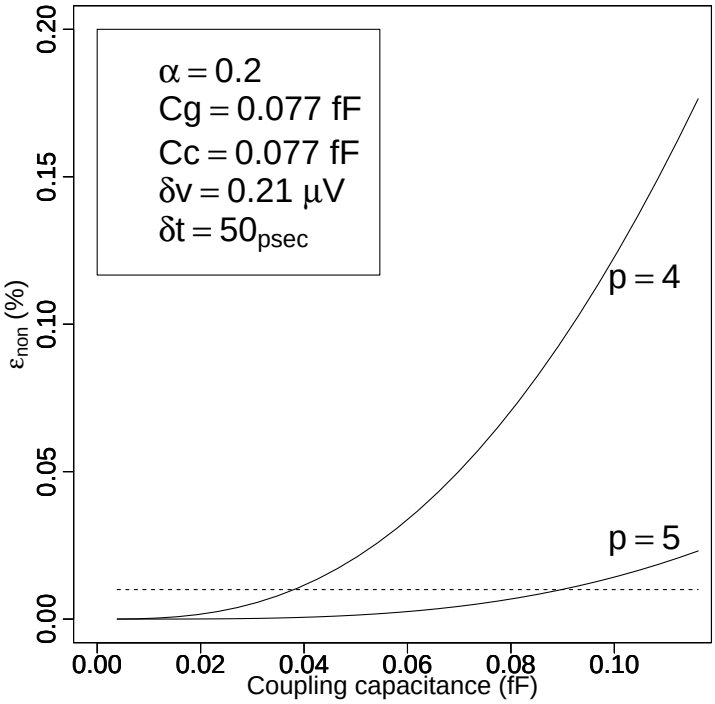

Figure 4.12: The V dependence of the spatially-correlated error. Dashed line corresponds to an error of 0.1 %.

phase operation can be sufficiently suppressed to be less than 0.1 % using the coupling capacitance Cc around 0.077 fF as shown in Fig. 4.13. Therefore, it is preferable that the site distance $p = 5$ be selected. In order to adopt sufficiently large coupling capacitance such that the ϵ_{loc} below 0.1 %, we need to choose sufficiently large p such that the ϵ_{non} below 0.01 %. We discuss about the way which can further reduce p in the following.

The p determines the maximum number of controlled-phase gates that are performed simultaneously on the same system. For example, we can perform $\lfloor \frac{N-2}{p+1} \rfloor + 1$ controlled-phase gates in parallel using N-qubits one dimensional system. If we can use the smaller p without adding extra errors, we can perform more controlled-phase gates in parallel, so that we can generate a cluster state within a shorter operating time. For this purpose, we introduce the spin echo technique where implementation of a π pulse (single qubit σ_X rotation) to the target qubit could refocus the dynamics of the spin so that effects of interactions

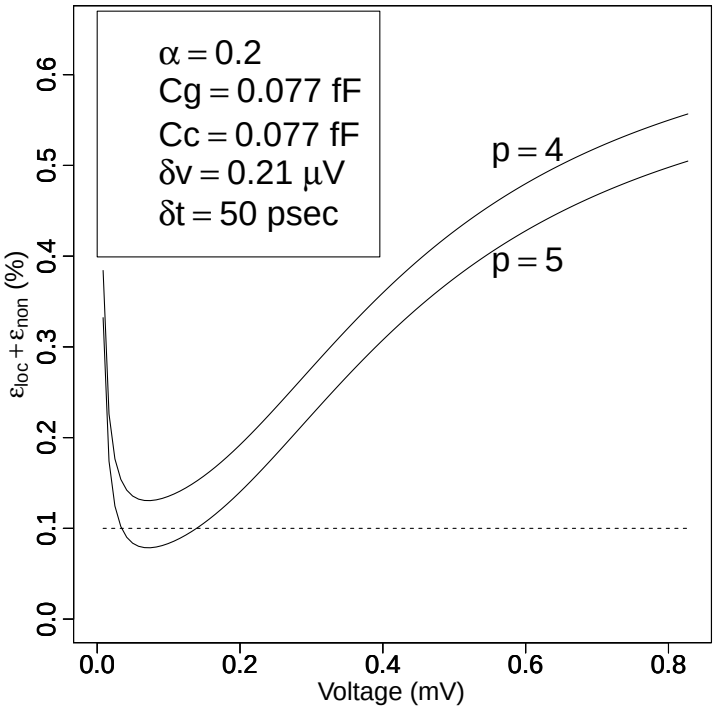

Figure 4.13: The V dependence of the total errors. Dashed line corresponds to an error of 0.1 %.

on the target qubit should be cancelled out. We apply two π pulses to pairs of qubits to suppress spatially-correlated errors. For example, we set three qubits in a raw and apply voltage $V_e^{(n)}$ to the n th qubits ($n = 1, 2, 3$) as shown in Fig. 4.14, where $V_e^{(1)}$ and $V_e^{(2)}$ are equal, $V_e^{(3)}$ is an arbitrary voltage, and the strength of interaction between qubit 1 and 2 is g. We set each qubit to be prepared in $|+\rangle$ state, let the state evolve for a time $t_{cp}/2$, perform two π pulses to qubit 1 and 2, and let the state evolve for a time $t_{cp}/2$. The final state become as follows:

$$\hat{U}|+++\rangle_{123} = \frac{1}{\sqrt{2}}\left(|+0\rangle_{12} + |-1\rangle_{12}\right) \otimes |+\rangle_3. \tag{4.103}$$

Here, the interactions $g_{(1)}\sigma_Z^{(2)}\sigma_Z^{(3)}$ and $g_{(2)}\sigma_Z^{(1)}\sigma_Z^{(3)}$ are cancelled out due to the π pulses and we obtain a cluster state between qubit 1 and 2.

This method can be applied with the case of arbitrary number of qubits. The general rules are follows: let us consider a pair of qubits. If we perform π pulses

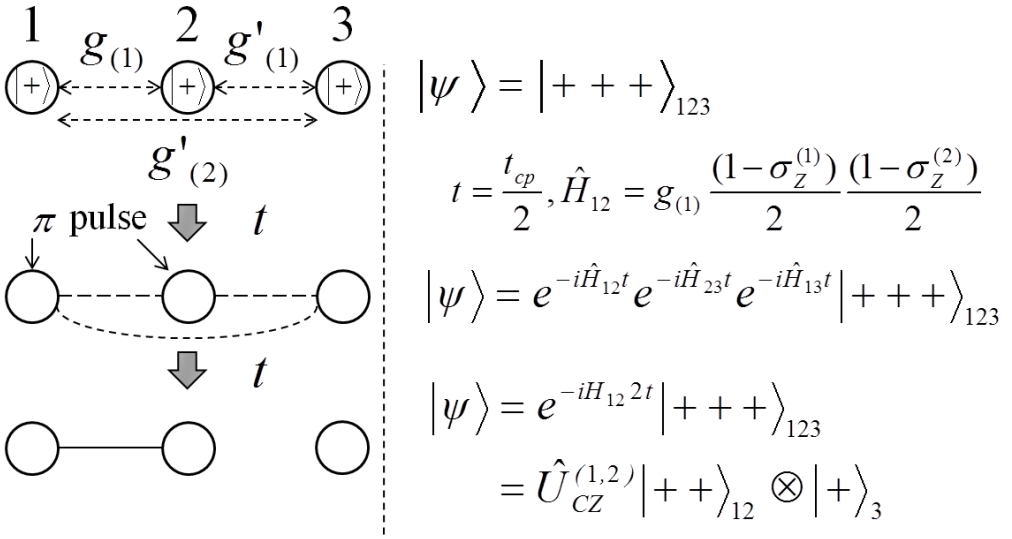

Figure 4.14: When we perform a π pulse on qubit 1 and 2 at $t = t_{cp}/2$, the nearest neighbor interaction between qubit 2 and 3 and the non-nearest neighbor interaction between qubit 1 and 3 are cancelled out. In such way, we can perform controlled-phase gate without changing the state of other qubits.

on both of qubits, the interaction between them is not affected by these pulses. On the other hand, if we perform π pulse on one of them, the interaction between them is cancelled out. These properties would be crucial for generating a cluster state as we will describe.

For generating a large one dimensional cluster state using N qubits of the circuit in Fig. 4.10, we show the procedure as follows:

Step 1 We apply voltage to $(3n-2)$ th and $(3n-1)$ th qubit for performing controlled-phase gates between $(3n-2)$ th and $(3n-1)$ th qubit where $n = 1, 2, \cdot\cdot, \lfloor \frac{N+1}{3} \rfloor$.

Step 2 We apply voltage to $(3n-1)$ th and $3n$ th qubit for performing controlled-phase gates between $(3n-1)$ th and $3n$ th qubit where $n = 1, 2, \cdot\cdot, \lfloor \frac{N+1}{3} \rfloor$.

Step 3 We apply voltage to $3n$ th and $(3n+1)$ th qubit for performing controlled-phase gates between $(3n-1)$ th and $3n$ th qubit where $n = 1, 2, \cdot\cdot, \lfloor \frac{N+1}{3} \rfloor$.

At each step of the above procedure, $\lfloor \frac{N-1}{3} \rfloor$ controlled-phase gate are per-

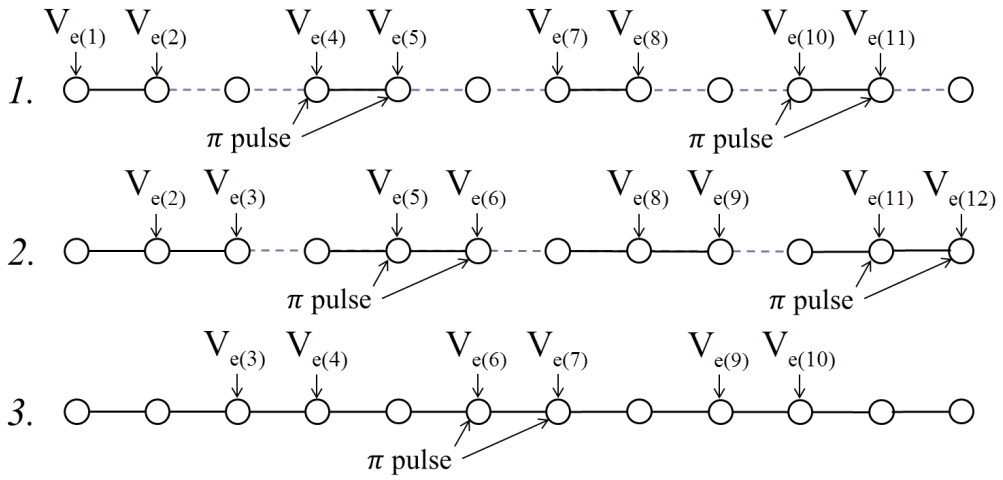

Figure 4.15: The 3-step procedure for generating a one dimensional cluster state. Step 1. We initialize $3n-2$ th and $3n-1$ th qubits in $|+\rangle$. Here, $n = 1, 2, \cdot\cdot, \lfloor \frac{N+1}{3} \rfloor$ where $\lfloor x \rfloor$ is the integer part of x. After that we apply voltage on $3n-2$ th and $3n-1$ th qubits. Let the state evolve for a time $t_{cp}/2$, perform π pulses to $6n-2$ th and $6n-1$ th qubits, and let the state evolve for a time $t_{cp}/2$. After these operations, controlled-phase gates have been performed between qubit $3n-2$ and $3n-1$. Step 2. We initialize $3n$ th qubits in $|+\rangle$. After that, similar to the Step 1, we perform controlled-phase gates between qubit $3n-1$ and $3n$. Step 3. We initialize $3n+1$ th qubits in $|+\rangle$. After that, similar to the Step 1 and 2, we perform controlled-phase gates between qubit $3n$ and $3n+1$.

formed in parallel. At each step, we will perform the following procedure to perform the controlled-phase gate. Firstly, prepare the qubit state in $|+\rangle$. Secondly, let the state evolve for a time $t = t_{cp}/2$ according to the Hamiltonian described in Eq. 4.100. Thirdly, perform the π pulses to suppress the non-local interaction. Finally, let the state evolve for a time $t = t_{cp}$. We show the details of these operations in Fig. 4.15 and explain how the non-local interaction is suppressed in Fig. 4.16. When all coupling capacitance are $Cc \leq 0.077$ fF, the spatially-correlated error on each qubits become as follows:

$$\epsilon_{non}^{(j)} = \sum_{n=5}^{N/2} \frac{\pi}{4} R^{(n-1)} m_{(n)} \simeq \frac{\pi}{4}(R^4 + 2R^5) \leq \frac{1}{10000} \tag{4.104}$$

The k th qubit is affected by mainly three non-local interactions as shown in

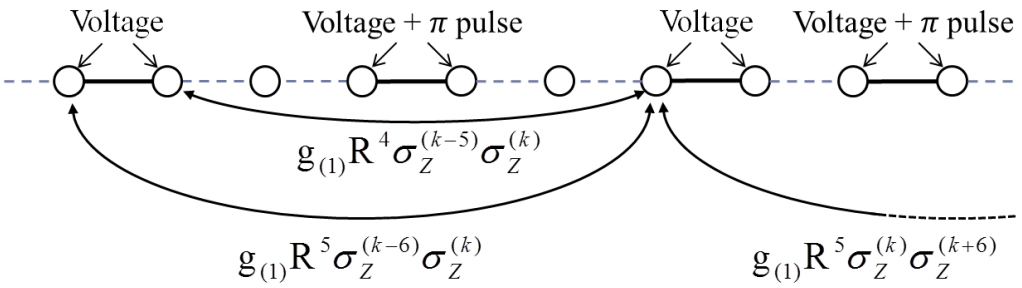

Figure 4.16: The influence of non-local interactions. During the controlled-phase gate, each target qubit are affected by non-local interactions. We show the strength of mainly three non-local interactions with k th qubit. These interactions are not cancelled out by π pulses.

Fig. 4.16. The strength of the largest interaction is $g_{(1)}R^4$, and the strength of the other two interactions are $g_{(1)}R^5$. The remaining non-local interactions are negligibly small.

4.5.5 Generation of a two dimensional cluster state

Next, we show how to generate a two dimensional cluster state using N^2 flux qubits arranged on $N \times N$ square lattice. We show a part of the circuit in Fig. 4.17. $f^{(j,k)}$ denotes the external magnetic flux through the loop of the qubit at site (j,k). Here, (j,k) corresponds to the lattice point. When all flux $f^{(j,k)}$ are 0.5, the system Hamiltonian is described as follows:

$$\hat{H} = \sum_{(l,m)} \frac{\Delta^{(l,m)}}{2} \sigma_Z^{(l,m)} + \sum_{((l,m),(l',m'))} g_{(|l-l'|+|m-m'|)} \sigma_Z^{(l,m)} \sigma_Z^{(l',m')} \qquad (4.105)$$

where $\Delta_{(l,m)}$ denotes the energy of the qubit at site (l,m), $g_{(|l-l'|+|m-m'|)}$ denotes the interaction strength between each pair of qubits at site (l,m) and (l',m'), and $|l-l'|+|m-m'|$ denotes the site distance between these qubits.

Here, we show the 12-step procedure as follows for generating a two dimensional cluster state.

Step 1-3 We perform $(N-1)\lfloor \frac{N}{4} \rfloor$ controlled-phase gate to generate $\lfloor \frac{N}{4} \rfloor$ one dimensional cluster states using qubits located in the $4m-3 (m = 1, 2, \cdot\cdot, \lfloor \frac{N+3}{4} \rfloor)$

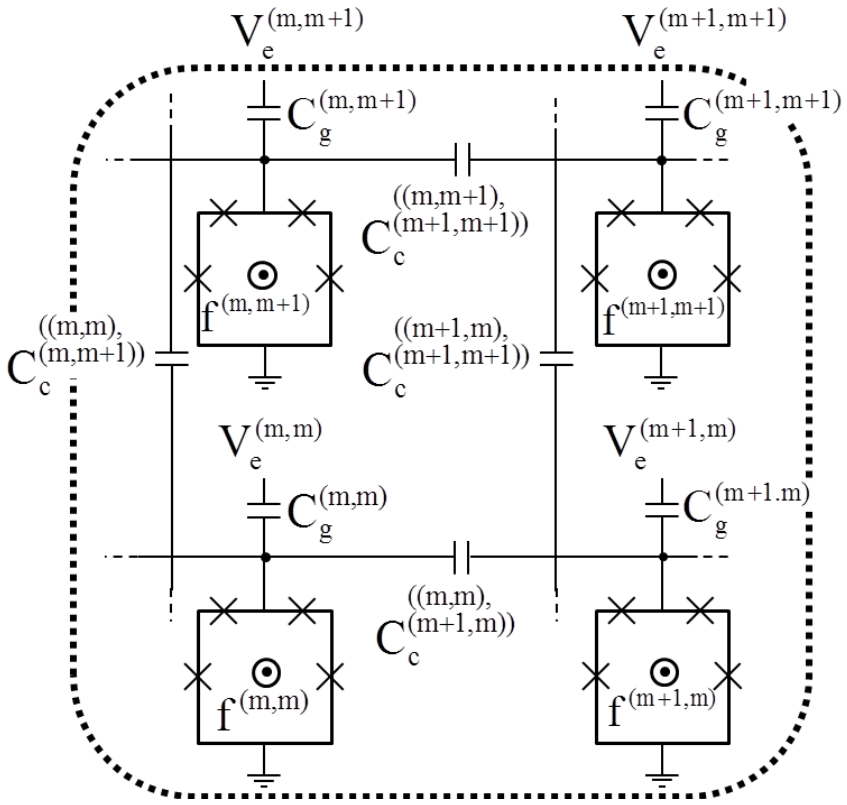

Figure 4.17: Physical circuit for generating a two dimensional cluster state. These four qubits correspond to the qubits surrounded by dot line in Fig. 4.18. Two Josephson junctions directly connected to a node (the superconducting islands) have the Josephson energies and capacitances that are α times larger than the other two Josephson junctions. Every flux qubit at site (j,k) couples with the four nearest neighbor qubits via capacitance $Cc^{((j,k)(j\pm1,k\pm1))}$.

row in the same way as shown in Fig. 4.15. Then the spatially-correlated error of each qubit in the $4m-3$ row is smaller than $\frac{1}{10000}$. We show the outline of these steps in Fig. 4.18(a).

Step 4-6 We perform $(N-1)\lfloor\frac{N-2}{4}\rfloor$ controlled-phase gate to generate $\lfloor\frac{N-2}{4}\rfloor$ one dimensional cluster states using qubits located in the $4p-1(p=1,2,\cdot\cdot,\lfloor\frac{N+1}{4}\rfloor)$ row in the same way as above. We show the outline of these steps in Fig. 4.18(b).

Step 7-9 We perform $(N-1)\lfloor\frac{N}{4}\rfloor$ controlled-phase gate to generate a two dimensional graph state as shown in Fig. 4.18(c) using qubits located in the

$4m-3$ column across $\lfloor \frac{N}{2} \rfloor$ one dimensional cluster states. We show the outline of these steps in Fig. 4.18(c).

Step 10-12 We perform $(N-1)\lfloor \frac{N-2}{4} \rfloor$ controlled-phase gate to generate a two dimensional cluster states using qubits located in the $4p-1$ column. We show the outline of these steps in Fig. 4.18(d).

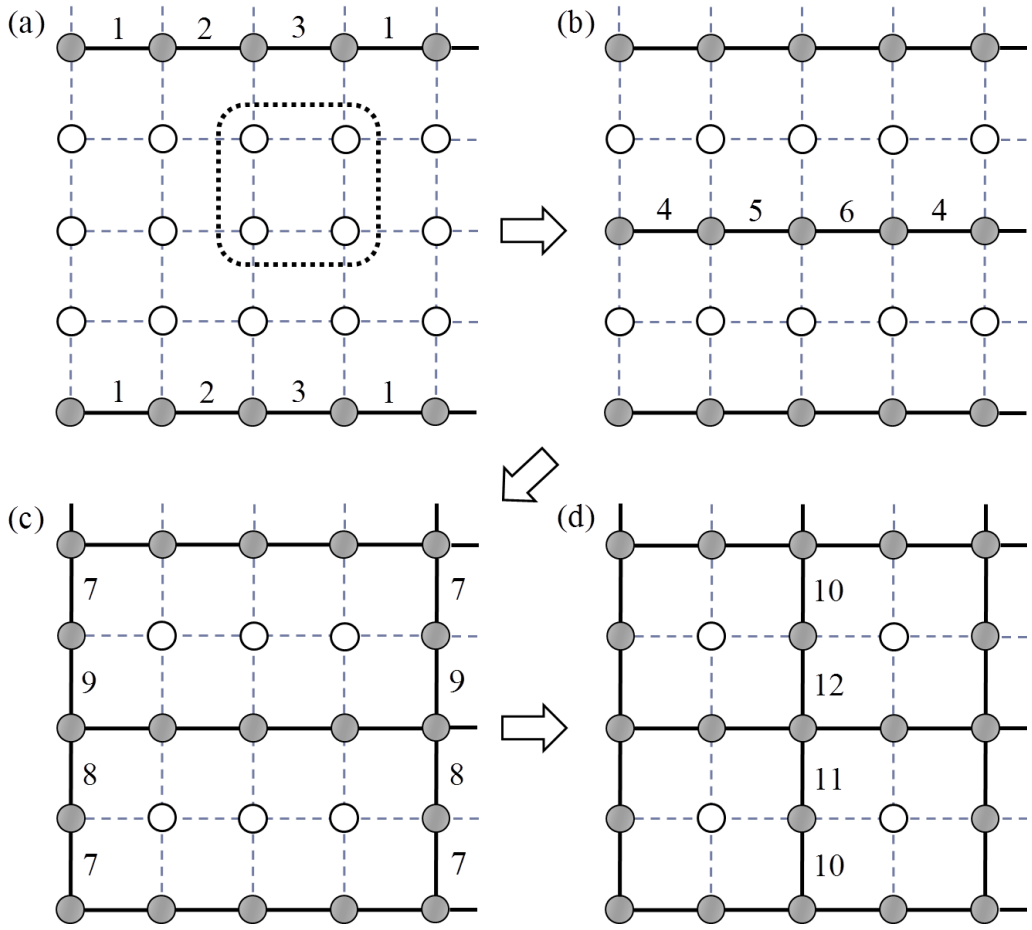

Figure 4.18: Schematic of our procedure for generating a two dimensional cluster state by graph state representation. Circles correspond to qubits, dashed lines correspond to electrically connection via a capacitance, solid-lines correspond to entanglement between qubits, and numbers show the order in which controlld-phase gates are performed by our procedure. White circles denote separable qubit, and gray circles denote qubits constituent of cluster state(s).

We show the details of each step of above procedure for generating a two

dimensional cluster state in Fig. 4.19. During each step, a part of the non-local

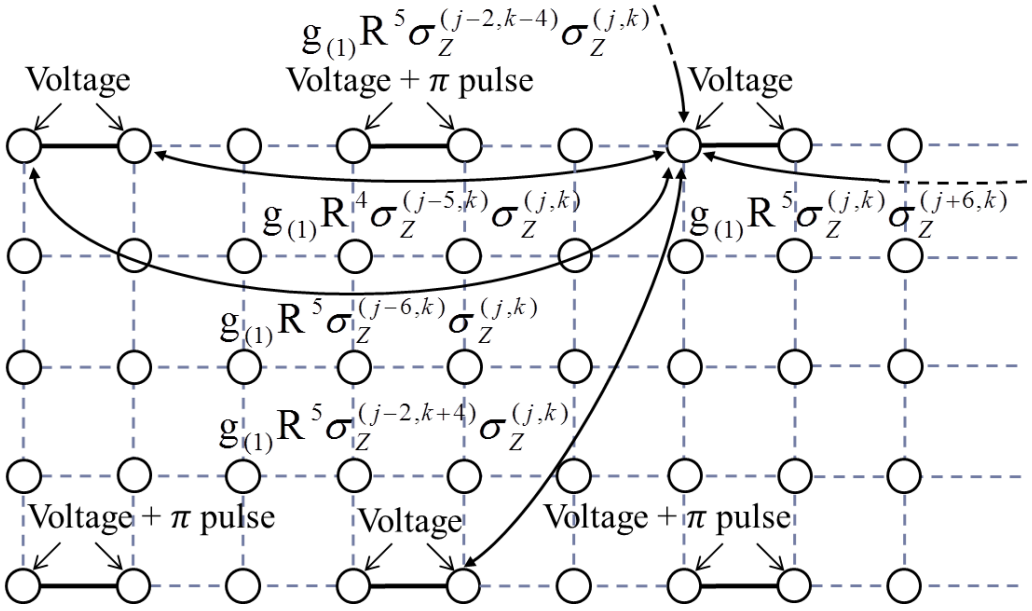

Figure 4.19: Operations and the influence of non-local interactions in generating a two dimensional cluster state. In this step, we apply voltage to qubit at site $(3n-2, 4m-3)$ and $(3n-1, 4m-3)$. Let the state evolve for a time $t_{cp}/2$, perform π pulses to qubit at site $(6n'-5, 8m'-7)$, $(6n'-4, 8m'-7)$, $(6n'-2, 8m'-3)$, and $(6n'-1, 8m'-3)$, and let the state evolve for a time $t_{cp}/2$. So that controlled-phase gates can be implemented between the pair of qubits at site $(3n-2, 4m-3)$ and $(3n-1, 4m-3)$. Here, $m = 1, 2, \cdot\cdot, \lfloor \frac{N+3}{4} \rfloor$, $m' = 1, 2, \cdot\cdot, \lfloor \frac{N+3}{8} \rfloor$, $n = 1, 2, \cdot\cdot, \lfloor \frac{N+1}{3} \rfloor$, and $n' = 1, 2, \cdot\cdot, \lfloor \frac{N+1}{6} \rfloor$. Each target qubit is affected by non-local interactions from qubits on the same row and other rows. We show mainly five non-local interactions with the qubit at site (j,k). These interactions are not cancelled out by π pulse.

interactions are not cancelled out by π pulses. When all coupling capacitance are $Cc \leq 0.077$ fF, the spatially-correlated error on each qubits become as follows:

$$\epsilon_{non}^{(j,k)} = \sum_{n=5}^{N/2} \frac{\pi}{4} R^{(n-1)} m_{(n)} \simeq \frac{\pi}{4}(R^4 + 4R^5) \leq \frac{1}{10000}. \tag{4.106}$$

The qubit at site (j, k) is affected by mainly five non-local interactions as shown in Fig. 4.19. The strength of the largest interaction is $g_{(1)}R^4$, and the strength of the other four interactions are $g_{(1)}R^5$. The remaining non-local interactions are negligibly small.

4.6 Discussion

In this chapter, we did not describe the details of the physical flux qubit system, in particular measurement system and electrical wiring. In general experimental system, flux qubits are few square micrometers and set on a substrate which is about 3.5 mm by 3.5 mm. This system has several terminals of electrical wiring. That is not enough to satisfy our requirements, several dozens and more. Current non-destructive measurement system as the Josephson bifurcation amplifier is also larger than flux qubits. There are several problems to solve for demonstration of above schemes. Even though it might be difficult to put into practice immediately, we propose our scheme as one of the possibility to acquire the scalability for quantum computation.

4.7 Conclusion

In conclusion, we suggest a new way to generate Ising interaction between capacitively-coupled superconducting flux qubits by using an applied voltage, and we also show an architecture about how to make a two-dimensional cluster state in this coupling scheme. Unlike the standard schemes, our scheme does not require to change the applied magnetic field on the flux qubit for the control of the interaction. Since applying local voltages is typically much easier than applying local magnetic flux, the scheme described in this chapter may have advantage to suppress a cross talk between the flux qubits. Our result paves the way for scalable quantum computation with superconducting flux qubits.

Chapter 5

Conclusion

In this dissertation, we have investigated obstacles for achieving the individual control of several controlled-phase gates using superconducting flux qubit system, and proposed two new approaches for scalable quantum information processing with flux qubits.

Firstly, we proposed the interaction control scheme for inductively coupled flux qubits where we utilize projective measurement and quantum feedforward. In this scheme, we assume that the always-on Ising type interactions between nearest neighbor flux qubits. Unitary operations such as applying magnetic field have been used to control the interaction in most of previous work. On the other hand, we use the non-unitary operation such as projective measurements. We showed the way to effectively turn on/off the interactions via measurement and quantum feedforward on the ancillary qubits which are inserted between the qubits for quantum computation. One advantage of our scheme is that the turning on/off of applied magnetic field is not required unlike previos schemes. This feature is important in order to suppress the cross-talk. Hence, it is expected to improve the individual addressability for parallel operations of controlled-phase gate. Furthermore, we proposed the constant step-size procedure for generating a large two or three-dimensional cluster state, which is useful for fault tolerant quantum computation.

Secondly, we proposed the tunable coupling method for four-junction flux qubits via a capacitance. We can control the Ising type interaction by bias

voltage to each qubit. It is typically known that the applying local voltage is much easier than applying local magnetic field. Therefore, we expect that our scheme has an advantage over the previous inductive coupling scheme in terms of cross-talk suppressing. To evaluate the performance of our scheme, we estimated a qubit-parameter range where one can perform fault-tolerant quantum computation with realistic noises. Moreover, we showed the constant step-size procedure for generating a one or two dimensional cluster states on the many qubit system. We expect that these results would be also a crucial step for the realization of flux-qubit based quantum computation.

In the short term, these suggestions show possible experiments as following. By using the first resluts, the interaction between three inductively coupled flux qubits can be controlled via quantum feedforward, which would be suitable for a proof of principle experiments. By using the second resluts, if we can fabricate a flux qubit having four Josephson junctions with apporopriate parameters, the tunnel energy of a flux qubit can be controlled by applied voltage, which no one has ever demonstrated. If two capacitively coupled flux qubits can be fabricated, we can demonstrate entanglement generation between them by controlling the applied voltage. These suggestions might be worth considering as a possibility to demonstrate in the near future.

In the long term, our results show that the flux-qubits system could be the key device for large-scale quantum computing. Furthermore, we show the concrete parameter sets which are requrired to implement fault-torelant quantum computation.

The ultimate aim of these proposal is to conduct the experiments. To realize our schemes, further research will be necessary in the future. We need to investigate the details of the physical setup including measurement device and pulse sequence to implement quantum feedforward and single gate operations. We also should consider the quantitative evaluation about further decoherence sources. Even though it is difficult to solve all those problems, we hope that these investigation based on the direction of this dissertation will improve the scalability of the flux qubit system.

References

[1] Daniel S. Abrams and Seth Lloyd. Simulation of many-body fermi systems on a universal quantum computer. *Phys. Rev. Lett.*, Vol. 79, pp. 2586–2589, Sep 1997.

[2] Dorit Aharonov, Alexei Kitaev, and John Preskill. Fault-tolerant quantum computation with long-range correlated noise. *Phys. Rev. Lett.*, Vol. 96, p. 050504, Feb 2006.

[3] A Albrecht, G Koplovitz, A Retzker, F Jelezko, S Yochelis, D Porath, Y Nevo, O Shoseyov, Y Paltiel, and M. B. Plenio. Self-assembling hybrid diamond-biological quantum devices. *New Journal of Physics*, Vol. 16, No. 9, p. 093002, 2014.

[4] Markus Ansmann, H Wang, Radoslaw C Bialczak, Max Hofheinz, Erik Lucero, M Neeley, AD O'Connell, D Sank, M Weides, J Wenner, et al. Violation of bell's inequality in josephson phase qubits. *Nature*, Vol. 461, No. 7263, pp. 504–506, 2009.

[5] Sahel Ashhab, AO Niskanen, Khalil Harrabi, Yasunobu Nakamura, Thomas Picot, PC De Groot, CJPM Harmans, JE Mooij, and Franco Nori. Interqubit coupling mediated by a high-excitation-energy quantum object. *Physical Review B*, Vol. 77, No. 1, p. 014510, 2008.

[6] R. Barends, J. Kelly, A. Megrant, D. Sank, E. Jeffrey, Y. Chen, Y. Yin, B. Chiaro, J. Mutus, C. Neill, P. O'Malley, P. Roushan, J. Wenner, T. C. White, A. N. Cleland, and John M. Martinis. Coherent josephson qubit

suitable for scalable quantum integrated circuits. *Phys. Rev. Lett.*, Vol. 111, p. 080502, Aug 2013.

[7] R. Barends, J. Kelly, A. Megrant, A. Veitia, D. Sank, E. Jeffrey, T. C. White, J. Mutus, A. G. Fowler, B. Campbell, Y. Chen, Z. Chen, B. Chiaro, A. Dunsworth, C. Neill, P. O'Malley, P. Roushan, A. Vainsencher, J. Wenner, A. N. Korotkov, A. N. Cleland, and John M. Martinis. Superconducting quantum circuits at the surface code threshold for fault tolerance. *Nature*, Vol. 508, , April 2014.

[8] R Barends, J Kelly, A Megrant, A Veitia, D Sank, E Jeffrey, TC White, J Mutus, AG Fowler, B Campbell, et al. Superconducting quantum circuits at the surface code threshold for fault tolerance. *Nature*, Vol. 508, No. 7497, pp. 500–503, 2014.

[9] Sean D. Barrett and Thomas M. Stace. Fault tolerant quantum computation with very high threshold for loss errors. *Phys. Rev. Lett.*, Vol. 105, p. 200502, Nov 2010.

[10] Jan Benhelm, Gerhard Kirchmair, Christian F. Roos, and Rainer Blatt. Towards fault-tolerant quantum computing with trapped ions. *Nature Physics*, Vol. 4, pp. 463–466, June 2008.

[11] S. C. Benjamin and S. Bose. Quantum computing in arrays coupled by "always-on" interactions. *Phys. Rev. A*, Vol. 70, p. 032314, Sep 2004.

[12] Simon C. Benjamin and Sougato Bose. Quantum computing with an always-on heisenberg interaction. *Phys. Rev. Lett.*, Vol. 90, p. 247901, Jun 2003.

[13] Charles H Bennett, Ethan Bernstein, Gilles Brassard, and Umesh Vazirani. Strengths and weaknesses of quantum computing. *SIAM journal on Computing*, Vol. 26, No. 5, pp. 1510–1523, 1997.

[14] A Bermudez, F Jelezko, M. B. Plenio, and A Retzker. Electron-mediated nuclear-spin interactions between distant nitrogen-vacancy centers. *Physical review letters*, Vol. 107, No. 15, p. 150503, 2011.

[15] Pierre-Marie Billangeon, et al. private communication.

[16] P. Oscar Boykin, Tal Mor, Matthew Pulver, Vwani Roychowdhury, and Farrokh Vatan. On universal and fault-tolerant quantum computing. In *Proceedings of 40th FOCS*, pp. 486–494. Society Press, 1999.

[17] Jonas Bylander, Simon Gustavsson, Fei Yan, Fumiki Yoshihara, Khalil Harrabi, George Fitch, David G Cory, Yasunobu Nakamura, Jaw-Shen Tsai, and William D Oliver. Noise spectroscopy through dynamical decoupling with a superconducting flux qubit. *Nature Physics*, Vol. 7, No. 7, pp. 565–570, 2011.

[18] Jonas Bylander, Simon Gustavsson, Fei Yan, Fumiki Yoshihara, Khalil Harrabi, George Fitch, David G Cory, Yasunobu Nakamura, Jaw-Shen Tsai, and William D Oliver. Noise spectroscopy through dynamical decoupling with a superconducting flux qubit. *Nature Physics*, Vol. 7, No. 7, pp. 565–570, 2011.

[19] Gang Chen, Zidong Chen, Lixian Yu, and Jiuqing Liang. One-step generation of cluster states in superconducting charge qubits coupled with a nanomechanical resonator. *Phys. Rev. A*, Vol. 76, p. 024301, Aug 2007.

[20] Yu-Ao Chen, Sylvain Nascimbène, Monika Aidelsburger, Marcos Atala, Stefan Trotzky, and Immanuel Bloch. Controlling correlated tunneling and superexchange interactions with ac-driven optical lattices. *Physical review letters*, Vol. 107, No. 21, p. 210405, 2011.

[21] Yu Chen, C Neill, P Roushan, N Leung, M Fang, R Barends, J Kelly, B Campbell, Z Chen, B Chiaro, et al. Qubit architecture with high coherence and fast tunable coupling. *arXiv preprint arXiv:1402.7367*, 2014.

[22] Kevin K. H. Cheung and Michele Mosca. Decomposing finite abelian groups. *Quantum Info. Comput.*, Vol. 1, No. 3, pp. 26–32, October 2001.

[23] J. Chiaverini and W. E. Lybarger. Laserless trapped-ion quantum simulations without spontaneous scattering using microtrap arrays. *Phys. Rev. A*, Vol. 77, p. 022324, Feb 2008.

[24] Andrew M Childs, Richard Cleve, Enrico Deotto, Edward Farhi, Sam Gutmann, and Daniel A Spielman. Exponential algorithmic speedup by a quantum walk. In *Proceedings of the thirty-fifth annual ACM symposium on Theory of computing*, pp. 59–68. ACM, 2003.

[25] I Chiorescu, Y Nakamura, CJP Ma Harmans, and JE Mooij. Coherent quantum dynamics of a superconducting flux qubit. *Science*, Vol. 299, No. 5614, pp. 1869–1871, 2003.

[26] C Counsell, M.H Levitt, and R.R Ernst. Analytical theory of composite pulses. *Journal of Magnetic Resonance (1969)*, Vol. 63, No. 1, pp. 133 – 141, 1985.

[27] Adriano Barenco David Deutsch and Artur Ekert. Universality in quantum computation. In *Proceedings of Mathematical and Physical Sciences*, Vol. 449, pp. 669–677, 1995.

[28] X-L Deng, D Porras, and J. I. Cirac. Effective spin quantum phases in systems of trapped ions. *Physical Review A*, Vol. 72, No. 6, p. 063407, 2005.

[29] David Deutsch and Richard Jozsa. Rapid solution of problems by quantum computation. *Proceedings of the Royal Society of London. Series A: Mathematical and Physical Sciences*, Vol. 439, No. 1907, pp. 553–558, 1992.

[30] Simon J Devitt, Ashley M Stephens, William J Munro, and Kae Nemoto. Requirements for fault-tolerant factoring on an atom-optics quantum computer. *Nature communications*, Vol. 4, , 2013.

[31] L DiCarlo, JM Chow, JM Gambetta, Lev S Bishop, BR Johnson, DI Schuster, J Majer, A Blais, L Frunzio, SM Girvin, et al. Demonstration of two-qubit algorithms with a superconducting quantum processor. *Nature*, Vol. 460, No. 7252, pp. 240–244, 2009.

[32] David P. DiVincenzo. Two-bit gates are universal for quantum computation. *Phys. Rev. A*, Vol. 51, pp. 1015–1022, Feb 1995.

[33] F Dolde, I Jakobi, B Naydenov, N Zhao, S Pezzagna, C Trautmann, J Meijer, P Neumann, F Jelezko, and J Wrachtrup. Room-temperature entanglement between single defect spins in diamond. *Nature Physics*, Vol. 9, No. 3, pp. 139–143, 2013.

[34] L-M Duan, E Demler, and M. D. Lukin. Controlling spin exchange interactions of ultracold atoms in optical lattices. *Physical review letters*, Vol. 91, No. 9, p. 090402, 2003.

[35] Matthew B. Elliott, Bryan Eastin, and Carlton M. Caves. Graphical description of the action of clifford operators on stabilizer states. *Phys. Rev. A*, Vol. 77, p. 042307, Apr 2008.

[36] Axel Friedenauer, Hector Schmitz, Jan Tibor Glueckert, Diego Porras, and Tobias Schätz. Simulating a quantum magnet with trapped ions. *Nature Physics*, Vol. 4, No. 10, pp. 757–761, 2008.

[37] Jonathan R Friedman, Vijay Patel, Wei Chen, SK Tolpygo, and James E Lukens. Quantum superposition of distinct macroscopic states. *nature*, Vol. 406, No. 6791, pp. 43–46, 2000.

[38] J. J. García-Ripoll, P. Zoller, and J. I. Cirac. Coherent control of trapped ions using off-resonant lasers. *Phys. Rev. A*, Vol. 71, p. 062309, Jun 2005.

[39] Michael R Geller, Emmanuel Donate, Yu Chen, Charles Neill, Pedram Roushan, and John M Martinis. Tunable coupler for superconducting xmon qubits: Perturbative nonlinear model. *arXiv preprint arXiv:1405.1915*, 2014.

[40] Joydip Ghosh, Andrei Galiautdinov, Zhongyuan Zhou, Alexander N. Korotkov, John M. Martinis, and Michael R. Geller. High-fidelity controlled-z gate for resonator-based superconducting quantum computers. *Phys. Rev. A*, Vol. 87, p. 022309, Feb 2013.

[41] M. Grajcar, Yu-xi Liu, Franco Nori, and A. M. Zagoskin. Switchable resonant coupling of flux qubits. *Phys. Rev. B*, Vol. 74, p. 172505, Nov 2006.

[42] Peter Groszkowski, Austin G. Fowler, Felix Motzoi, and Frank K. Wilhelm. Tunable coupling between three qubits as a building block for a superconducting quantum computer. *Phys. Rev. B*, Vol. 84, p. 144516, Oct 2011.

[43] Lov K. Grover. Quantum computers can search arbitrarily large databases by a single query. *Phys. Rev. Lett.*, Vol. 79, pp. 4709–4712, Dec 1997.

[44] Lov K. Grover. Rapid sampling though quantum computing. In *Proceedings of STOC'00*, pp. 618–626, 2000.

[45] Guo-Ping Guo, Hui Zhang, Tao Tu, and Guang-Can Guo. One-step preparation of cluster states in quantum-dot molecules. *Phys. Rev. A*, Vol. 75, p. 050301, May 2007.

[46] R Harris, AJ Berkley, MW Johnson, P Bunyk, S Govorkov, MC Thom, S Uchaikin, AB Wilson, J Chung, E Holtham, et al. Sign-and magnitude-tunable coupler for superconducting flux qubits. *Physical review letters*, Vol. 98, No. 17, p. 177001, 2007.

[47] Aram W Harrow, Avinatan Hassidim, and Seth Lloyd. Quantum algorithm for linear systems of equations. *Physical review letters*, Vol. 103, No. 15, p. 150502, 2009.

[48] M. Hein, W. Dür, J. Eisert, R. Raussendorf, M. Van den Nest, and H. J. Briegel. Entanglement in graph states and its applications. In *Proceedings of the International School of Physics "Enrico Fermi" on "Quantum Computers, Algorithms and Chaos"*, 2005.

[49] M. Hein, J. Eisert, and H. J. Briegel. Multiparty entanglement in graph states. *Phys. Rev. A*, Vol. 69, p. 062311, Jun 2004.

[50] Travis Hime, PA Reichardt, BLT Plourde, TL Robertson, C-E Wu, AV Ustinov, and John Clarke. Solid-state qubits with current-controlled coupling. *science*, Vol. 314, No. 5804, pp. 1427–1429, 2006.

[51] Max Hofheinz, H Wang, Markus Ansmann, Radoslaw C Bialczak, Erik Lucero, Matthew Neeley, AD O'Connell, Daniel Sank, J Wenner, John M Martinis, et al. Synthesizing arbitrary quantum states in a superconducting resonator. *Nature*, Vol. 459, No. 7246, pp. 546–549, 2009.

[52] D Hover, S Zhu, T Thorbeck, GJ Ribeill, D Sank, J Kelly, R Barends, John M Martinis, and R McDermott. High fidelity qubit readout with the superconducting low-inductance undulatory galvanometer microwave amplifier. *Applied Physics Letters*, Vol. 104, No. 15, p. 152601, 2014.

[53] Yong Hu, Zheng-Wei Zhou, and Guang-Can Guo. Always on non-nearest-neighbour coupling in scalable quantum computing. *New Journal of Physics*, Vol. 9, No. 2, p. 27, 2007.

[54] Kensuke Inaba, Yuuki Tokunaga, Kiyoshi Tamaki, Kazuhiro Igeta, and Makoto Yamashita. High-fidelity cluster state generation for ultracold atoms in an optical lattice. *Phys. Rev. Lett.*, Vol. 112, p. 110501, Mar 2014.

[55] Evan Jeffrey, Daniel Sank, J. Y. Mutus, T. C. White, J. Kelly, R. Barends, Y. Chen, Z. Chen, B. Chiaro, A. Dunsworth, A. Megrant, P. J. J. O'Malley, C. Neill, P. Roushan, A. Vainsencher, J. Wenner, A. N. Cleland, and John M. Martinis. Fast accurate state measurement with superconducting qubits. *Phys. Rev. Lett.*, Vol. 112, p. 190504, May 2014.

[56] Liang Jiang, Ana Maria Rey, Oriol Romero-Isart, J. J. García-Ripoll, Anna Sanpera, and Mikhail D Lukin. Preparation of decoherence-free cluster states with optical superlattices. *Physical Review A*, Vol. 79, No. 2, p. 022309, 2009.

[57] Dominic William Jordan and Peter Smith. *Nonlinear ordinary differential equations: an introduction for scientists and engineers*. New York, 2007.

[58] K Kakuyanagi, S Kagei, R Koibuchi, S Saito, A Lupaşcu, K Semba, and H Nakano. Experimental analysis of the measurement strength dependence of superconducting qubit readout using a josephson bifurcation readout method. *New Journal of Physics*, Vol. 15, No. 4, p. 043028, 2013.

[59] A Yu Kitaev. Fault-tolerant quantum computation by anyons. *Annals of Physics*, Vol. 303, No. 1, pp. 2–30, 2003.

[60] Jens Koch, Terri M. Yu, Jay Gambetta, A. A. Houck, D. I. Schuster, J. Majer, Alexandre Blais, M. H. Devoret, S. M. Girvin, and R. J. Schoelkopf. Charge-insensitive qubit design derived from the cooper pair box. *Phys. Rev. A*, Vol. 76, p. 042319, Oct 2007.

[61] Chiu Fan Lee and Neil F. Johnson. Efficient quantum computation within a disordered heisenberg spin chain. *Phys. Rev. A*, Vol. 70, p. 052322, Nov 2004.

[62] Malcolm H Levitt. Composite pulses. *Progress in Nuclear Magnetic Resonance Spectroscopy*, Vol. 18, No. 2, pp. 61–122, 1986.

[63] P. B. Li, Y. Gu, Q. H. Gong, and G. C. Guo. Generation of ising interaction and cluster states in a one-dimensional coupled resonator waveguide. *The European Physical Journal D*, Vol. 55, No. 1, pp. 205–209, 2009.

[64] Zhi-Rong Lin, Guo-Ping Guo, Tao Tu, Fei-Yun Zhu, and Guang-Can Guo. Generation of quantum-dot cluster states with a superconducting transmission line resonator. *Phys. Rev. Lett.*, Vol. 101, p. 230501, Dec 2008.

[65] Seth Lloyd. Almost any quantum logic gate is universal. *Phys. Rev. Lett.*, Vol. 75, pp. 346–349, Jul 1995.

[66] JB Majer, FG Paauw, ACJ Ter Haar, CJPM Harmans, and JE Mooij. Spectroscopy on two coupled superconducting flux qubits. *Physical review letters*, Vol. 94, No. 9, p. 090501, 2005.

[67] Olaf. Mandel, Markus. Greiner, Artur. Widera, Tim. Rom, Theodor W. Hansch, and Immanue Bloch. Controlled collisions for multi-particle entanglement of optically trapped atoms. *Nature*, Vol. 425, pp. 937–940, Oct 2003.

[68] Olaf Mandel, Markus Greiner, Artur Widera, Tim Rom, Theodor W. Hänsch, and Immanuel Bloch. Coherent transport of neutral atoms in spin-dependent optical lattice potentials. *Phys. Rev. Lett.*, Vol. 91, p. 010407, Jul 2003.

[69] Vladimir E Manucharyan, Jens Koch, Leonid I Glazman, and Michel H Devoret. Fluxonium: Single cooper-pair circuit free of charge offsets. *Science*, Vol. 326, No. 5949, pp. 113–116, 2009.

[70] Piero Martin, J Adamek, P Agostinetti, M Agostini, A Alfier, C Angioni, V Antoni, L Apolloni, F Auriemma, O Barana, et al. Overview of the rfx fusion science program. *Nuclear Fusion*, Vol. 51, No. 9, p. 094023, 2011.

[71] C. Monroe, R. Raussendorf, A. Ruthven, K. R. Brown, P. Maunz, L.-M. Duan, and J. Kim. Large-scale modular quantum-computer architecture with atomic memory and photonic interconnects. *Phys. Rev. A*, Vol. 89, p. 022317, Feb 2014.

[72] JE Mooij, TP Orlando, L Levitov, Lin Tian, Caspar H Van der Wal, and Seth Lloyd. Josephson persistent-current qubit. *Science*, Vol. 285, No. 5430, pp. 1036–1039, 1999.

[73] Kae Nemoto, Michael Trupke, Simon J. Devitt, Ashley M. Stephens, Burkhard Scharfenberger, Kathrin Buczak, Tobias Nöbauer, Mark S. Everitt, Jörg Schmiedmayer, and William J. Munro. Photonic architecture for scalable quantum information processing in diamond. *Phys. Rev. X*, Vol. 4, p. 031022, Aug 2014.

[74] P Neumann, R Kolesov, B Naydenov, J Beck, F Rempp, M Steiner, V Jacques, G Balasubramanian, ML Markham, DJ Twitchen, et al. Quan-

tum register based on coupled electron spins in a room-temperature solid. *Nature Physics*, Vol. 6, No. 4, pp. 249–253, 2010.

[75] Michael A Nielsen. Cluster-state quantum computation. *Reports on Mathematical Physics*, Vol. 57, No. 1, pp. 147–161, 2006.

[76] AO Niskanen, K Harrabi, F Yoshihara, Y Nakamura, S Lloyd, and JS Tsai. Quantum coherent tunable coupling of superconducting qubits. *Science*, Vol. 316, No. 5825, pp. 723–726, 2007.

[77] AO Niskanen, K Harrabi, F Yoshihara, Y Nakamura, and JS Tsai. Spectroscopy of three strongly coupled flux qubits. *Physical Review B*, Vol. 74, No. 22, p. 220503, 2006.

[78] TP Orlando, JE Mooij, Lin Tian, Caspar H van der Wal, LS Levitov, Seth Lloyd, and JJ Mazo. Superconducting persistent-current qubit. *Physical Review B*, Vol. 60, No. 22, p. 15398, 1999.

[79] C. Padurariu and Yu. V. Nazarov. Theoretical proposal for superconducting spin qubits. *Phys. Rev. B*, Vol. 81, p. 144519, Apr 2010.

[80] B. L. T. Plourde, J. Zhang, K. B. Whaley, F. K. Wilhelm, T. L. Robertson, T. Hime, S. Linzen, P. A. Reichardt, C.-E. Wu, and John Clarke. Entangling flux qubits with a bipolar dynamic inductance. *Phys. Rev. B*, Vol. 70, p. 140501, Oct 2004.

[81] D Porras and J. I. Cirac. Effective quantum spin systems with trapped ions. *Physical review letters*, Vol. 92, No. 20, p. 207901, 2004.

[82] P Rabl, SJ Kolkowitz, FHL Koppens, JGE Harris, P Zoller, and Mikhail D Lukin. A quantum spin transducer based on nanoelectromechanical resonator arrays. *Nature Physics*, Vol. 6, No. 8, pp. 602–608, 2010.

[83] R. Raussendorf, J. Harrington, and K. Goyal. A fault-tolerant one-way quantum computer. *Annals of Physics*, Vol. 321, No. 9, pp. 2242 – 2270, 2006.

[84] R Raussendorf, J Harrington, and K Goyal. Topological fault-tolerance in cluster state quantum computation. *New Journal of Physics*, Vol. 9, No. 6, p. 199, 2007.

[85] Robert Raussendorf and Hans J. Briegel. A one-way quantum computer. *Phys. Rev. Lett.*, Vol. 86, pp. 5188–5191, May 2001.

[86] Robert Raussendorf, Daniel E. Browne, and H. J. Briegel. Measurement-based quantum computation on cluster states. *Phys. Rev. A*, Vol. 68, p. 022312, Aug 2003.

[87] Robert Raussendorf and Jim Harrington. Fault-tolerant quantum computation with high threshold in two dimensions. *Phys. Rev. Lett.*, Vol. 98, p. 190504, May 2007.

[88] P. Ribenboim. *The New Book of Prime Number Records*. 3rd edition, 1995.

[89] D Ristè, M Dukalski, CA Watson, G de Lange, MJ Tiggelman, Ya M Blanter, KW Lehnert, RN Schouten, and L DiCarlo. Deterministic entanglement of superconducting qubits by parity measurement and feedback. *Nature*, Vol. 502, No. 7471, pp. 350–354, 2013.

[90] C A Ryan, M Laforest, and R Laflamme. Randomized benchmarking of single- and multi-qubit control in liquid-state nmr quantum information processing. *New Journal of Physics*, Vol. 11, No. 1, p. 013034, 2009.

[91] M Schaffry, S C Benjamin, and Y Matsuzaki. Quantum entanglement distribution using a magnetic field sensor. *New Journal of Physics*, Vol. 14, No. 2, p. 023046, 2012.

[92] Eyob Sete, Andrei Galiautdinov, Eric Mlinar, John Martinis, and Alexander Korotkov. Catch-disperse-release readout for superconducting qubits. *Phys. Rev. Lett.*, Vol. 110, p. 210501, May 2013.

[93] Peter W. Shor. Polynomial-time algorithms for prime factorization and discrete logarithms on a quantum computer. *SIAM J. on Computing*, pp. 1484–1509, 1997.

[94] I Siddiqi, R Vijay, M Metcalfe, E Boaknin, L Frunzio, RJ Schoelkopf, and MH Devoret. Dispersive measurements of superconducting qubit coherence with a fast latching readout. *Physical Review B*, Vol. 73, No. 5, p. 054510, 2006.

[95] I. Siddiqi, R. Vijay, F. Pierre, C. M. Wilson, M. Metcalfe, C. Rigetti, L. Frunzio, and M. H. Devoret. Rf-driven josephson bifurcation amplifier for quantum measurement. *Phys. Rev. Lett.*, Vol. 93, p. 207002, Nov 2004.

[96] Daniel R Simon. On the power of quantum computation. *SIAM Journal on Computing*, Vol. 26, No. 5, pp. 1474–1483, 1997.

[97] Jonathan Simon, Waseem S Bakr, Ruichao Ma, M Eric Tai, Philipp M Preiss, and Markus Greiner. Quantum simulation of antiferromagnetic spin chains in an optical lattice. *Nature*, Vol. 472, No. 7343, pp. 307–312, 2011.

[98] Thomas M. Stace, Sean D. Barrett, and Andrew C. Doherty. Thresholds for topological codes in the presence of loss. *Phys. Rev. Lett.*, Vol. 102, p. 200501, May 2009.

[99] Matthias Steffen, M Ansmann, Radoslaw C Bialczak, Nadav Katz, Erik Lucero, R McDermott, Matthew Neeley, Eva Maria Weig, Andrew N Cleland, and John M Martinis. Measurement of the entanglement of two superconducting qubits via state tomography. *Science*, Vol. 313, No. 5792, pp. 1423–1425, 2006.

[100] Matthias Steffen, Frederico Brito, David DiVincenzo, Matthew Farinelli, George Keefe, Mark Ketchen, Shwetank Kumar, Frank Milliken, Mary Beth Rothwell, Jim Rozen, et al. Quantum information storage using tunable flux qubits. *Journal of Physics: Condensed Matter*, Vol. 22, No. 5, p. 053201, 2010.

[101] M. Stern, G. Catelani, Y. Kubo, C. Grezes, A. Bienfait, D. Vion, D. Esteve, and P. Bertet. Flux qubits with long coherence times for hybrid quantum circuits. *Phys. Rev. Lett.*, Vol. 113, p. 123601, Sep 2014.

[102] A Marshall Stoneham, Anthony Henry Harker, and Gavin W Morley. Could one make a diamond-based quantum computer? *Journal of Physics: Condensed Matter*, Vol. 21, No. 36, p. 364222, 2009.

[103] Tetsufumi Tanamoto. One- and two-dimensional n-qubit systems in capacitively coupled quantum dots. *Phys. Rev. A*, Vol. 64, p. 062306, Nov 2001.

[104] Stefan Trotzky, Patrick Cheinet, Simon Fölling, M Feld, Ute Schnorrberger, Ana Maria Rey, Anatoli Polkovnikov, EA Demler, Mikhail D Lukin, and I Bloch. Time-resolved observation and control of superexchange interactions with ultracold atoms in optical lattices. *Science*, Vol. 319, No. 5861, pp. 295–299, 2008.

[105] R. Tycko, A. Pines, and J. Guckenheimer. Fixed-point theory of iterative excitation schemes in nmr. *Journal of Chemical Physics*, Vol. 83, pp. 2775–2802, 1985.

[106] M Van den Nest, W Dür, A Miyake, and HJ Briegel. Fundamentals of universality in one-way quantum computation. *New Journal of Physics*, Vol. 9, No. 6, p. 204, 2007.

[107] Maarten Van den Nest, Jeroen Dehaene, and Bart De Moor. Graphical description of the action of local clifford transformations on graph states. *Phys. Rev. A*, Vol. 69, p. 022316, Feb 2004.

[108] S. H. W. van der Ploeg, A. Izmalkov, Alec Maassen van den Brink, U. Hübner, M. Grajcar, E. Il'ichev, H.-G. Meyer, and A. M. Zagoskin. Controllable coupling of superconducting flux qubits. *Phys. Rev. Lett.*, Vol. 98, p. 057004, Feb 2007.

[109] Caspar H Van der Wal, ACJ Ter Haar, FK Wilhelm, RN Schouten, CJPM Harmans, TP Orlando, Seth Lloyd, and JE Mooij. Quantum superposition of macroscopic persistent-current states. *Science*, Vol. 290, No. 5492, pp. 773–777, 2000.

[110] R Vijay, Chris Macklin, DH Slichter, SJ Weber, KW Murch, R Naik, Alexander N Korotkov, and I Siddiqi. Stabilizing rabi oscillations in a superconducting qubit using quantum feedback. *Nature*, Vol. 490, No. 7418, pp. 77–80, 2012.

[111] Yaakov S. Weinstein, C. Stephen Hellberg, and Jeremy Levy. Quantum-dot cluster-state computing with encoded qubits. *Phys. Rev. A*, Vol. 72, p. 020304, Aug 2005.

[112] T Yamamoto, M Watanabe, JQ You, Yu A Pashkin, O Astafiev, Y Nakamura, F Nori, and JS Tsai. Spectroscopy of superconducting charge qubits coupled by a josephson inductance. *Physical Review B*, Vol. 77, No. 6, p. 064505, 2008.

[113] N. Y. Yao, L. Jiang, A. V. Gorshkov, P. C. Maurer, G. Giedke, J. I. Cirac, and M. D. Lukin. Scalable architecture for a room temperature solid-state quantum information processor. *Nature Communications*, Vol. 3, p. 800, 2012.

[114] Fumiki Yoshihara, Yasunobu Nakamura, Fei Yan, Simon Gustavsson, Jonas Bylander, William D. Oliver, and Jaw-Shen Tsai. Flux qubit noise spectroscopy using rabi oscillations under strong driving conditions. *Phys. Rev. B*, Vol. 89, p. 020503, Jan 2014.

[115] JQ You, Xuedong Hu, S Ashhab, and Franco Nori. Low-decoherence flux qubit. *Physical Review B*, Vol. 75, No. 14, p. 140515, 2007.

[116] Christof Zalka. Efficient simulation of quantum systems by quantum computers. *Fortschritte der Physik*, Vol. 46, No. 6-8, pp. 877–879, 1998.

[117] Shi-Biao Zheng. Generation of cluster states in ion-trap systems. *Phys. Rev. A*, Vol. 73, p. 065802, Jun 2006.

[118] Xingxiang Zhou, Zheng-Wei Zhou, Guang-Can Guo, and Marc J. Feldman. Quantum computation with untunable couplings. *Phys. Rev. Lett.*, Vol. 89, p. 197903, Oct 2002.

[119] Zhongyuan Zhou, Shih-I Chu, and Siyuan Han. Unified approach for universal quantum gates in a coupled superconducting two-qubit system with fixed always-on coupling. *Phys. Rev. B*, Vol. 73, p. 104521, Mar 2006.

[120] Guanyu Zhu, David G. Ferguson, Vladimir E. Manucharyan, and Jens Koch. Circuit qed with fluxonium qubits: Theory of the dispersive regime. *Phys. Rev. B*, Vol. 87, p. 024510, Jan 2013.